THE CRUSTAL STRUCTURE OF THE EASTERN MARMARA REGION USING RECEIVER FUNCTION ANALYSIS

by

Pınar Büyükakpınar

B.S, Geophysical Engineering, Süleyman Demirel University, 2009

M.S, Geophysics, Boğaziçi University, 2013

Submitted to the Kandilli Observatory and Earthquake
Research Institute in partial fulfillment of
the requirements for the degree of
Doctor of Philosophy

Graduate Program in Geophysics
Boğaziçi University
2019

This thesis is dedicated to
love of my life.

ACKNOWLEDGEMENTS

First of all, I would like to express my sincere appreciation and gratitude to my advisor, Prof. Dr. Mustafa AKTAR for his educational guidance and encouraging instruction in the improvement and completion of my study. The desire in our working times inspired me. It is obvious how much he likes this job from his eyes, and it affects me very much. He always gives me useful suggestions so that I could improve my research and writing skills in a broader context. I always remember his soft voice and our nice conversations.

I would like to thank Prof. Dr. Argun KOCAOĞLU and Assoc. Prof. Ali Özgün KONCA, for their guidance, and support throughout this research.

In addition, I would like to thank Assoc. Prof. Ekrem ZOR and Dr. Yaman ÖZAKIN for their insight, endeavor, and support for this research as well as providing me computer programs to enhance my study during the data processing stages.

I would also like to thank all of my friends and members of Kandilli Observatory and Earthquake Research Institute for encouraging me to continue on and finish up my thesis. I owe my profound gratitude and sincere thanks to my dear friend and colleague Fatih TURHAN for his endless support. My research would not have been possible without their help. In addition, I would like to thank Emre AÇIKGÖZ from TUBITAK for sharing the data set which is necessary for my study.

Finally, I would like to thank my wonderful family for their unconditional love and support. My mother and father deserve special recognition for being the best role models I could imagine. My brother has been my best friend all my life and I love him dearly and thank his for all his advice and support. I know I always have my family to count on when times are rough. I love them so much and, I undoubtedly could not have done this work without them.

ABSTRACT

THE CRUSTAL STRUCTURE OF THE EASTERN MARMARA REGION USING RECEIVER FUNCTION ANALYSIS

This study focuses on the crust of the Eastern Marmara in order to understand of how much the structure is influenced by the tectonic history and also by the activity of the NAF. Recent studies have claimed that the crustal thickness varies significantly on the north and south of the NAF, which is assumed to indicate the separation line between Eurasian and Anatolian Plates. The present study aims to reevaluate the claim above, using newly available data and recently developed tools. The methods used during the study are the receiver function analysis and surface wave analysis. The first one is more intensively applied, since the second one only serves to introduce stability constraint in the inversions. Data are obtained from the permanent network of KOERI and from PIRES arrays. The main result of the study indicates that the receiver functions for the stations close to the fault zone are essentially very different from the rest and should be treated separately. They show signs of complex 3D structures of which two were successfully analyzed by forward modeling (HRTX and ADVT). A dipping shallow layer is seen to satisfy the major part of the azimuthal variation at these two stations. For the stations off the fault on the other hand, the receiver functions show a more stable behavior and are analyzed successfully by classical methods. CCP stacking, H-k estimation, single and joint inversion with surface waves, are used for that purpose. The results obtained from these totally independent approaches are remarkably consistent with each other. It is observed that the crustal thickness does not vary significantly neither in the NS, nor in the SW direction. A deeper Moho can only be expected on two most NE stations where a gradual transition is more likely than a sharp boundary (SILT and KLYT). The structural trends, although not significant, are generally aligned in the EW direction. In particular, a slower lower crust is observed in the southern stations, which is possibly linked to the mantle upwelling and thermal transient of the Aegean extension. Otherwise neither the velocity, nor the thickness of the crust does not imply any significant variation across the fault zone, as was previously claimed.

ÖZET

ALICI FONKSİYONLARINI KULLANARAK DOĞU MARMARA BÖLGESİ'NİN KABUK YAPISININ BELİRLENMESİ

Bu çalışma, Doğu Marmara'nın kabuk yapısının tektonik olarak ne kadar KAF'ın hareketinden etkilendiğini anlamak üzerine odaklanmıştır. Son zamanlarda yapılan çalışmalar, kabuk kalınlığının Avrasya ve Anadolu Plakaları arasındaki ayrım çizgisini gösterdiği varsayılan KAF'ın kuzeyi ve güneyinde önemli ölçüde değiştiğini iddia etmiştir. Bu çalışma, yeni elde edilen verileri ve yeni geliştirilen araçları kullanarak yukarıdaki iddiayı yeniden değerlendirmeyi amaçlamaktadır. Çalışma sırasında kullanılan yöntemler, alıcı fonksiyon analizi ve yüzey dalgası analizidir. Birincisi daha yoğun bir şekilde uygulanmaktadır, çünkü ikincisi sadece ters çözümlerde denge kısıtlaması getirmeye yardımcı olmaktadır. Veriler, KOERI ve PIRES yerel diziliminden oluşan kalıcı ağlardan elde edilmiştir. Çalışmanın ana sonucu, fay bölgesine yakın olan istasyonlar için alıcı fonksiyonlarının diğerlerinden çok farklı olduğunu ve ayrı olarak ele alınması gerektiğini göstermektedir. İki tane ileri modelleme (HRTX ve ADVT) ile başarılı bir şekilde analiz edilen karmaşık 3D yapıların işaretlerini gösterirler. Bu iki istasyondaki başlıca azimut değişiminin büyük bölümünü dalan bir sığ katmanın sağladığı görülmektedir. Diğer taraftan, faydan uzak olan istasyonlar için alıcı fonksiyonları daha kararlı bir davranış sergiler ve klasik yöntemlerle başarılı bir şekilde analiz edilirler. Ortak dönüşüm noktaları yığması (CCP), kalınlık hız oranı tahmini (H-k), yüzey dalgaları ile tek ve ortak ters çözümler, bu amaç için kullanılır. Bu tamamen bağımsız yaklaşımlardan elde edilen sonuçlar, birbirleriyle oldukça tutarlıdır. Kabuk kalınlığının ne kuzey-güney ne de güneybatı yönünde önemli ölçüde değişmediği görülmektedir. Daha derin bir Moho süreksizliği ancak keskin bir kabuk sınırından ziyade kademeli bir kabuk geçişin (SILT ve KLYT) olduğu kuzey-güney istasyonlarının çoğunda beklenebilir. Yapısal eğilimler, önemli olmamakla birlikte, genellikle doğu-batı yönünde hizalanır. Özellikle, güneydeki istasyonlarda, muhtemelen Ege uzantısının manto yükselmesi ve termal geçişi durumuyla bağlantılı olan daha yavaş bir kabuk görülmektedir. Aksi takdirde, ne hız, ne de kabuk kalınlığı, daha önce iddia edildiği gibi, fay bölgesi boyunca önemli bir değişiklik göstermemektedir.

TABLE OF CONTENTS

ACKNOWLEDGEMENTS iv
ABSTRACT v
ÖZET vi
TABLE OF CONTENTS vii
LIST OF FIGURES ix
LIST OF TABLES xix
LIST OF SYMBOLS xx
LIST OF ACRONYMS/ABBREVIATIONS xxi
1. INTRODUCTION 1
2. TECTONICS OF EASTERN MARMARA REGION 7
3. METHODOLOGIES 14
   3.1. Receiver Function 14
      3.1.1. Receiver Function Analysis 16
   3.2. H-κ Stacking Technique 19
   3.3. Surface Wave Analysis 22
      3.3.1. Rayleigh Wave and Love Wave 22
      3.3.2. The Dispersion of Surface Waves 23
      3.3.3. Rayleigh Wave Dispersion 25
         3.3.3.1. Two-Station Method 26
   3.4. Joint Inversion Technique 26
   3.5. CCP Stacking 28
4. DATA ANALYSIS AND RESULTS 29

4.1. Data and Seismic Stations 29

4.2. The Data Quality Assessment 40

4.3. CCP Stacking Results of All Stations 58

4.4. H-κ Stacking Results 67

4.5. 1D RF Inversion Results 74

4.5.1. 1D RF Inversion Results of Northern Stations 89

4.5.2. 1D RF Inversion Results of Southern Stations 90

4.6. Joint Inversion Results 92

4.6.1. Results of Surface Wave Analysis 92

4.6.2. Joint Inversion Results of Northern Stations 96

4.6.3. Joint Inversion Results of Southern Stations 97

5. THREE DIMENSIONAL MODELLING OF RECEIVER FUNCTIONS 100

6. CONCLUSIONS AND DISCUSSIONS 106

REFERENCES 111

APPENDIX A1: RECEIVER FUNCTIONS FOR KOERI NETWORK 122

APPENDIX A2: RECEIVER FUNCTIONS FOR PIRES NETWORK 130

LIST OF FIGURES

Figure 2.1. The digital elevation map of Turkey and surroundings. Black lines are the main active faults. White arrows show the movement of the tectonic plates. Yellow circles are location of the earthquakes M>5.0 since 1950 (Çemen and Yılmaz, 2017). …………………………………………………………………………......8

Figure 2.2. GPS velocity vectors with respect to Eurasia. (Reilinger et al., 2006). 9

Figure 2.3. The seismicity map of the study region during 1900-Present (KOERI catalog). Fault lines are taken from MTA. 10

Figure 2.4. Focal Mechanism of 15 events (Mw≥4.8) in the Marmara Region since 1983. (Global CMT catalog). Fault lines are taken from MTA. 11

Figure 2.5. Morphotectonic components of the Marmara region (Yılmaz, 2017).................... 11

Figure 2.6. General geological structure of the Marmara region and its surrounding areas (Okay, 2008).. 13

Figure 3.1. Phase arrivals of teleseismic incident P wave for a layer over a half space model (left). Receiver function traces that show direct P, Ps conversions and its multiples, respectively (right). 15

Figure 3.2. NS, EW, radial (R), transverse (T) components and back-azimuth (BAZ) 17

Figure 3.3. 2011-05-14T21:07:20 Afghanistan Earthquake 3 components waveform (upper) and rotated components (below).. 18

Figure 3.4. Curves demonstrating the contributions of Ps and its multiples PpPs and PpSs+PsPs to the stacked amplitude as a function of crustal thickness and Vp/Vs ratio. 21

Figure 3.5. Displacements caused by horizontally propagating fundamental Love (left) and Rayleigh waves (right). In both cases the wave amplitudes decay strongly with depth (Shearer, Introduction to Seismology, 1999). 23

Figure 3.6. The comparison of the group velocity (U) and the phase velocity(c). The envelope of the wave packet propagates with the group velocity, and the phase of any component of the wave propagates with the phase velocity. (b) The arrivals of a dispersive wave at different receivers (Lowrie, 2007). 25

Figure 4.1. PIRES Network and Seismic Stations used in the study area. 30

Figure 4.2. Teleseismic earthquakes used in the study. 30

Figure 4.3. Basic steps in data analysis. 32

Figure 4.4. The azimuthal distribution of events used in the study. 33

Figure 4.5. The number of RFs for each station used in the study. 34

Figure 4.6. Magnitude versus fit value of radial RF’s in ADVT station. 34

Figure 4.7. Radial receiver functions with respect to the ray parameter in CTYL station. The number on the right of each trace demonstrates how many particular receiver functions contributed to the trace in the ray parameter of 0.04 s/km bins. 35

Figure 4.8. Radial RFs in (left), and tangential RFs (right) in CAVI station which is illustrated as the “stable station” in the study region due to the small variation of arrival times on the radial component and low energy on the tangential component. The number on the right of each trace demonstrates how many particular receiver functions contributed to the trace in the azimuth of 10° bins.. 37

Figure 4.9. Radial RFs in (left), and tangential RFs (right) in HRTX station which is illustrated as the “unstable station” in the study region due to the large variation of arrival times on the radial component and high energy on the tangential component. The number on the right of each trace demonstrates how many particular receiver functions contributed to the trace in the azimuth of 10° bins............................... 38

Figure 4.10. Stable, Quasi-stable and Unstable stations in the study area. Fault lines are taken from MTA. 40

Figure 4.11. The number of selected events with high S/N ratio for P-waves principal component analysis for each station.. 43

Figure 4.12. The field trip to the CTKS station located in Çatalca (left) and the correction of misoriented seismometer to the true north direction (right)................................. 44

Figure 4.13. The results of particle motion of the ADVT station for 38 earthquakes having BAZ 45-50 called Group 1 (left) and 51 earthquakes having BAZ 101-106 called Group 2 (right)... 47

Figure 4.14. The results of particle motion of the ARMT station for BAZ 45-50 called Group 1 (left), BAZ 101-106 called Group 2 (middle), and 2011-03-11 Mw=8.9 Tohoku Earthquake (right). 47

Figure 4.15. The results of particle motion of the BGKT station for BAZ 45-50 called Group 1 (left), BAZ 101-106 called Group 2 (middle), and 2011-03-11 Mw=8.9 Tohoku Earthquake (right) before 30.11.2016. 48

Figure 4.16. The results of particle motion of the BGKT station for BAZ 101-103 called Group 2 after 30.11.2016. 48

Figure 4.17. The results of particle motion of the CAVI station for BAZ 45-50 called Group 1 (left), BAZ 101-106 called Group 2 (middle), and 2011-03-11 Mw=8.9 Tohoku Earthquake (right). 49

Figure 4.18. The results of particle motion of the CTKS station for BAZ 45-50 called Group 1 (left), BAZ 101-106 called Group 2 (middle), and 2011-03-11 Mw=8.9 Tohoku Earthquake (right). 49

Figure 4.19. The results of particle motion of the CTYL station for BAZ 45-50 called Group 1 (left), BAZ 102-105 called Group 2 (middle), and 2011-03-11 Mw=8.9 Tohoku Earthquake (right) before 2011.06.22. 50

Figure 4.20. The results of particle motion of the CTYL station for BAZ 45-49 called Group 1 (left), BAZ 103-105 called Group 2 (right), after 2011.07.23. 50

Figure 4.21. The results of particle motion of the EDC station for BAZ 45-50 called Group 1 (left), BAZ 100-105 called Group 2 (middle), and 2011-03-11 Mw=8.9 Tohoku Earthquake (right).. 51

Figure 4.22. The results of particle motion of the GEMT station for BAZ 45-50 called Group 1 (left), BAZ 101-106 called Group 2 (middle), and 2011-03-11 Mw=8.9 Tohoku Earthquake (right).. 51

Figure 4.23. The results of particle motion of the HRTX station for BAZ 45-50 called Group 1 (left), BAZ 101-105 called Group 2 (middle), and 2011-03-11 Mw=8.9 Tohoku Earthquake (right).. 52

Figure 4.24. The results of particle motion of the ISK station for BAZ 45-50 called Group 1 (left), BAZ 101-106 called Group 2 (middle), and 2011-03-11 Mw=8.9 Tohoku Earthquake (right).. 52

Figure 4.25. The results of particle motion of the KCTX station for BAZ 45-50 called Group 1 (left), BAZ 101-106 called Group 2 (middle), and 2011-03-11 Mw=8.9 Tohoku Earthquake (right).. 53

Figure 4.26. The results of particle motion of the KLYT station for BAZ 46-50 called Group 1 (left), BAZ 101-104 called Group 2 (right), and before 2009.02.14.................... 53

Figure 4.27. The results of particle motion of the KLYT station for BAZ 45-50 called Group 1 (left), BAZ 101-106 called Group 2 (middle), and 2011-03-11 Mw=8.9 Tohoku Earthquake (right) after 2009.02.14. 54

Figure 4.28. The results of particle motion of the MDNY station for BAZ 45-50 called Group 1 (left), BAZ 101-106 called Group 2 (middle), and 2011-03-11 Mw=8.9 Tohoku Earthquake (right).. 54

Figure 4.29. The results of particle motion of the SILT station for BAZ 45-50 called Group 1 (left), BAZ 102-107 called Group 2 (middle), and 2011-03-11 Mw=8.9 Tohoku Earthquake (right).. 55

Figure 4.30. The results of particle motion of the YLV station for BAZ 45-49 called Group 1 (left), BAZ 101-106 called Group 2 (right)... 55

Figure 4.31. Angle of deviation for stations of KOERI Network between 01.01.2012-30.11.2016. 57

Figure 4.32. The location of Profile A (up) and CCP stacking result of Profile A (down). 59

Figure 4.33. The location of Profile B (up) and CCP stacking result of Profile B (down). 61

Figure 4.34. The location of Profile C (up) and CCP stacking result of Profile C (down). 63

Figure 4.35. The location of Profile D (up) and CCP stacking result of Profile D (down). 64

Figure 4.36. The location of Profile E (up) and CCP stacking result of Profile E (down)....... 66

Figure 4.37. H-κ stacking results for northern stations BGKT, CTKS, CTYL, ISK, KLYT, and SILT.. 70

Figure 4.38. H-κ stacking results for southern stations ARMT, CAVI, EDC, GEMT, KCTX, and MDNY. 71

Figure 4.39. The final Moho depth map Stable and Quasi-stable stations used in the study. .. 72

Figure 4.40. The final Vp/Vs ratio map for Stable and Quasi-stable stations used in the study. 73

Figure 4.41. ARMT station radial RFs for BAZ 12º - 116º (down-left) and stacked waveform for 268 events (top-left), H-K result (up-right). Blue signal is observed stacked waveform and red signal is predicted waveform for 1D inversion for the initial model (mid-right). 1D inversion result (down-right). 77

Figure 4.42. BGKT station radial RFs for BAZ 0º - 40º (down-left) and stacked waveform for 57 events (top-left), H-K result (up-right). Blue signal is observed stacked waveform and red signal is predicted waveform for 1D inversion for the initial model (mid-right). 1D inversion result (down-right). 78

Figure 4.43. CAVI station radial RFs for BAZ 1º - 108º (down-left) and stacked waveform for 312 events (top-left), H-K result (up-right). Blue signal is observed stacked waveform and red signal is predicted waveform for 1D inversion for the initial model (mid-right). 1D inversion result (down-right). 79

Figure 4.44. CTKS station radial RFs for BAZ 0º - 116º (down-left) and stacked waveform for 487 events (top-left), H-K result (up-right). Blue signal is observed stacked waveform and red signal is predicted waveform for 1D inversion for the initial model (mid-right). 1D inversion result (down-right). 80

Figure 4.45. CTYL station radial RFs for BAZ 0º - 117º (down-left) and stacked waveform for 400 events (top-left), H-K result (up-right). Blue signal is observed stacked waveform and red signal is predicted waveform for 1D inversion for the initial model (mid-right). 1D inversion result (down-right). 81

Figure 4.46. EDC station radial RFs for BAZ 0º - 110º (down-left) and stacked waveform for 333 events (top-left), H-K result (up-right). Blue signal is observed stacked waveform and red signal is predicted waveform for 1D inversion for the initial model (mid-right). 1D inversion result (down-right). 82

Figure 4.47. GEMT station radial RFs for BAZ 0º - 116º (down-left) and stacked waveform for 552 events (top-left), H-K result (up-right). Blue signal is observed stacked waveform and red signal is predicted waveform for 1D inversion for the initial model (mid-right). 1D inversion result (down-right). 83

Figure 4.48. ISK station radial RFs for BAZ 20º - 117º (down-left) and stacked waveform for 441 events (top-left), H-K result (up-right). Blue signal is observed stacked waveform and red signal is predicted waveform for 1D inversion for the initial model (mid-right). 1D inversion result (down-right). 84

Figure 4.49. KCTX station radial RFs for BAZ 0º - 110º (down-left) and stacked waveform for 233 events (top-left), H-K result (up-right). Blue signal is observed stacked waveform and red signal is predicted waveform for 1D inversion for the initial model (mid-right). 1D inversion result (down-right). 85

Figure 4.50. KLYT station radial RFs for BAZ 60º - 117º (down-left) and stacked waveform for 247 events (top-left), H-K result (up-right). Blue signal is observed stacked waveform and red signal is predicted waveform for 1D inversion for the initial model (mid-right). 1D inversion result (down-right). 86

Figure 4.51. MDNY station radial RFs for BAZ 1º - 58º (down-left) and stacked waveform for 249 events (top-left), H-K result (up-right).). Blue signal is observed stacked waveform and red signal is predicted waveform for 1D inversion for the initial model (mid-right). 1D inversion result (down-right).. 87

Figure 4.52. SILT station radial RFs for BAZ 60º - 117º (down-left) and stacked waveform for135 events (top-left), H-K result (up-right). Blue signal is observed stacked waveform and red signal is predicted waveform for 1D inversion for the initial model (mid-right). 1D inversion result (down-right).. 88

Figure 4.53. 1D inversion results for Northern Stations. Black dotted lines show the initial model (Karabulut et al., 2011). Red lines show the predicted final models....... 89

Figure 4.54. 1D inversion results for Southern Stations. Black dotted lines show the initial model (Karabulut et al., 2011). Red lines show the predicted final models....... 90

Figure 4.55. 1D inversion results for neighboring stations in northern part of the region (CTKS-BGKT-ISK) and in southern part (EDC-KCTX-ARMT-MDNY). 91

Figure 4.56. Ray paths of Central Italy earthquakes 2016-10-30T06:40:19 Mw=6.5 for EDC-CAVI station (red-triangles) and 2016-08-24T01:36:34 Mw=6.2 for EDRB-CTKS (blue-triangles).. 93

Figure 4.57. BHZ components for Central Italy Earthquake 2016-08-24T01:36:34 Mw=6.2 in EDRB-CTKS stations (left) and the fundamental modes (right)........................ 93

Figure 4.58. BHZ components for Central Italy Earthquake 2016-10-30T06:40:19 Mw=6.5 in EDC and CAVI stations (left) and the fundamental modes (right). 94

Figure 4.59. The Rayleigh wave phase velocity dispersion curves between EDRB-CTKS and EDC-CAVI pairs (left). Surface wave inversion results in the (right). Blue line representing northern Marmara and red one shows southern Marmara. Black dotted lines show the initial model (Karabulut et al., 2011). 95

Figure 4.60. Joint inversion results for Northern Stations. Black dotted lines show the initial model (Karabulut et al., 2011). Red lines show the predicted final models. 96

Figure 4.61. Joint inversion results for Southern Stations. Black dotted lines show the initial model (Karabulut et al., 2011). Red lines show the predicted final models. 97

Figure 4.62. Joint inversion results for neighboring stations in northern part of the region (CTKS-BGKT-ISK) and in southern part (EDC-KCTX-ARMT-MDNY). 98

Figure 5.1. ADVT station observed radial RF and synthetic radial RF (upper left). Velocity model for this station with no dipping layer (middle-right). Observed transverse RF and synthetic transverse RF (lower left). 102

Figure 5.2. ADVT station observed radial RF and synthetic radial RF (upper left). Velocity model for this station with a shallow dipping layer. Vertical axis is not plotted to scale for clarity (middle-right). Observed transverse RF and synthetic transverse RF (lower left). 103

Figure 5.3. HRTX station observed radial RF and synthetic radial RF (upper left). Velocity model for this station with a shallow dipping layer. Vertical axis is not plotted to scale for clarity (middle-right). Observed transverse RF and synthetic transverse RF (lower left). 105

LIST OF TABLES

Table 4.1. KOERI Broadband stations, their sensor types and operating time used in the P-waves principal component analysis. 42

Table 4.2. Group 1 events BAZ (45-50) used for calculating P-wave particle motion in ADVT station. 45

Table 4.3. Group 2 events BAZ (101-106) used for calculating P- wave particle motion in ADVT station. 46

Table 4.4. Average angle of deviation for stations of KOERI Network used in the study. 56

Table 4.5. H- κ results for stable and quasi-stable stations.. 69

LIST OF SYMBOLS

κ	Vp/Vs ratio
p	Ray parameter

LIST OF ACRONYMS/ABBREVIATIONS

1D	One Dimensional
2D	Two Dimensional
3D	Three Dimensional
H	Moho Thickness
LAB	Lithosphere-Asthenosphere Boundary
NAF	North Anatolian Fault
NAFZ	North Anatolian Fault Zone
RF	Receiver Function
sec	Second
t	Time
Vp	P wave velocity
Vs	S wave velocity

1. INTRODUCTION

The Marmara Region is a rapidly deforming area in northwestern Turkey associated with a high seismic activity throughout the entire historical time. The major feature of this location is The North Anatolian Fault (NAF), which is a one of the largest transform fault known worldwide. It continues for about 1200 km from Karlıova to mainland Greece, splitting the Eurasian and the Anatolian Plates. Anatolian plate is squeezed between the Eurasian and Arabian Plates, escapes westwards along the dextral NAF and sinistral East Anatolian Faults (EAF) into the NS extending through Aegean (McKenzie, 1972). Current right-lateral slip rate is estimated to be around 20-30 mm/year (McClusky *et al.*, 2000). In the Marmara region, the NAF shows two different properties not recognized in the rest of its 1200 km long fault zone (Okay *et al.*,2000). There are several deep marine basin structures, among which the largest ones are Çınarcık Basin, Central Basin, and Tekirdağ Basin aligned from west to east. The actual morphology of these basins is largely shaped by the activity of the NAF. However, it is still a matter of debate whether their initial emergence is related to the NAF or else they existed well before it. It is also to be noted that the Marmara Fault is not the only branch of the NAF in the Marmara Region. In fact, it splays into a number of other southern branches that are diffused into the western Turkey in a horsetail fashion. In addition to these main branches of NAF, many secondary dextral strike slip fault zones, trending NW or SW directions, are also observed on land. In most cases, they have no apparent relation to the active branch of the NAF. Briefly, the entire region presents a complex deforming zone marked by continuous interaction of the stress partitioning patterns. The Eastern Marmara is a critical section of the NAF, where the relatively simple morphology marked by strike slip deformation gradually turns into a complex zone where the Aegean extension comes in to play its role. The main feature of the Eastern Marmara is the offshore segment of NAF, named The Princes Islands segment or the Çınarcık Fault Zone. It constitutes the northern boundary of the Çınarcık basin and is currently identified as a seismic gap (Bohnhoff *et al*, 2013). Since this location is very close to the large population center of Istanbul, it is considered as a high-risk zone and became a popular scientific target in recent years.

Several seismological, geological, and tectonic studies have been done in the Marmara Region because of its attractive and complex structure, especially after 17 August 1999 Izmit and 12 November 1999 Düzce earthquakes. Among them, the receiver function studies mostly focused on the eastern part of the Marmara Region and especially the land area of this region. Hence, the crustal structure from these studies generally represent structure beneath the land area. After installation of the sea bottom observatory stations in the Marmara Sea, it became possible to study crustal structure beneath OBS stations under the Marmara Sea with receiver function.

There are several on-shore studies targeted to obtain crustal velocity variation and structure of the Marmara Region; Gürbüz *et al*., (1992), Gürbüz *et al*., (2000), Karabulut *et al*., (2003), Barış *et al*., (2005), Zor (2006). Gürbüz *et al*., (1992) determined velocity-depth models beneath 13 stations surrounding the Marmara region by using earthquake travel time data. The study showed that thickness of the crust varies from 27 to 34 km and minimum thickness is seen around Istanbul. According to the study, the thickness increases to the south of Marmara Sea and also it becomes thicker in Trace Region. The results of their study also suggested that there is a gradual increase in crustal thickness from Istanbul to Edincik and crustal structure beneath the Marmara region is too complex. There are also various high velocity seismic zones and some gaps exist in the area. Finally, the study showed that average P wave velocity in the crust and beneath the Moho is 6.2 km/s and 7.9 km/s, respectively. In addition to the study, Gürbüz *et al*., (2000) computed 1-D velocity structure model using 180 events recorded by well distributed land station geometry around the Marmara Sea by using VELEST. Several scientists also revealed the thickness variation of the crust in the Marmara region. Horasan *et al*., (2002) found the total thickness of the crust is 32 km, and the Pg and Pn velocities are 5.9 and 8.0 km/sec, respectively, in the Gulf of Izmit, Marmara region. The shear wave attenuation in the region [Horasan *et al*.,1998; Gök *et al*.,2000] demonstrates that the crustal structure has not a simple pattern in the Sea of Marmara. The geometry of Moho boundary in the Marmara Sea was investigated by many scientists [Necioğlu *et al*., 1981; Gürbüz *et al*., 1992; Özer *et al*., 1996; Kuleli *et al*., 1997] depending on the earthquake data. Furthermore, Guney A.B., and Horasan G. (2002) indicated that the crustal thickness in the Marmara differs from 28 to 34 km. Karabulut *et al*., (2003) published 2D velocity model in the eastern part of Marmara by using seismic tomography technique and they found that the average P-wave velocity is around 5.7 – 5.9 km/s. They also found a relationship between the low velocity zones and strike slip motion of the northern branch of the NAF. They related the results with the complex structure of the region. Another crustal structure study for the Marmara Region is a tomographic inversion method by Barış *et al*., (2005). They showed that western part of NAFZ points out lateral heterogeneity and low velocity zones correspond to alluvial sediments deposits.

Zor (2006) revealed that the 1D velocity models for the stations located at the same tectonic regime in the eastern part of the Marmara region are significantly similar to each other by implementing the receiver function method collected from the 11 broad-band stations. He also observed that the thickening of the crust is from west 29-32 km to east (4.35 km along the NAFZ. The results of this study showed that the average crustal thickness and S wave velocity for the whole region are 31 ± 2 km and 3.64 ± 0.15 km/s, respectively. Denli (2008) investigated 3-D velocity structure of the Eastern Marmara Region from local tomography. In his study, generally low velocities vary between 5.3-5.7km/s through vertical extension of the faults and these extensions of the NAF branches are observed between 2-15 km depths. Mutlu (2011) applied Pn tomography in Turkey included Marmara Region and found the thickness of the crust is nearly 30 - 32 km in that region. Tezel *et al*., (2013) presented that in the Marmara region the the Moho depth varies between 28 and 42 km. In the north of the NAFZ the Moho depth is between 37km-40 km in the eastern Marmara. In addition, in the western part of Marmara, the thickness of the Moho is at around 35 km. Vanacore *et al*., (2013) presented the first plate scale Moho and Vp/Vs ratio map of the Turkey based on H-κ stacking method for approximately 300 stations. According to their study, Moho depth increases from west to east and Western Anatolia is dominated by shallower Moho depth. They also presented the Moho depth about 28-32 km for the Marmara Region. Oruç B., Sönmez T. (2017) show that the Moho thickness varies from 31 km at the northern part of North Anatolian Fault Zone to 39 km in the southern part of the NAFZ.

The Sapanca-Adapazarı zone which is slightly east of Marmara Region is studied in detail by Frederiksen *et al*., (2015). They have used data from a dense array installed temporarily around the NAF. A simple two-layer model is assumed to calculate the Moho depth variations without calculating the receiver functions at individual stations. A grid search for three parameters which are the total crustal thickness which is H, the Vp/Vs ratio of the basement which is k, and the thickness of an overlying sedimentary layer is conducted to evaluate the spacial variation. They found a crustal variation range between 30 km 45 km across the total observation area, with increasing thickness toward to NW direction. This variation seems to be too high considering all previous studies conducted in the area. It is quite likely that this preliminary estimation suffers from large deviations due the observation period being too short, and the SNR being too low from too deep basin effect.

Teleseismic converted waves obtained by P and S receiver functions studies has become a popular method for imaging discontinuities. In recent years, to image faults and shear zones on the fault zones in the absence of seismicity contributes helpful information for lithosphere dynamics. Recently, Schulte-Pelkum and Ben-zion (2012) and Schulte-Pelkum and Mahan (2014) published that faults and shear zones has been detected with teleseismic converted waves by using receiver functions.

This study focuses on the crust of the Eastern Marmara in order to understand of how much the structure is influenced by the activity of the NAF. The methods used during the study are mainly the receiver function analysis and surface wave analysis. The first one provides point wise information while the second one gives an average property over a larger area, which is determined by the wavelength of the surface wave used. Since the study is an attempt to distinguish between fault complexity zones in an otherwise undisturbed area, the point wise information is naturally more intensively used. The surface wave approach is only implemented to introduce a constraint for the average velocity in order to stabilize the receiver function inversions.

In its most general form, the receiver function is a representation of the response of a set of plane layers to an incident teleseismic plane wave. Therefore, the interpretation of most receiver functions underlines the assumption of plane-layered structure. This is often extended to include cases where the structure is approximately plane layered, as in the case of a gently dipping interface (Langston, 1977, 1979). This first part of this thesis concerns the above classical approach, where the simple plane layered (1-D) model is assumed to be valid. In this sense, the earlier work by Zor *et al*., (2006) is updated since more data became available during the 12 additional years that passed since the publication of this pioneering work. The new results bring improvement in terms of more accuracy provided by the stacking of higher number of receiver functions and also a much better azimuth coverage. However, the main contribution comes in terms of additional stations, which increases the spacial resolution by an order of magnitude. The general description of the receiver functions analysis appears in Section 3.1 and the results obtained are in Section given 4.5.

Note that new tools for the interpretations of receiver functions also became available since the publication of the work by Zor *et al*., (2006). CCP stacking and H-k stacking, which are among the best known of such new representation methods, are implemented in this thesis. These new approaches provide a clear view of the general trends of mid-crustal reflection as well as Moho depth throughout the whole Marmara Region. The methodology for this approach is summarized in Section 3.4 and the results are given in Section 4.5.

A well-known limitation of receiver functions analysis is the lack of an anchor point, which constrains the absolute value of the crustal velocities. One way to overcome this problem is to make use of velocity depth profiles obtained from surface wave dispersion analysis. The most elegant way in this context is to do a joint inversion of the receiver functions with the surface wave dispersion data. Accordingly, a joint inversion approach is applied for a more reliable inversion of the receiver functions. This step has the effect of tempering the low velocity trends in the lower crust that were obtained in the previous case with no surface wave. Note that, since the study region is relatively small for a general case of dispersion analysis, two-station approach is used for the surface wave inversion. The methodology for this approach is summarized in Section 3.4 and the results are given in Section 4.5.

The second part of the thesis concerns a more ambitious attempt, which aims at pushing the receiver function analysis to its limits. As already mentioned above, the classical approach for receiver function analysis assumes plane-layered structure, which is often a condition difficult to meet in complex deforming zones. One way to check this assumption is to verify how much energy is leaked to the transversal component of the receiver function. In the presence of large tangential components, a plane-layered structure assumption is inappropriate and could give geologically unrealistic models and incorrect depth information. This approach has been used with the inversion of several receiver functions of related receivers for laterally heterogeneous regional crustal structure (Ammon *et al*., 1990; Owens *et al*., 1984). In particular, whenever a 3-D structure or an anisotropic structure is present, the simple plane-layered model assumption fails. At stations close to the fault zone where complications of both types are encountered, the application of receiver function approach becomes tricky. Langston (1996) showed that the structure of the San Andreas Fault zone greatly affects the teleseismic P arrival, has a profound effect on the calculated receiver functions, and could contribute significantly to the coda waves due to scattering. In this thesis, it is observed that stations away from the fault zones often meet the conditions for a plane-layered model, while the closer ones are complex and needs a detailed analysis. Therefore, all the approaches described up to this point were limited to the stations away from fault zones, which are referred as *Stable Stations*. The second part of this thesis is an attempt to interpret the complexity at the stations close to the fault zones, which in turn, are referred as *Unstable Stations*. The classical paper by Cassidy (1992) is mainly used for the modeling of the complexity. This study provides a systematic survey of receiver function properties for the intermediate case where the layered structure is still valid but the layering is not horizontal. The results presented in the second part of this thesis, make use of the results presented by Cassidy. In particular, since a rich dataset is now available for the Eastern Marmara, covering a large time span with a high spatial sampling, an attempt is made to interpret the receiver functions by introducing dipping layers. In this context, the azimuthal variation of the receiver functions is investigated by reference to the non-horizontal layering. In this situation both the radial and transversal components are taken into account. The velocity inversion is achieved by forward modeling and visual inspection of the comparison results. The convergence of the off-line iteration is completely based upon manual adjustments and depends heavily upon the experience of the analyst. The inversion was successful for two out of the three sites, which were identified as being unstable. The results of this quasi 3-D modeling are given in Section 4.5.

2. TECTONICS OF EASTERN MARMARA REGION

The Marmara Region is located in the northwest Turkey and it is situated at the junction of the Aegean, western Anatolian, Thrace and Black Sea Regions. This is tectonically complex area, marking the transition zone between north-south extensional regime of the Aegean Region and the strike slip regime of the NAF. This fault zone is the most important feature of the Marmara Region and presently determines the entire evolution of the local structure.

NAF is considered to be one of the largest intercontinental transform worldwide. It has a well-recorded seismic activity that extends for about 1200 km from Karlıova junction to mainland Greece, as shown in Figure 2.1. Together with the sinistral East Anatolian Fault, it marks the boundary of the Anatolian plate, which escapes westwards between the converging Eurasian plate and Arabian plate, into the NS extending Aegean (McKenzie, 1972). The rate of motion of the Anatolian Plate increases from east (15-20 mm/yr) to the west (20-30 mm/year) as shown in Figure 2.2. (Reilinger *et al*., 2006, 2010).

Several large historical earthquakes were observed in its total length, leaving only a few locations where the stress is not yet released. NAF was activated many times along its total length during the last century length by large earthquakes (Stein *et al*., 1997). This sequence of large events is considered to be the best example of stress transfer and static triggering processes that is observed in such detail in instrumental time. The chronological ordering of the events implies a western propagation of the rupture, of which the most recent one is the 17 August 1999 Izmit earthquake with magnitude Mw=7.4. This was a devastating earthquake and caused the highest damage and loss of human life in the history. The next major event is predicted to occur in the neighboring segment, i.e. Marmara Sea Segment, due to the accumulated stress and no significant earthquake was detected for more than a century (Aktar, 2017).

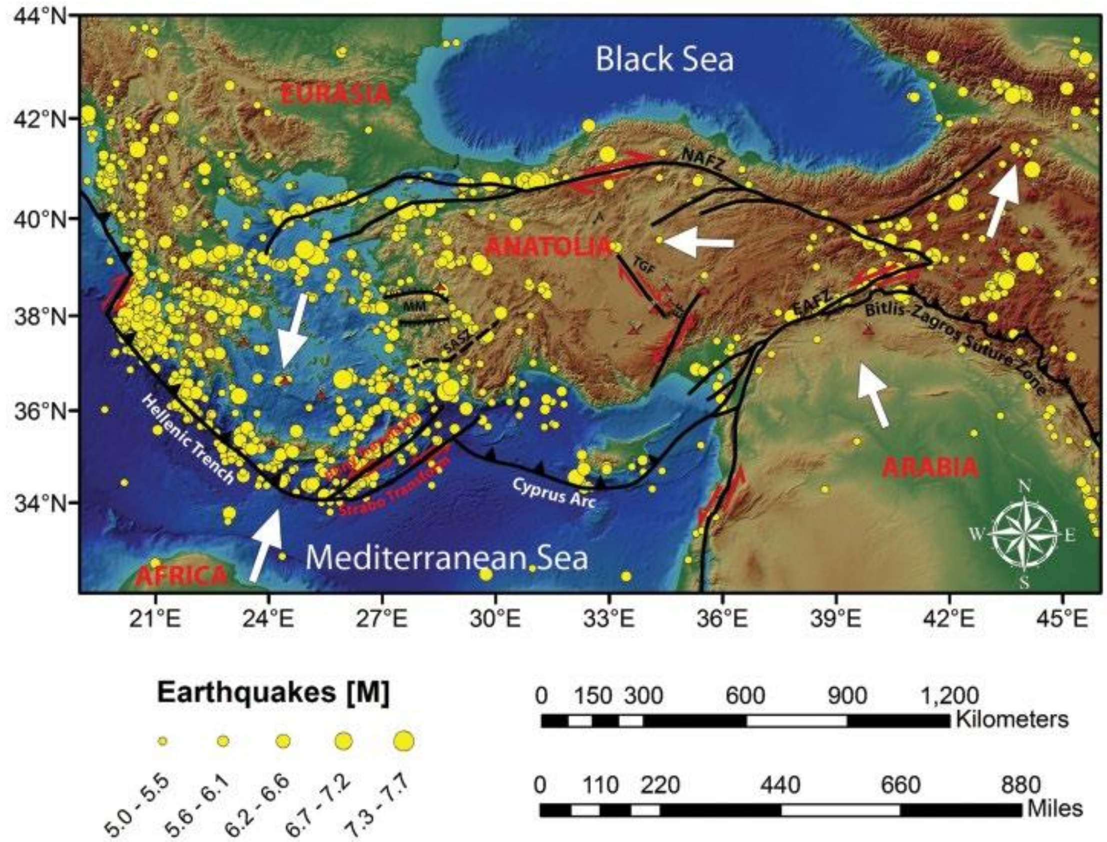

Figure 2.1. The digital elevation map of Turkey and surroundings. Black lines are the main active faults. White arrows show the movement of the tectonic plates. Yellow circles are location of the earthquakes M>5.0 since 1950 (Çemen and Yılmaz, 2017).

The exact path that the NAF in the Marmara Region is not known, except for the Izmit Bay, which ruptured during the 1999 event. The seismicity pattern and the morphology clearly indicates that there sare more than one branches that run parallel to each other in the western directions. These are the Çınarcık Fault representing the northern Branch Branch, the Yalova-Mudanya Branch and the Iznik-Mekece-Gemlik Branch. Figure 2.3 and 2.4 show the seismicity patterns and the focal mechanisms of Eastern Marmara Region, respectively. All branches are known to produce large events in the history. It is generally believed that the most northern Branch, which crosses the central axis of the Marmara Sea, will be the site for the next large earthquake. At this stage, the key point of the debates is how the stress is partitioned among these sub-parallel branches. This constitutes the main question to answer before making any estimate about the size of future events. GPS data in recent years provides clues about the most recent strain patterns. However, for a long-term estimate, morphology and structure becomes the main source of information. In this context an essential question is to determine to what extend the fault activity influences the structure in the long term. Yılmaz (2017) has identified 4 morphotectonic components for the Eastern Marmara (Figure 2.5):

1. The North Anatolian Transform fault zone
2. The Marmara Sea Basin
3. The Thrace-Kocaeli peneplain (and the Istanbul plateau)
4. The Bursa-Balıkesir plateau

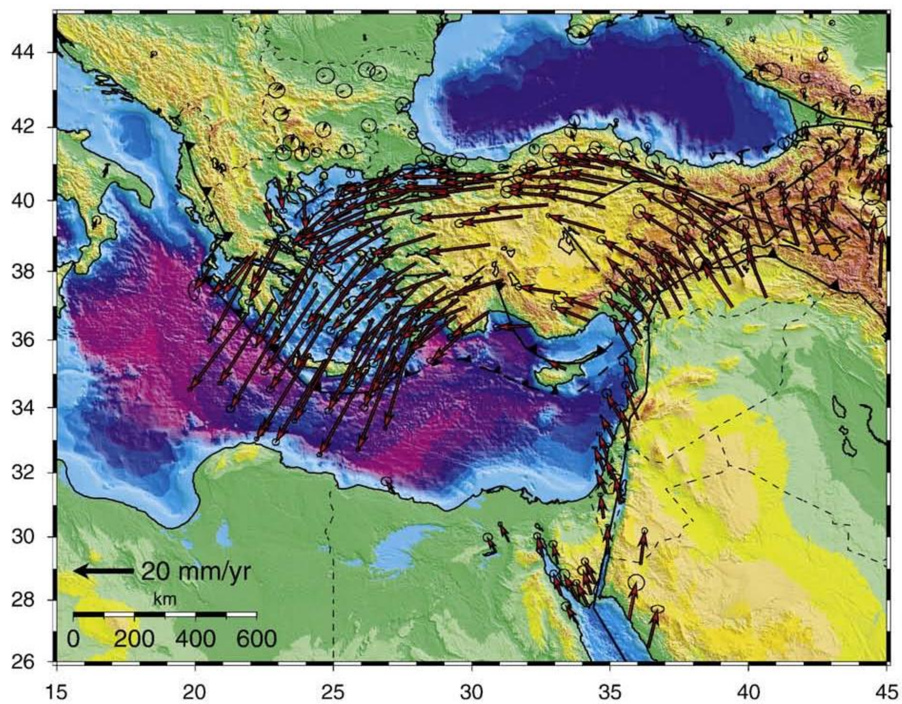

Figure 2.2. GPS velocity vectors with respect to Eurasia. (Reilinger et al., 2006).

In particular, the first two, namely North Anatolian Transform Fault Zone together with the Marmara Sea Basins, constitute a young structural axis in the EW direction, which separates the last two terrains, the peneplain and the plateau. The more important aspect of this morphological classification is that it is closely related to the tectonic history of the region. More interestingly, this young structural axis constitutes at the same time, the separation line of two different tectonic units, and namely the Eurasian and the Anatolian Plates.

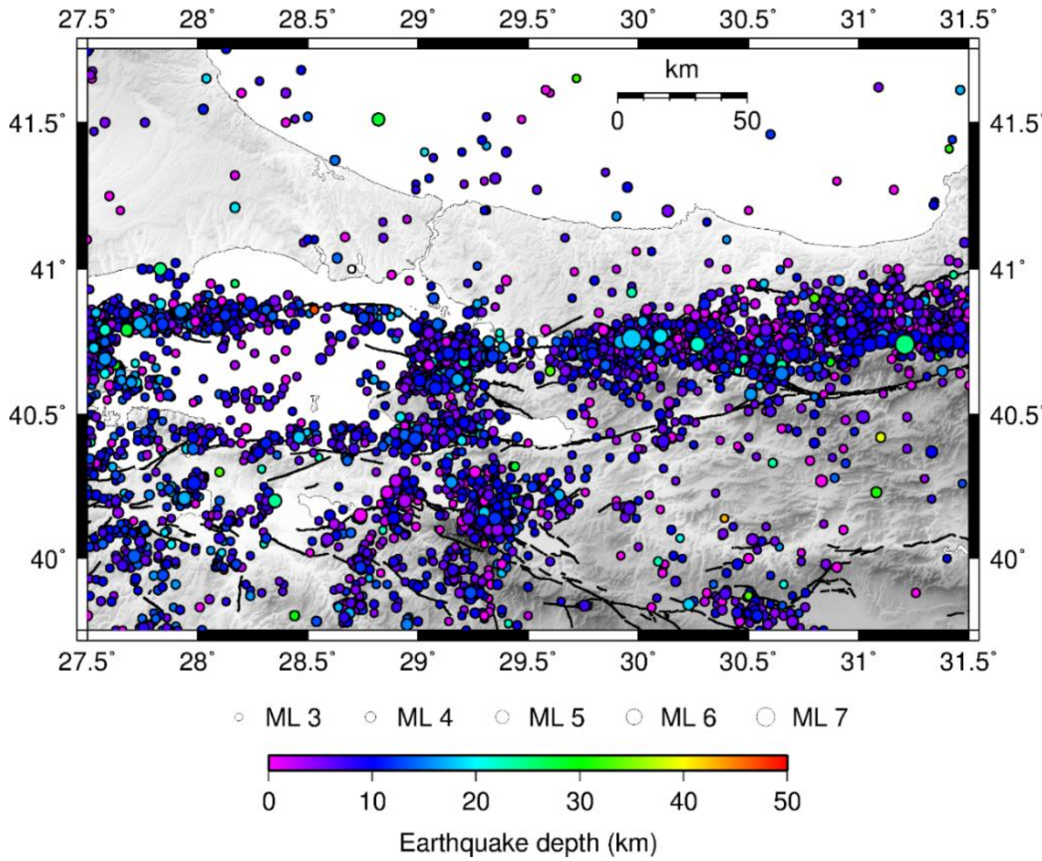

Figure 2.3. The seismicity map of the study region during 1900-Present (KOERI catalog). Fault lines are taken from MTA.

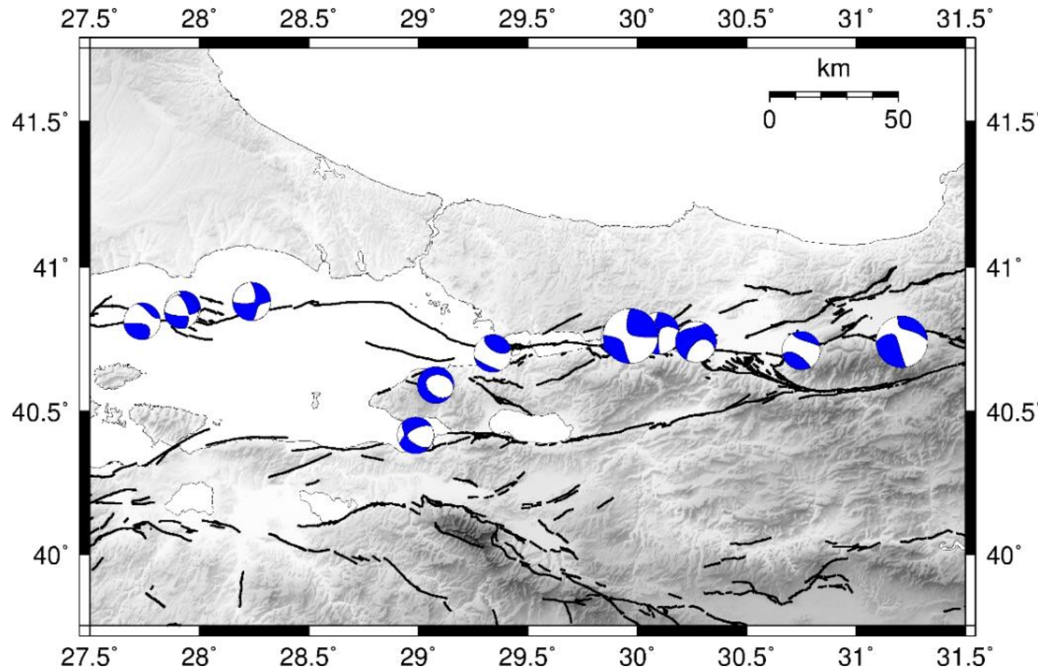

Figure 2.4. Focal Mechanism of 15 events (Mw≥4.8) in the Marmara Region since 1983. (Global CMT catalog). Fault lines are taken from MTA.

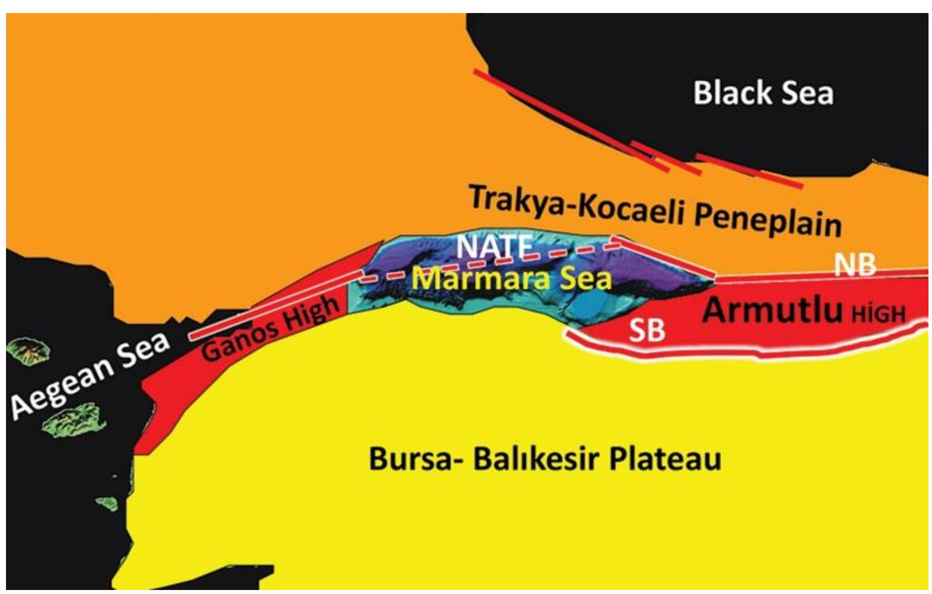

Figure 2.5. Morphotectonic components of the Marmara region (Yılmaz, 2017).

On the North, the Thrace-Kocaeli peneplain with a rather smooth topography is considered as a member of the Eurasian Plate, where else the Bursa-Balıkesir plateau is a member of the Anatolian Plate. The tectonic units representing the plates are shown in Figure 2.6 which is taken from Okay (2008). Looking in more detail, the Thrace-Kocaeli peneplain shows two different roots in the east and west. The eastern side is represented by the Istanbul zone, which is comprised of Precambrian crystalline basement that gradually transforms to a continuous transgressive sedimentary succession. The sedimentary series ranges from Ordovician to Carboniferous, and contains deformed traces of the Hercynian orogeny (Görür *et al*., 1997; Dean *et al*., 1997). As one goes west, around Silivri - Büyük Çekmece line, the Istanbul zone disappear under the Istranca-Rhodopian terrane. This unit crops out all along the southern, western and northern of the young Thrace Basin. It is represented by a crystalline basement, which includes metamorphic rocks interrupted by Permian granites (Aydın, 1974; Okay and Tuysüz, 1999). During the mid-Jurassic, both basement and its Triassic succession were regionally metamorphosed and then overlain by Cenomanian conglomerates and shallow marine limestones. The top is covered by Senonian andesites and intruded by associated granodiorites as in the case of the Istanbul Zone (Moore *et al*., 1980).

On the South of the NAF axis, the Anatolian Plate is represented by the Sakarya Continent. This is defined by a Triassic subduction accretion complex which is called Karakaya Complex. It consists of strongly deformed and partly metamorphosed basement. During the latest Triassic the final phase of deformation occurred and it was followed by sedimentation of Jurassic continental to shallow-marine deposits, Cretaceous carbonates, and finally by Senonian andesites (Altıner *et al*., 1991; Tüysüz, 1993). The whole series can clearly be observed along the deep canyon carved by the Sakarya River.

Figure 2.6. General geological structure of the Marmara region and its surrounding areas (Okay, 2008).

The fact that the axis formed by the NAF and the Marmara Basins constitutes a separation line between two tectonic units, lead to the hypothesis that the suture constitutes a weakness zone, which facilitated the formation of the fault. It is therefore assumed that structural units located on the north and the south of NAF should constitute two totally different worlds, with entirely different characteristics. Many studies focused on proving that the properties of the crust vary considerably across the fault (Kahraman *et al.*, 2015; Frederiksen *et al.*, 2015). Receiver functions studies were the most popular tool for these types of studies. This is also one of the motivations that laid ground for the present thesis. This work however showed that although some structural differences can be detected for the north and south of NAF, this is not substantial enough to be related to the origin of the plates on both sides. The detected differences are minor and are probably due to more recent tectonic processes such as the Aegean extension, etc.

3. METHODOLOGIES

3.1. Receiver Function

Receiver function technique is one of the widely used tools to determine crust and upper mantle structure. The P wave on the telesismic waveforms involve information showing the source orientation, near source structure, source time history, mantle path effect, and the structure in the vicinity of station. Receiver functions are time series that are calculated from 3 component seismograms and present relative response of Earth structure below a station. A receiver function is a combination of P-S converted waves that are reverberating beneath the station and only involves information about the structure in a local sense (Ammon, 1991). In receiver function technique, teleseismic waveforms which include a series of reflection, refraction, and conversions. The basic idea of this method is that incoming P wave is converted into SV wave at Moho discontinuity due to the sharp velocity contrast and these converted waves arrive to the station after P wave. The trace of receiver function contains the direct P wave arrival that shows how the initial P wave is divided into radial and vertical components at the surface. This first arrival (direct P) is followed by a Ps phase having a positive polarity which result from obvious velocity contrasts such as the Moho discontinuity and later PpPms, PpSmS+PsPms, and PsSms reverberated phases between the surface and the impedance contrasts as shown in Figure 3.1.

The amplitudes of the pulse arrivals for a receiver function depend on the incidence angle of the P-wave and the amount of the velocity contrasts generating the conversions and multiples. Moreover, the arrival times of the converted phase and multiples rely on the depth of the velocity contrast, the P and S velocity between the contrast and the surface, and the ray parameter. In addition to all, the amplitudes of the later arrivals and their frequency content depend on the nature of the velocity transition (Ammon *et al*., 1990).

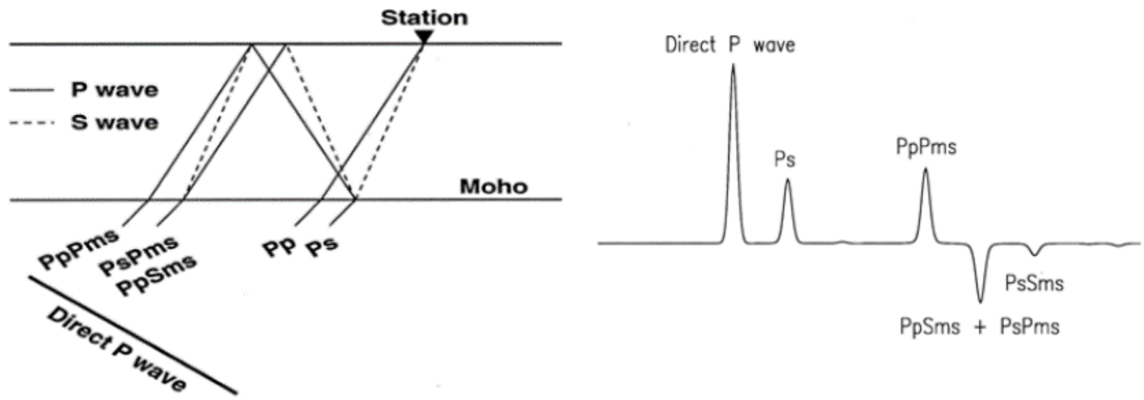

Figure 3.1. Phase arrivals of teleseismic incident P wave for a layer over a half space model (left). Receiver function traces that show direct P, Ps conversions and its multiples, respectively (right).

The arrival times and amplitude of pulses in a receiver function provide knowledge about the travel time from the interface to the surface and the velocity contrast. However, the receiver function inversions for S wave velocity structure are non-unique considering there is very little absolute velocity information contained in the receiver functions. It brings about the non-uniqueness problem known as the velocity-depth trade-off due to the lack of velocity information (Ammon *et al*., 1990). This velocity-depth trade-off appears because receiver function technique is a differential method consisting of no absolute travel time information. A fast and thick layer can produce the same average differential arrival time for a slow and thin layer. Ammon *et al*., (1990) showed this velocity-depth trade-off by for the initial velocity model dependency of the inverted velocity models.

Receiver functions can be used to determine the geometry of seismic reflectors, the shear wave velocity variation within the crust and the upper mantle, the character of the crust-mantle boundary, and the assessment of the Poisson ratio in the crust.

3.1.1. Receiver Function Analysis

In receiver function studies, teleseismic events ranging from 30° to 90°are frequently used because P waves are steeply incident and dominate vertical component of ground motion while Ps converted phases are recorded on the horizontal component (Cassidy, 1992). Generally, three component broad-band seismometers are preferred to use because they have a flat velocity response throughout most of the lower frequency bands in contrast to the spectrum of short period seismometers.

After choosing the teleseismic events, the next step is filtering of the waveforms to gather obtain high quality data and eliminate high frequency content which are affected by small-scale heterogeneities. 0.1 Hz-1 Hz or 0.05 Hz-1 Hz are appropriate for filtering of teleseismic events. Another step is windowing of seismograms and it depends on the discontinuities of interest. In this study, 60 seconds before P wave and 90 seconds after P wave is commonly used. The following step in receiver function analysis is to rotate the filtered and windowed teleseismic events. By using the back azimuth, the angle measured between the vector pointing seismic station to source and seismic station to north (Scherbaum and Johnson, 1992), the North-South (NS) and East-West (EW) components can be rotated into the radial and tangential components, respectively (Figure 3.2). I use the ray based (RT) system since P to SV converted phases are radially polarized and observed on radial component, while P to SH converted phases are transversely polarized and observed on tangential component.

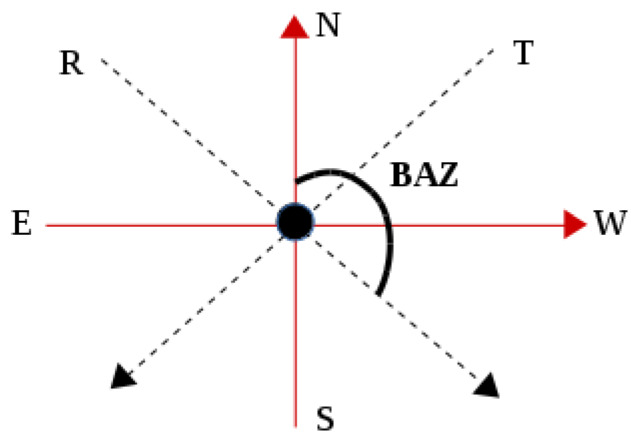

Figure 3.2. NS, EW, radial (R), transverse (T) components and back-azimuth (BAZ)

The final step in receiver function analysis is to obtain radial and tangential receiver functions from filtered, windowed, and rotated teleseismic waveforms as illustrated in Figure 3.3. By applying deconvolution process which means spectral division of the radial and transverse components to vertical component, the estimation of receiver functions can be done. In addition, the aim of this procedure is to eliminate the effects of the near source ray path and instrument response in order to obtain the signal which includes the first P wave, P-S wave conversions, and locally generated reverberations under the station. Deconvolution can be done either in frequency domain which was proposed by Langston (1979) or in time domain proposed by Ligorria and Ammon (1999). The latter is more suitable for noisy observations to estimate more reliable results. This deconvolution method is a least square minimization of the difference between observed and predicted horizontal waveform traced by the convolution of updated spike train which is processed iteratively with the vertical waveform (Ligorria and Ammon, 1999).

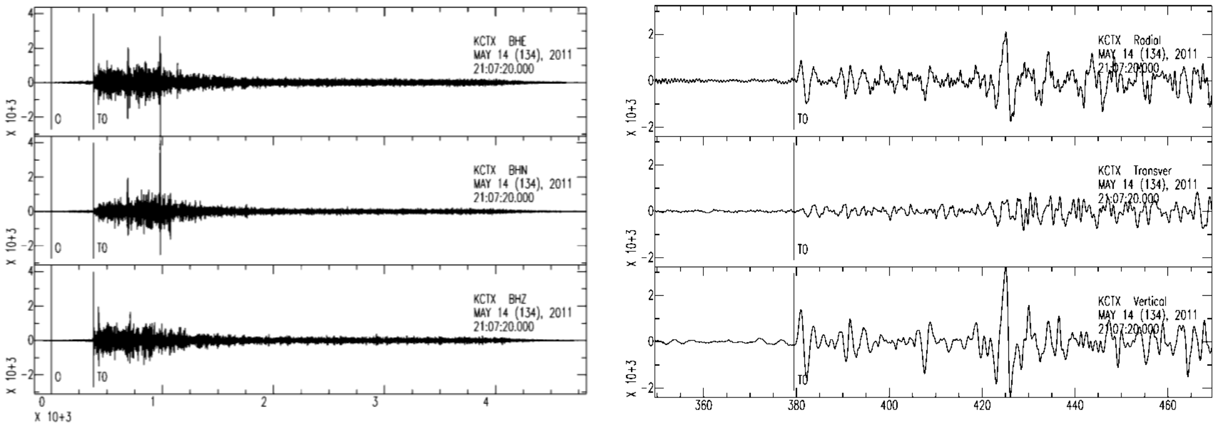

Figure 3.3. 2011-05-14T21:07:20 Afghanistan Earthquake 3 components waveform (upper) and rotated components (below).

The vertical component is cross-correlated with radial component to calculate the lag of the first and largest spike in the receiver function. The spike amplitude is measured by solving a simple equation placed in Kikuchi and Kanamori (1982). Then the convolution of the current measurement of the receiver function with the vertical component is subtracted from the radial component, and the procedure is repeated to predict other spike lags and amplitudes. Throughout the iteration, the misfit between the radial component and the vertical and receiver function convolution is decreased. This process will continue until the reduction in misfit with additional spikes becomes insignificant. One of the main advantages of this approach is that the significant features in the original signal can be extracted one by one, and preserved as much as possible in resultant receiver functions (Ligorria and Ammon 1999). In this study, this technique is pursued to implement the receiver function analysis.

3.2. H-κ Stacking Technique

In receiver function, Ps converted phase and reverberated phases PpPs and PpPs + PsPs indicate relevant information in respect to the crustal properties such as H and Vp/Vs ratio. They are significant parameters to understand the crustal structure, which can be determined beneath a station if phases are existed clearly.

A useful technique to calculate depth and Vp/Vs ratio became popular in the last decade is called H-k stacking method proposed by Zhu and Kanamori (2000). It is assumed in this method that the crust is laterally uniform and consisting of laterally horizontal layers.

The time difference between Ps and direct P can be used in receiver function analysis to estimate average crustal thickness,

where H is the thickness, p is ray parameter, Vp and Vs are average crustal velocities, and t is the time difference between P and Ps arrival times.

$$\boldsymbol{H = \frac{t_{Ps}}{\sqrt{\frac{1}{V_s^2} - p^2} - \sqrt{\frac{1}{V_p^2} - p^2}}} \tag{3.1}$$

Additionally, the crustal thickness can be calculated by using the arrival time of the reverberated phase PpPs,

$$\boldsymbol{H = \frac{t_{PpPs}}{\sqrt{\frac{1}{V_s^2} - p^2} + \sqrt{\frac{1}{V_p^2} - p^2}}} \tag{3.2}$$

and also for other reverberated phases PpSs + PsPs,

$$\boldsymbol{H} = \frac{\boldsymbol{t_{PpSs+PsPs}}}{\boldsymbol{2}\sqrt{\frac{\boldsymbol{1}}{\boldsymbol{V_s^2}} - \boldsymbol{p^2}}} \tag{3.3}$$

It is not so easy to observe converted Ps phase and its multiples which are PpPs and PpSs + PsPs on a receiver function trace because of background noise in real situations, scattering energy from crustal heterogeneities, and P-S conversions from other discontinuities. Hence stacking multiple events in the time domain might be helpful in order to enhance the signal to noise ratio.

H-κ stacking technique is developed by Zhu and Kanamori (2000). This method sums the amplitudes of receiver function at the predicted arrival times of Ps, PpPs and PpSs + PsPs for different crustal thickness H and κ values. Figure 3.4 indicates that lines demonstrating the Ps pointing Moho boundary its multiples which are PpPs and PpSs+PsPs to the stacked amplitude as a function of crustal thickness and Vp/Vs ratio. In this technique, a transformation is made from the time domain receiver functions into the H and Vp/Vs domains with assuming a starting average P wave velocity. H-κ stacking is described as,

$$\mathbf{s}(\mathbf{H} - \boldsymbol{\kappa}\,) = \sum_{\boldsymbol{i}} \boldsymbol{w_1\, rf_i(t_1) + w_2 rf_i(t_2) - w_3 rf_i(t_3)} \tag{3.4}$$

where rfj(t) is the radial receiver function with j ranging from 1 to the total numbers of waveforms. The thickness is H the Vp/Vs ratio is κ. t1, t2, and t3 are the predicted Ps, PpPs and PpPs+PsPs arrival times showing crustal thickness. The w1, w2, and w3 are the weighting factors and w1 + w2 + w3 =1

The weight for Ps should be greater than the sum of the weights of PpPs and PpPs + PsPs to balance the contribution for three pulses according to the Zhu and Kanamori (2000). They presented weighting factors as 70%, 20% and 10%, respectively in their study. They also stated that Ps has the highest S-N ratio, therefore it should be given a high weight factor than Ps, PpPs and PpPs + PsPs. When these phases are stacked coherently, H and κ are better estimated.

An advantage of this method is that multiple teleseismic waveforms can be conveniently analyzed. In addition, estimation of crustal thickness or Vp/Vs ratio do not contain effect of lateral variations since Ps conversion point is very close to the station. Moreover, average crustal model is obtained by stacking receiver functions from different distances and directions, and there is no need to pick arrival times of different conversion phases (Zhu and Kanamori, 2000).

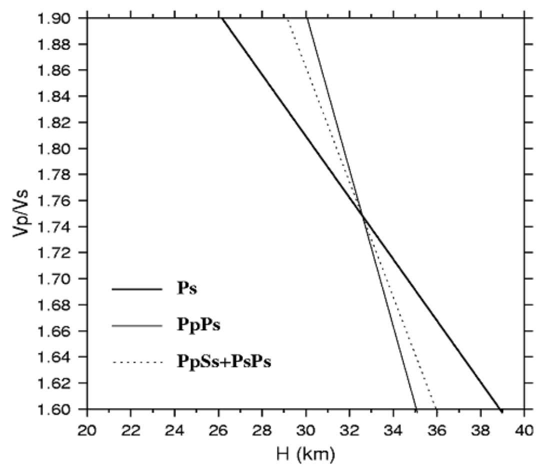

Figure 3.4. Curves demonstrating the contributions of Ps and its multiples PpPs and PpSs+PsPs to the stacked amplitude as a function of crustal thickness and Vp/Vs ratio.

On the other hand, the method has some limitations. One of them is that Moho discontinuity is assumed planar layer, homogeneous, and there are no lateral variations. However, if Moho is dipping then it affects Vp/Vs ratio that indicates lateral heterogeneities. Dipping of this interface will cause travel time difference with respect to the horizontal interface (Ligorria, 2000). Rays travelling along or down dip direction, the arrival times of pulses are smaller than those generated at flat Moho boundary and cause the deviation of the H-κ stacking results. Furthermore, according to Cassidy, 1992; Liggoria, 2000; Julia, 2004 if Moho boundary is gradually increased instead of a sharp Moho discontinuity this type of boundary can make the energy from the boundary interaction phases that spread in time so that the corresponding pulses decrease in amplitude and increase in width. Moreover, converted phases and multiples from intra-crustal discontinuities could overlap with the real Moho Ps converted phase. Especially in sedimentary units where the multiples from the sediment–bedrock interface overlap in time with the Ps converted phase at the Moho (Cassidy, 1992; Zelt & Ellis, 1988). As a result, time shift of the Ps peak may cause unrealistic thickness and Vp/Vs ratios.

3.3. Surface Wave Analysis

Seismic waves are the waves that travel through the earth which are caused by the release of energy from earthquakes or explosions. Normally, they are classified as body waves and surface waves in terms of the different properties, such as the wave speed and the direction of wave propagation. For example, the first kind of body wave is the P-wave (or primary wave) and the second type of body wave is the S-wave (or shear wave), which propagate through the interior of the earth, whereas, the surface waves propagate along the surface of the earth, and decay in amplitude rapidly with increasing depth. The strongest arrivals on a broadband seismogram for shallow earthquakes are the surface waves, which arrive at a seismic station after the body waves, and usually cause heavy damage and destruction to the structures.

3.3.1. Rayleigh Wave and Love Wave

Similar to body waves, surface waves are also separated into two categories: Rayleigh waves and Love waves characterized by particle motion, respectively. Rayleigh waves, which are caused owing to interference of P and SV waves near the free surface. They are polarized in the vertical (SV) plane of propagation and due to the phase shift between P and SV. Rayleigh waves propagate along the free surface and their amplitudes decay exponentially in the vertical direction. Particle motion for Rayleigh waves at the surface follow a retrograde elliptical orbit and counter clockwise. Their propagation is strongly determined by surface topography. Rayleigh waves travel relatively slower than other seismic waves in most cases and are usually seen as the last seismic waves on the vertical components on seismograms.

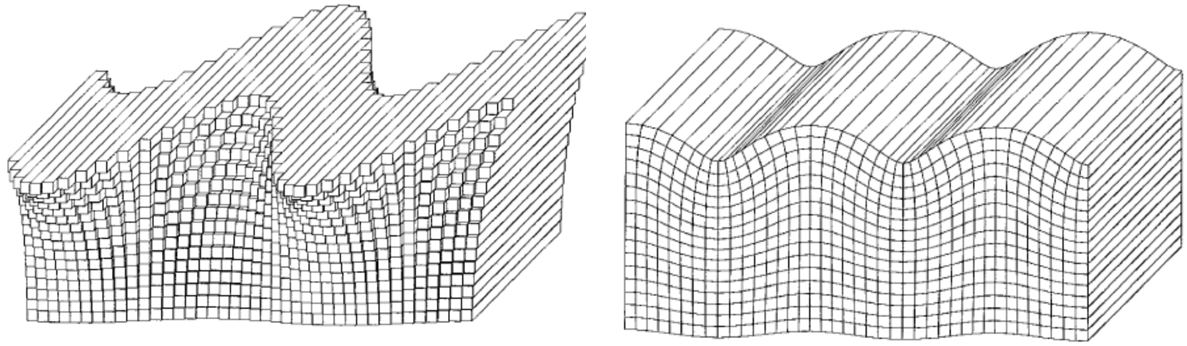

Figure 3.5. Displacements caused by horizontally propagating fundamental Love (left) and Rayleigh waves (right). In both cases the wave amplitudes decay strongly with depth (Shearer, Introduction to Seismology, 1999).

Love waves which are another type of surface wave are polarized in the horizontal plane and perpendicular to the direction of wave propagation. In contrast to Rayleigh waves, they do not show vertical motion (Figure 3.5). Love waves generally travel faster than Rayleigh waves.

An important characteristic of surface waves is the dispersion, which means the waves travel with different speeds at the different periods.

3.3.2. The Dispersion of Surface Waves

One of the most significant characteristics of surface waves is dispersion, which plays an important role in quantitative studies of crust and upper mantle structures. Surface waves are normally dispersive in a vertically heterogeneous medium which means that different velocities are corresponding to different periods. Surface waves with longer periods or long wavelength travel faster than those with shorter periods, as they are sensitive to the deeper structure of the earth. Therefore, the velocity of the surface wave has a function which is related to the period contrary to the depth.

If a sinusoidal wave propagates with a constant wavelength, every point on this wave will shift with the phase velocity (c). On the other hand, group velocity (U) represent the speed of the envelope of the wave packet propagates through space. Figure 3.6 shows the comparison the phase velocity and the group velocity. Phase velocity can be defined as:

$$\boldsymbol{c = \frac{w}{k}} \tag{3.5}$$

ω refers to the angular frequency. k is the wave number, and k = 2π/λ. The relation is,

$$\boldsymbol{\omega = \omega(k)} \tag{3.6}$$

The group velocity is related to the phase velocity by,

$$\boldsymbol{U = \frac{dw}{dk}} \tag{3.7}$$

From the relations above,

$$\boldsymbol{U = \frac{d}{dk}(ck) = c + k\frac{dc}{dk} = c - \lambda\frac{dc}{\lambda}} \tag{3.8}$$

where λ is the wavelength. The phase velocity increases with increasing the wavelength in the normal cases. Hence, the group velocity is slower than the phase velocity because dc/dλ are positive.

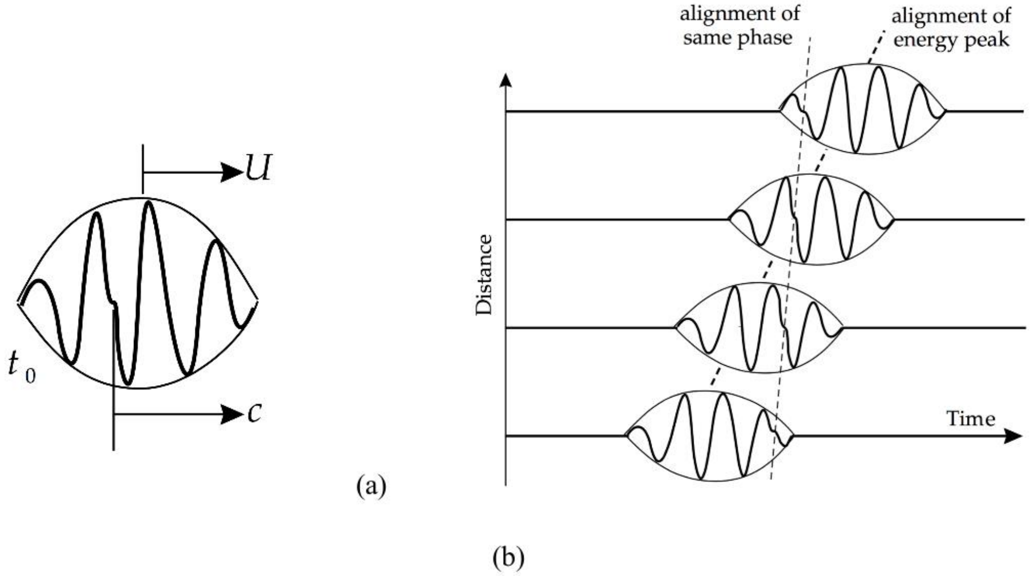

Figure 3.6. The comparison of the group velocity (U) and the phase velocity(c). The envelope of the wave packet propagates with the group velocity, and the phase of any component of the wave propagates with the phase velocity. (b) The arrivals of a dispersive wave at different receivers (Lowrie, 2007).

3.3.3. Rayleigh Wave Dispersion

The Rayleigh waves dispersion studies is widely used in the studies of Earth structure in the recent years Brune & Dorman 1963; Knopoff 1972; Gomberg *et al*., 1988; Debayle & Kennett 2000). Group velocity and phase velocity information may be obtained from, using single-station or two-station methods. In this study, Rayleigh wave phase velocities are estimated for an earthquake between pairs of stations situated in common great circle path which means that the contribution of the source phase to the observed phase is the same. In this method, the amplitude and phase term which are common to both seismograms are extracted (Darbyshire, F.A. *et al*., 2004). The advantage of the two-station study also has that only the structure between the stations contributes to the dispersion curve, instead of the entire source station path. This is a significant factor in this study.

<u>3.3.3.1. Two-Station Method.</u> Rayleigh wave fundamental mode propagation was studied in Marmara Region and calculated inter-station phase velocities applying the two-station method developed by Herrmann (1987). In order to eliminate the propagation effects between the source and the near-station, the near-station waveform is deconvolved from the far-station waveform in the two-station method. The assumptions of a two-station technique are that

a) single surface mode is observed at both stations,
b) that both stations be on the same great circle path which means that the contribution of the source phase to the observed phase is the same, and that there be good signal-to-noise in the observed signal, which requires that the path from the source to the stations not be one of low amplitude (Herrmann, 1987).

3.4. Joint Inversion Technique

Many surface wave dispersion and teleseismic P wave receiver functions studies for the S wave velocity structure has been studied to cover constraints the crustal and upper mantle structure. The first receiver function inversion study was performed in the 1980s (Owens *et al*., 1984), and many other studies have figured out (Mangino *et al.*, 1993; Cassidy & Ellis 1993; Sheehan *et al*., 1995; Sandvol *et al*., 1998; Julia *et al*., 1998). On the other hand, inversion of the surface wave dispersion, introduced much earlier (McEvilly 1964), and remains a useful technique to investigate Earth structure (Nolet 1977; Dost 1990; Bourjot & Romanowicz 1992; Badal *et al*., 1996; Mokhtar *et al*., 2000).

A teleseismic P wave receiver function is especially sensitive to the S-wave velocity structure at interfaces and vertical travel times (Julia *et al*., 2000). It provides site information and is sensitive to both dip angle and direction of interface (Cassidy, 1992). Receiver functions constrain shear velocity contrasts of interfaces located in the medium and the relative travel time of the converted waves reverberated between those interfaces, so that interpretations of such data may carry an apparent depth–velocity trade-off (Ammon *et al*., 1990). In contrast, surface wave dispersion analysis produces better estimations of average shear velocities at different depth ranges.

The joint interpretation of surface wave dispersion and teleseismic P-wave receiver functions seems to provide tighter constraints on the shear velocity structure than either technique individually. The ultimate velocity model from the joint inversion should be sensitive to both interface sharpness and velocity undulations of the crust. Previous research had shown that this method provides stable constraints to subsurface structure than either individual data set (Julia *et al*., 2003; Shen *et al*., 2012).

The joint inversion attempts to simultaneously invert receiver functions and surface wave dispersion estimation for the S wave velocity model. It is pursued Herrmann and Ammon's (2002) instructions based upon an iterative damped least-squares to implement the joint inversion. The inversion procedure gives smooth velocity models with a minimum number of sharp velocity contrasts and smoothness is handled by a damping value. The eventual velocity model should minimize the joint prediction error, which is shown as follows;

$$E = \frac{(1-p)}{N_r}\sum_{i=0}^{N_r}\left(\frac{o_{r_i} - P_{r_i}}{\sigma_{r_i}}\right)^2 + \frac{p}{N_s}\sum_{j=0}^{N_s}\left(\frac{o_{s_j} - P_{s_j}}{\sigma_{r_j}}\right)^2 \tag{3.9}$$

where O indicates observed data, and P indicates to predicted data. N represents the total number of the observations for each individual data set. σ is the standard error. Subscript r and s show the two data sets, receiver function and surface wave dispersion, subsequently. Subscript i refers to the receiver function at time ti and j shows the jth surface wave dispersion. The p factor, also called the influence factor, is an a priori parameter that indicates the relative contribution of each data set to the solution. The value of p should be between 0 and 1. If p = 0, the receiver function will be the only data set to contribute to the resultant solution. On the contrary, if p = 1, the surface wave dispersion will be the only data set for the inversion. The computer program joint96 performs the joint inversion method (Herrmann and Ammon, 2002). The 1-D S-wave velocity models are directly calculated from the program.

3.5. CCP Stacking

A common seismological method is to utilize receiver functions, associated with converted P and S waves at horizontal interfaces to figure out the existing of vertical offsets of the Moho across large faults (Burdick and Langston, 1977; Jones and Phinney, 1998; Zhu and Kanamori, 2000; Wittlinger *et al*., 2004). Receiver function arrivals can present a strong back azimuth dependence on events in tectonically active areas (Schulte-Pelkum and Mahan, 2014). In order to represent receiver function results for crustal thickness, a conversion must be made from the time domain into space domain with an initial velocity model. This is usually performed with 1D velocity models.

The Moho interface is often build by using receiver functions in a common conversion point (CCP) stacking that constructs a 3D volume throughout a study region by averaging receiver functions that fall in a grid cell after projected along ray paths assuming an initial velocity model The amplitudes and polarities in the 3D volume demonstrate the section of discontinuities in the crust and mantle, successfully accounting for back azimuthal alterations beneath a station. The grid spacing in the CCP method is commonly user-defined. In this study, obtained CCP stacks are binned in a 3D grid and 1 km cells. Common Conversion Point (CCP) stacks are estimated using 1-D AK135 velocity model extracted for each ray. The CCP stacks are evaluated with volumetric plots using PARAVIEW program in this study.

In order to estimate the path of the incoming rays to generate sets of effective 1D velocity models representative of the structures sampled by each teleseismic ray, 3D ray tracing of Sambridge and Kennett (1990) in the combined velocity model is used. Then the velocity structure is extracted along each path as a function of depth Vp(z) and converted to Vs(z) using Vp/Vs = 1.732. It is excluded to the study that visually obtained a total 7884 radial component receiver functions at 26 stations functions with RMS misfit between the final estimated and observed radial waveforms larger than 70%.

4. DATA ANALYSIS AND RESULTS

4.1. Data and Seismic Stations

Teleseismic data which is collected during a 12 years period between 2005 and 2017 is processed in this study. Figure 4.1 shows stations used in this study. There are two primary sources for the data. The first one is the permanent seismic array (PIRES) located close to the main fault branch offshore of Istanbul. PIRES stations are distributed over 17 different locations on the Prince Islands. Figure 4.1 shows them as a cluster of yellow triangles inside the Izmit Bay. Yassiada and Sivriada, which are the two outermost ones of Prince Islands, include two dense subarrays with 5 stations each. Stations at both subarrays have a cross-shaped distribution with an aperture of about 300 m. The average station spacing within each PIRES subarray is 191 m. These two subarrays, together with the single station on the Balıkçıada are the three land locations, which are closest to the Çınarcık Fault. In addition to PIRES array, 15 permanent stations operated by KOERI are included in the analysis. They are located between 40.1°-41.5° N and 27.5°-30.0° E and cover most part of the Eastern Marmara. Approximately 1500 teleseismic events were chosen from the USGS earthquake catalog according to magnitudes (Mw>5.5) and epicentral distances (ranging between 30° and 90°). The distribution of events is given in Figure 4.2.

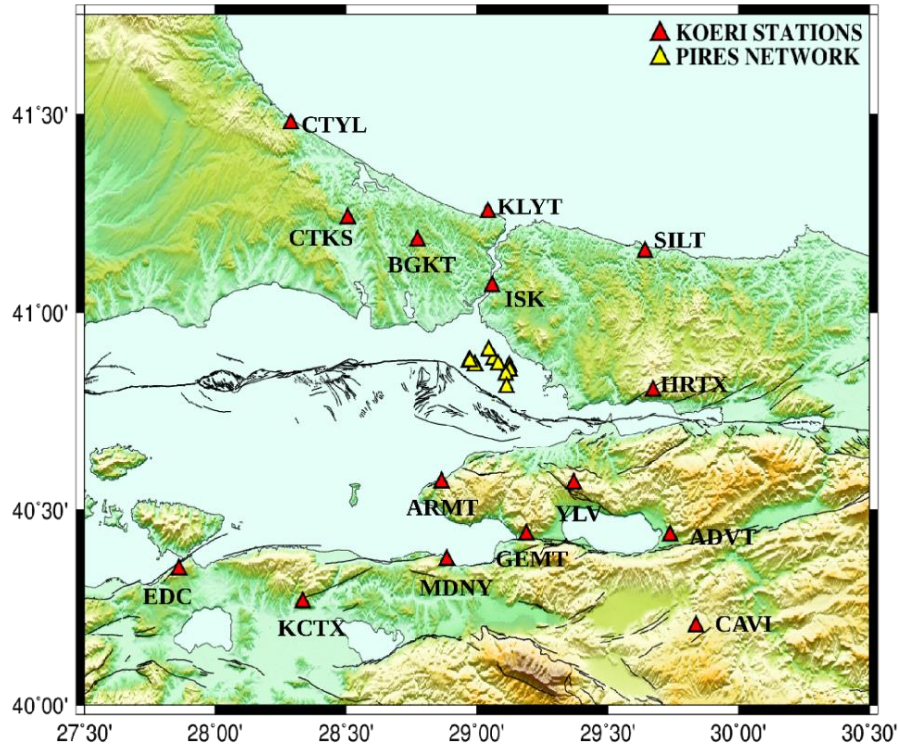

Figure 4.1. PIRES Network and Seismic Stations used in the study area.

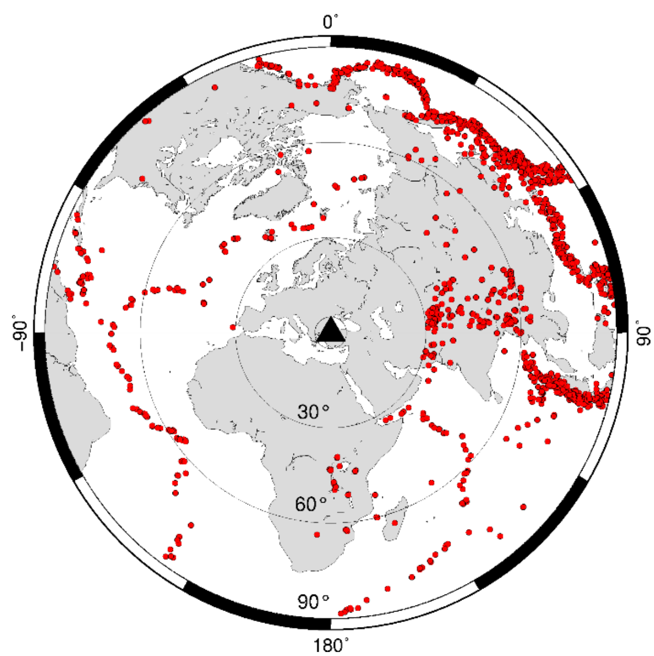

Figure 4.2. Teleseismic earthquakes used in the study.

After selecting the available data, basic preparation steps were applied to the data. Firstly, P arrival times of earthquakes were picked by hand and the data were cut with windowing from 60 seconds before P arrivals to 90 seconds after the predicted P arrival time. Basic filtering is applied to all waveforms by removing mean and trend, then band-pass filtering between 0.1-2 Hz using 4^{th} order Butterworth filter with two passes. Tapering is also applied. To isolate converted S phases from the P wave, XYZ components are transformed into RTZ coordinate system by using back-azimuth. Furthermore, in order to calculate the receiver functions in time domain iterative deconvolution technique suggested by Ligorria and Ammon (1999) is applied by using 200 iterations and a Gaussian width factor of 2.5 (corresponding to 1 Hz pulse width). This total procedure takes about one day of computational time on a standard PC computer, for one single station. The quality of the iterative deconvolution can be evaluated using the misfit between predicted and actual radial receiver functions. In this work a lower limit of 70% is set to eliminate the unreliable receiver functions. The selected receiver functions are also subjected to a visual inspection for a second step elimination.

Moreover, receiver functions were stacked in order to achieve better signal to noise ratio and binned azimuthally to show variation with respect to the backazimuth. The whole procedure is summarized in Figure 4.3 in the form of a flow chart.

The histogram of teleseismic events available for each azimuth is given in Figure 4.4. As commonly observed for all receiver functions studies in Turkey, the data coverage is rich for the azimuth range between 0°-120°. The impact of the event magnitude upon of the receiver function quality is shown on the right hand side of the same figure. One can clearly see from the chart that only very few events with high magnitude results in a low misfit. In other words, large magnitude events guarantee best receiver functions regardless of the distance or the depth of the events, as generally mentioned.

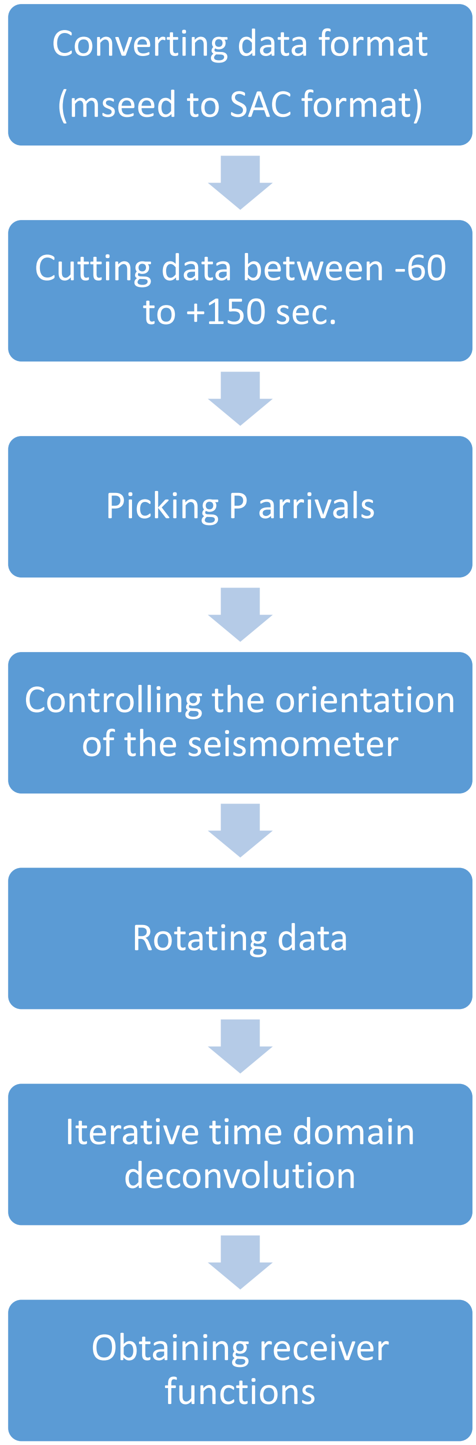

Figure 4.3. Basic steps in data analysis.

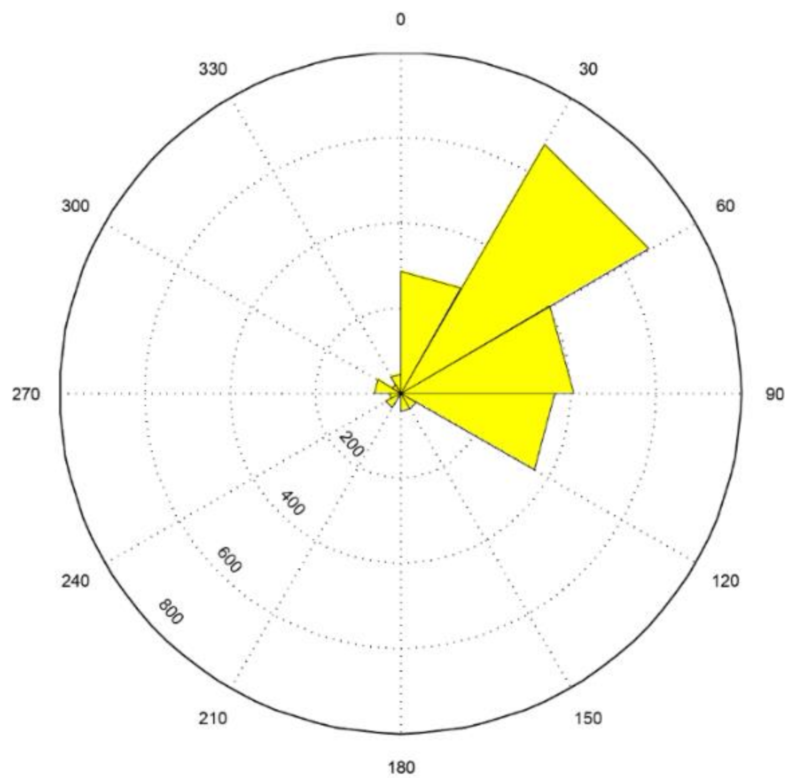

Figure 4.4. The azimuthal distribution of events used in the study.

At this stage it is clear some stations have a better data coverage than others. This is due to the fact that some stations were operated for a shorter time periods or any other non-technical issue such as the non-availability of the data, etc. The number of selected events at each station thus represents in a way, the reliability of that station, and this is given in Figure 4.5. Note that the three stations with the lowest number of events (BUYA, BRGZ and MRTI) are excluded from the analysis.

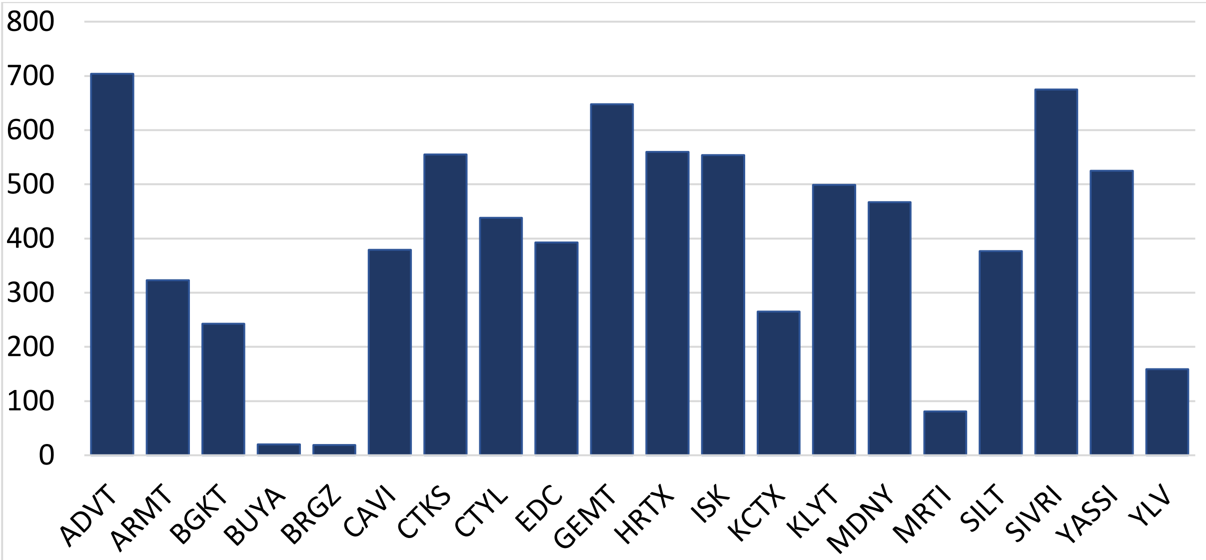

Figure 4.5. The number of RFs for each station used in the study.

The selection criteria for RF is an important procedure after deconvolution process. Fit value of receiver function and magnitude relation for ADVT station given in Figure 4.6. The number of events decreases with the magnitude and fit values of RF.

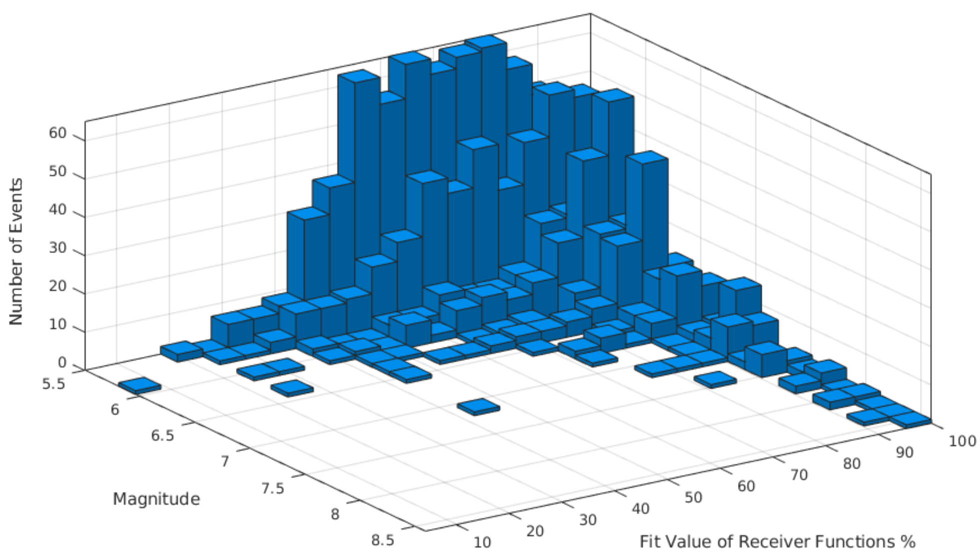

Figure 4.6. Magnitude versus fit value of radial RF’s in ADVT station.

The distance of the events is not expected to have a critical influence upon the shape of the receiver function. This is shown by the example of CTYL station given in Figure 4.7, where radial receivers are plotted for varying distances of teleseismic events. The distance to events is shown in terms incidence angle of the wave, which is given by the ray parameter. The ray parameter varies between 0.041 to 0.079 s/km, which corresponds to distances of 90°- 30°, respectively. Apparently, there is no variation of the receiver function for all event distances.

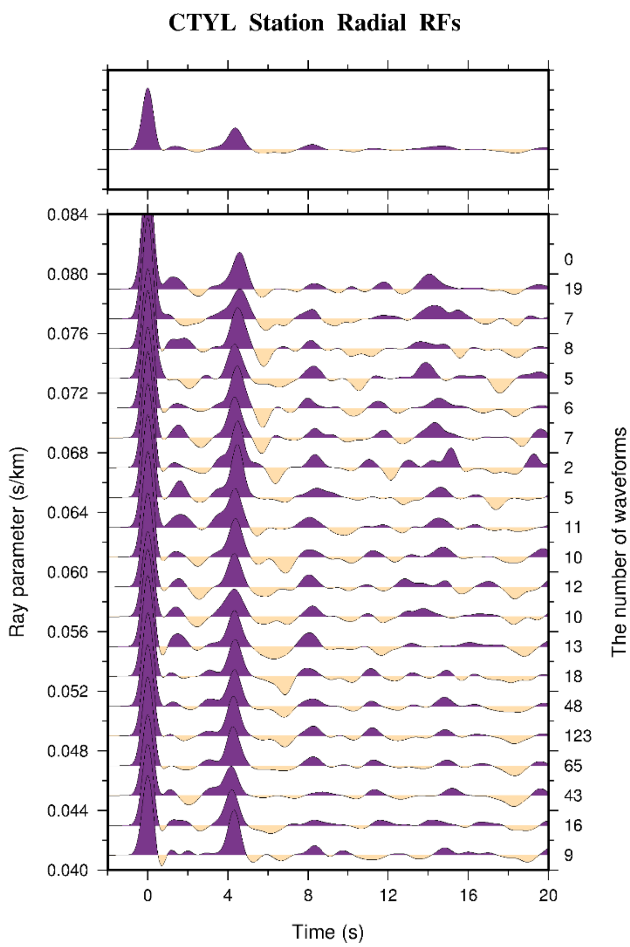

Figure 4.7. Radial receiver functions with respect to the ray parameter in CTYL station. The number on the right of each trace demonstrates how many particular receiver functions contributed to the trace in the ray parameter of 0.04 s/km bins.

An important assumption in the calculation of receiver functions is that, the structure beneath the station can be expressed in terms of homogeneous horizontal layers. Therefore, the energy on tangential component of the receiver functions is zero (or in practice, contains incoherent noise) and the energy on the radial component is expected to be dominant. Furthermore, since no azimuth variation is assumed receiver function as are expected to be the same for all directions. However, this is very seldom seen in real data. In practice, backazimuth independent arrivals are used to image subsurface interfaces. It can be tested the azimuthal variation in the Moho Ps converted phase in the radial component, and the amplitude of arrivals in the transverse receiver function, which should be zero for flat-lying, isotropic layers. It is noticed that the obtained receiver functions in our study show an azimuthal dependence, which changes from one station to other. The degree of energy leakage to tangential component also changes according to the locations of the station. This suggests the complexity of the structures. In particular, it is observed that for stations close to the NAF, the tangential motions are comparable to radial motions implying significant deviation from the horizontal homogeneous layer assumption, possibly due to the presence of the fault. Below two examples of these end members are given, the first one satisfying the horizontal layer assumption and the second one contradicting the same assumption.

Figure 4.8 shows the receiver functions for CAVI station, over the total range of back azimuths (0°- 360°). The small variation in the Ps converted phase (4 s ± 0.2) in the radial receiver function and the small amplitude of the tangential receiver function relative to the amplitude of the radial justify modeling the crust and upper mantle structure of this station as 1D structure. The small deviation of the order of 0.2 second can be ignored since background noise or event distance variation can easily introduce such small scale disturbances. In this study, these type of stations where azimuthal variation are limited to a minimum and therefore the horizontal layer assumption is best satisfied, are called “Stable Stations”.

Figure 4.9 shows the receiver functions for the HRTX station, again over the total range of back azimuths. It is first noticed that the Moho shows large amplitude positive arrivals with strong variation in arrival time, varying between 4 and 6 sec. A second pulse located at 2.2 s ± 0.1, between the direct and the Moho pulses, hints a mid-crustal boundary. This mid-crust pulse however disappears at some specific azimuth (60°- 240°), which in turn points to a non-horizontal structure. Furthermore, the high amplitude of the tangential receiver functions relative to the amplitude of the radial receiver functions indicate a breakdown of P–SH to SV decoupling. This is likely to be caused by complex structural effects such as scattering, dipping of interfaces, anisotropy, and the presence of 2D or 3D heterogeneity. In this study, these type of stations where azimuthal variation hints a deviation from simple 1-D model, are called “Unstable Stations”.

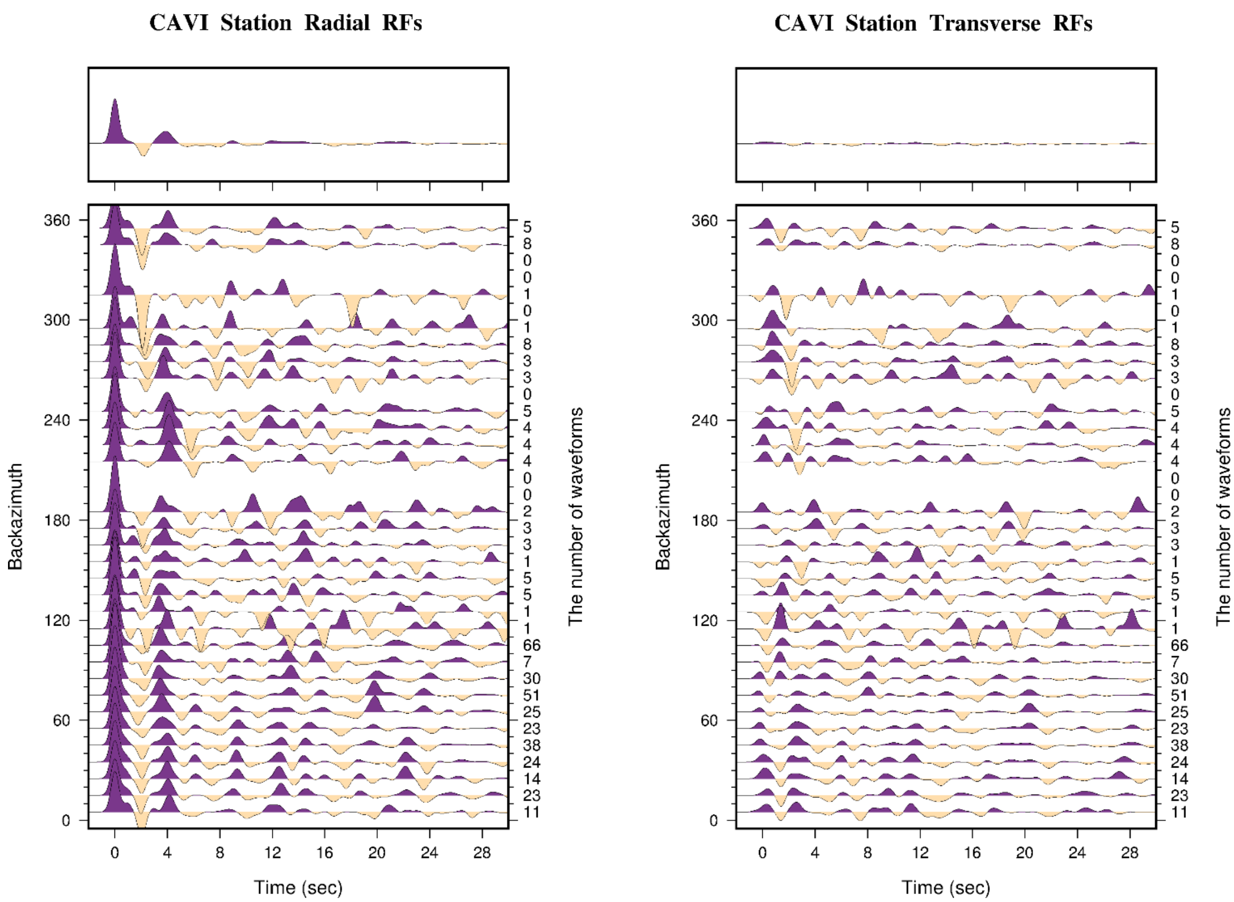

Figure 4.8. Radial RFs in (left), and tangential RFs (right) in CAVI station which is illustrated as the “stable station” in the study region due to the small variation of arrival times on the radial component and low energy on the tangential component. The number on the right of each trace demonstrates how many particular receiver functions contributed to the trace in the azimuth of 10° bins.

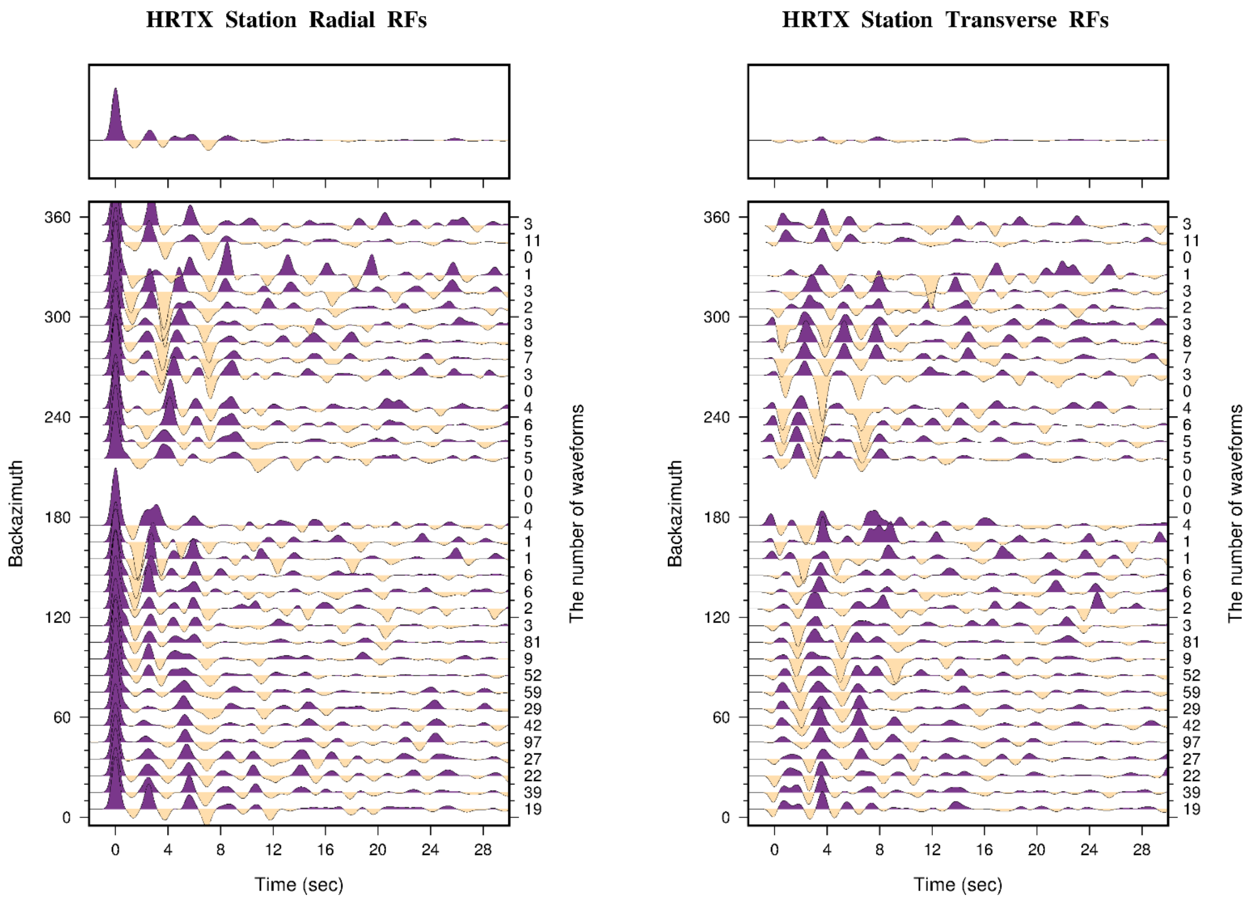

Figure 4.9. Radial RFs in (left), and tangential RFs (right) in HRTX station which is illustrated as the "unstable station" in the study region due to the large variation of arrival times on the radial component and high energy on the tangential component. The number on the right of each trace demonstrates how many particular receiver functions contributed to the trace in the azimuth of 10° bins.

The stations that clearly show characteristics of an unstable station are: ADVT, HRTX, YLV, and all of the stations at PIRES array. Additionally, two other stations, namely GEMT and MDNY, also show a much less degree of "unstable" characteristics and therefore stand at nearly half way between the two types. In fact, these last two stations were in included in the 1D inversion process of as shown in Section 4.5, and a satisfactory horizontal model were obtained for these two cases.

At this stage it is important to note that the stations that are seen to be “unstable” are the ones that are located close to the NAF, with the exception of YLV. This result has important implications, which means that the crustal structure of the Marmara Region is quite stable except at locations, which are disrupted by the activity of NAF. This disrupted area is limited to the very close vicinity of the fault. On the other hand, the stations on the fault show crustal complexities that are not easy to solve. In fact, only two of the stations were analyzed by 3D modeling, while all of the stations on the PIRES array show no sign of regularity that can be translated into a reliable structural model. Consequently, one may consider that the Çınarcık Basin zone is structurally most complex zone of the total Eastern Marmara. Note that the case of the two stations GEMT and MDNY, which shows a limited degree of “Unstability” may imply that this southern branch of the NAF, which crosses Iznik-Mekece-Gemlik Bay, may represent a younger branch of the NAF. In other word, the fault activity did not have enough time to disturb the crustal structure as compared to the case of PIRES and HRTX. These two stations which show an intermediate characteristic between stable and unstable ones will be called as “quasi-stable” stations. The location of the three types, namely stable, unstable, and quasi-stable stations are shown in Figure 4.10 with using white, black, and gray triangles, respectively. The active faults in the region are also shown in black lines in the same figure taken by MTA. One can clearly see that stations which shows sign of unstabilities are the ones located on the fault lines.

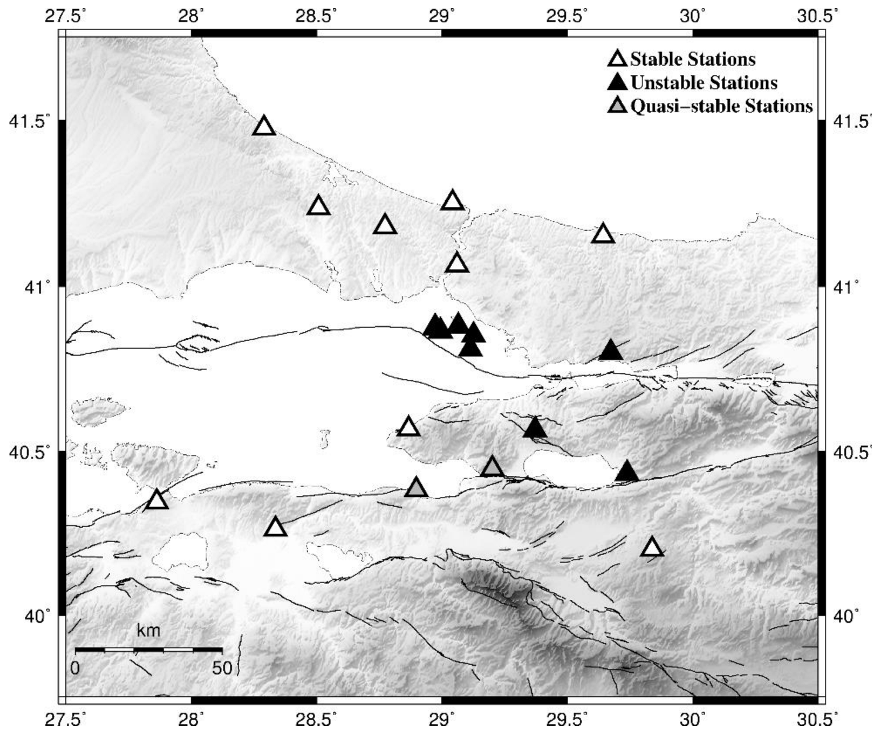

Figure 4.10. Stable, Quasi-stable and Unstable stations in the study area. Fault lines are taken from MTA.

4.2. The Data Quality Assessment

The assessment of data quality for seismic station and seismic network are important procedures, which should be applied prior data acquisition and interpretation. Recently, three-component seismic recordings are widely used in seismic studies for constraining earthquake sources and structural complexities such as shear-wave splitting, focal mechanism, receiver function, polarization analysis of both body and surface wave on Earth. Accurate aligning of the seismic sensor orientation to the true north is one of the most critical parameter for seismic data acquisition procedures studies rely heavily on precise three-component broadband data. However, this parameter is simply affected by magnetic field around the station such as volcanic areas and earth poles regions or by human error in declination calibration during an installation even for a professional field seismologist and this misorientation lead to wrong results and interpretation in the data analysis procedures. It is therefore very important to estimate instrument orientation and determining misoriented stations for operating a modern seismic network and improving the quality of the network in the future.

It is predicted that errors in the orientation of the north-south and east-west components from the polarization of body waves (Yoshizawa *et al*., 1999; Schulte-Pelkum *et al*., 2001) and surface waves (Laske 1995; Laske & Masters 1996; Larson 2000; Larson & Ekstrom 2002; Stachnik *et al*., 2012; Zha *et al*., 2013) by several scientists. The sensor orientation is not aligned properly by more than 10° even in quality stations in Global Seismographic Network GSN in some cases (e.g. Larson & Ekstrom 2002).

In this study, P-waves principal component analysis is used to figure out the directions of particle motions by using well-recorded earthquakes with high S/N ratio with magnitude greater than 5.5 occurring in the epicentral distance 30°-90° during the period 2006-2017 at the 15 stations operated by KOERI shown in Figure 4.1 and listed in Table 4.1. The number of selected events for P-waves principal component analysis for each station demonstrated in Figure 4.11.

Sensor type of the stations used in the study are GURALP 3ESP, 3T, and 3ESPC given in Table 4.1. Teleseismic events were separated as their backazimuth as Group 1 (BAZ 42-48) and Group 2 (BAZ 102-105). Moreover, Tohoku Earthquake (2011-03-11T05:46:23 Mw=8.9) was included in the study. A two-pole Butterworth low-pass filter of 0.3 Hz is applied to all waveforms which are composed of 8 second P-wave onset time. The apparent back azimuth was computed by calculating the covariance matrix from particle motions of BHE and BHN components in MATLAB. Furthermore, polarity reversals for transverse components is also analyzed.

Table 4.1. KOERI Broadband stations, their sensor types and operating time used in the P-waves principal component analysis.

No	Station Name	Sensor Type	Start Time
1	ADVT	Guralp - 3ESP	2006-05-19
2	ARMT	Guralp - 3ESP	2007-12-17
3	BGKT	Guralp - 3ESP	2007-05-29
4	CAVI	(Guralp - 3ESP),(3T)	(27-09-2007 - 2012-06-01), (2012-06-01 -)
5	CTKS	Guralp - 3ESP	2007-09-28
6	CTYL	Guralp - 3T	2007-09-29
7	EDC	Guralp - 3T	2008-11-27
8	GEMT	Guralp - 3T	2006-07-07
9	HRTX	Guralp - 3ESP	2008-04.03
10	ISK	Guralp - 3T	2007-01-25
11	KCTX	Guralp - 3ESP	2008-07-11
12	KLYT	Guralp - 3T	2006-05-18
13	MDNY	Guralp - 3ESP	2008-07-09
14	SILT	Guralp - 3ESP	2007-08-01
15	YLV	Guralp - 3ESPC	2012-01-06

In this study, the apparent back azimuths of the teleseismic events from P-wave particle motions of BHE and BHN components were calculated and plotted as their backazimuth. The results of particle motion of the ADVT station for 38 earthquakes having BAZ 45-50 listed in Table 4.2 called Group 1 and 51 earthquakes having BAZ 101-106 listed in Table 4.3 called Group 2. The deviation from the true north of ADVT station is approximately 37.78°N as shown in Figure 4.12. The results of particle motions for the other stations are given in the following order. Black lines show the apparent backazimuth and red lines show the true backazimuth, respectively.

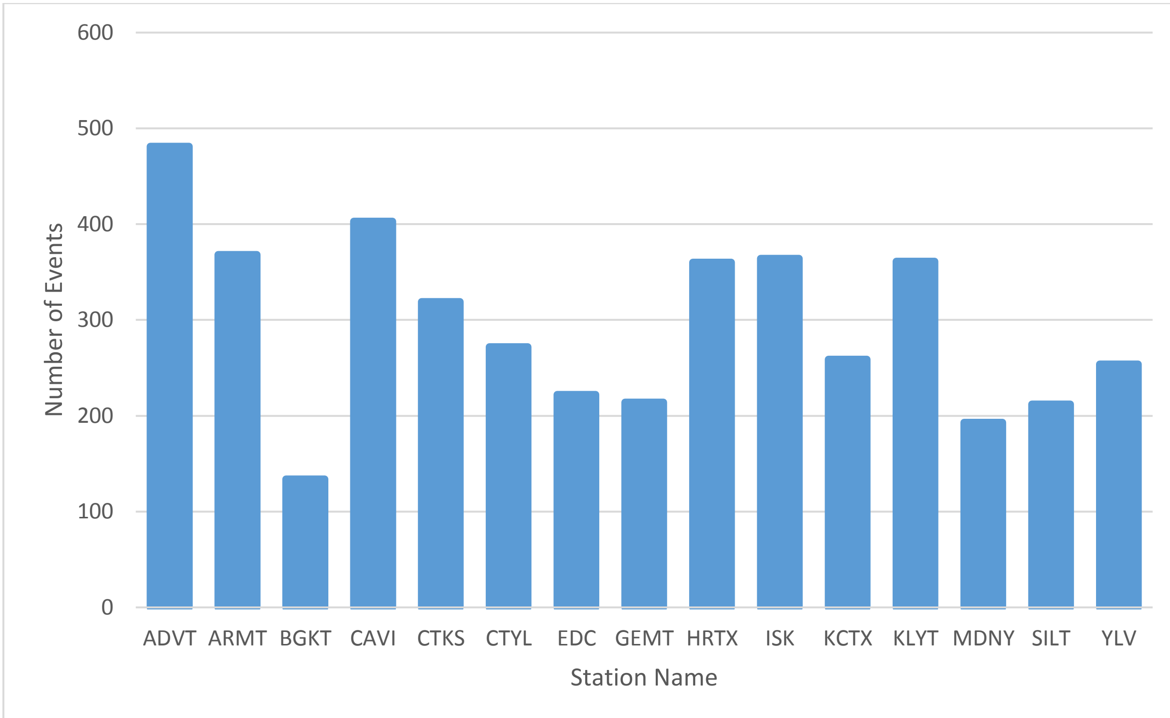

Figure 4.11. The number of selected events with high S/N ratio for P-waves principal component analysis for each station.

A field trip was also organized to the CTKS station located in Çatalca to control the orientiation of the seismometer as shown in Figure 4.11. The misorientation is around 36º which is similar to our results and the station was corrected to the true north direction on 17 January 2019.

Figure 4.12. The field trip to the CTKS station located in Çatalca (left) and the correction of misoriented seismometer to the true north direction (right).

Table 4.2. Group 1 events BAZ (45-50) used for calculating P-wave particle motion in ADVT station.

Event ID	Mw	BAZ(45-50)
2006-09-16T02:22:50	5,8	48,73
2008-05-07T16:02:04	6,4	49,54
2010-03-14T08:08:04	6,7	48,27
2011-03-12T01:47:19	6,6	47,72
2011-03-13T01:26:06	6,2	49,78
2011-03-15T15:23:54	6,0	45,57
2011-03-17T12:54:54	5,6	49,20
2011-03-17T18:55:35	5,5	48,20
2011-03-19T01:22:48	5,9	46,16
2011-03-22T07:18:46	6,4	47,26
2011-03-25T11:36:25	6,2	47,34
2011-03-27T22:23:59	6,1	47,53
2011-03-30T05:29:52	6,0	48,95
2011-03-31T07:15:30	6,0	47,26
2011-04-11T08:16:13	6,7	49,46
2011-04-13T19:57:26	6,0	45,96
2011-05-07T20:52:23	5,6	46,08
2011-06-22T21:50:52	6,6	46,29
2011-07-23T04:34:24	6,3	47,25
2011-07-30T18:53:53	6,3	49,16
2011-08-19T05:36:33	6,2	48,30
2011-09-16T19:26:42	6,6	45,84
2011-09-16T22:40:46	5,6	45,57
2011-11-23T19:24:33	6,1	48,66
2012-05-20T07:19:58	6,2	46,13
2012-06-17T20:32:22	6,3	47,28
2012-10-01T22:21:46	6,0	45,94
2013-10-25T17:10:17	7,1	46,97
2014-07-04T22:42:06	5,9	46,63
2014-07-11T19:22:00	6,5	48,30
2014-10-11T02:35:47	6,0	45,04
2015-05-12T21:13:01	6,8	47,24
2016-01-02T04:22:18	5,8	48,63
2016-11-21T20:59:49	6,9	48,70
2017-07-20T00:11:25	5,8	48,61
2017-09-20T16:37:16	6,1	46,41
2017-10-06T07:59:32	6,2	47,10
2017-10-06T14:56:42	5,6	49,01

Table 4.3. Group 2 events BAZ (101-106) used for calculating P- wave particle motion in ADVT station.

Event ID	Mw	BAZ(101-106)
2006-07-19T10:57:33	6,0	104,69
2006-07-27T11:16:41	5,7	103,77
2006-08-11T20:54:14	5,7	103,79
2006-09-16T06:17:43	5,7	102,95
2006-12-01T03:58:21	6,4	101,04
2006-12-17T21:10:20	5,9	102,81
2007-03-06T03:49:40	6,2	103,08
2007-03-06T05:49:26	6,3	103,08
2007-04-27T08:02:47	6,0	102,70
2007-06-26T22:23:05	5,9	105,45
2007-08-08T17:04:58	7,6	102,37
2007-09-12T11:10:25	8,0	105,55
2007-09-12T23:49:05	8,0	104,61
2007-09-13T03:35:28	7,2	104,99
2007-09-13T16:09:18	6,5	104,58
2007-09-14T06:01:37	6,6	105,25
2007-09-26T15:43:05	6,3	104,76
2007-09-29T05:32:44	5,9	103,97
2007-10-02T03:43:41	6,2	105,32
2007-10-24T21:02:50	6,9	105,45
2007-11-22T23:02:13	6,2	102,83
2008-02-20T08:08:32	7,2	103,77
2008-02-25T08:36:34	7,4	105,02
2008-02-25T18:06:01	6,5	105,01
2008-02-25T21:02:18	6,9	105,01
2008-04-02T08:48:50	6,0	104,73
2010-03-05T16:06:58	6,5	105,48
2010-04-06T22:15:03	7,6	103,24
2010-06-12T19:26:47	7,5	102,67
2010-06-26T09:50:45	6,0	103,70
2010-10-25T14:42:21	7,8	105,53
2010-10-25T19:37:30	6,1	105,04
2010-11-19T21:55:15	5,7	102,20
2011-01-17T19:20:57	6,2	105,22
2011-01-18T20:23:25	7,4	101,86
2011-04-03T20:06:42	6,7	105,20
2011-08-22T20:12:22	6,0	105,18
2011-09-05T17:55:11	6,7	102,23
2012-06-23T04:34:52	6,1	102,23
2012-07-25T00:27:44	6,3	103,76
2012-11-01T14:12:02	5,6	103,15
2013-06-13T16:47:25	6,7	105,58
2013-09-24T11:29:47	7,7	103,35
2014-01-25T05:14:21	6,1	102,96
2014-05-18T01:02:29	6,0	104,91
2016-04-06T14:45:33	6,0	104,10
2016-05-02T04:21:25	5,7	103,85
2016-12-06T22:03:33	6,5	101,64
2017-08-13T03:08:13	6,4	104,61
2017-08-31T17:06:56	6,3	104,10
2017-12-15T16:47:59	6,5	103,35

STATION: ADVT

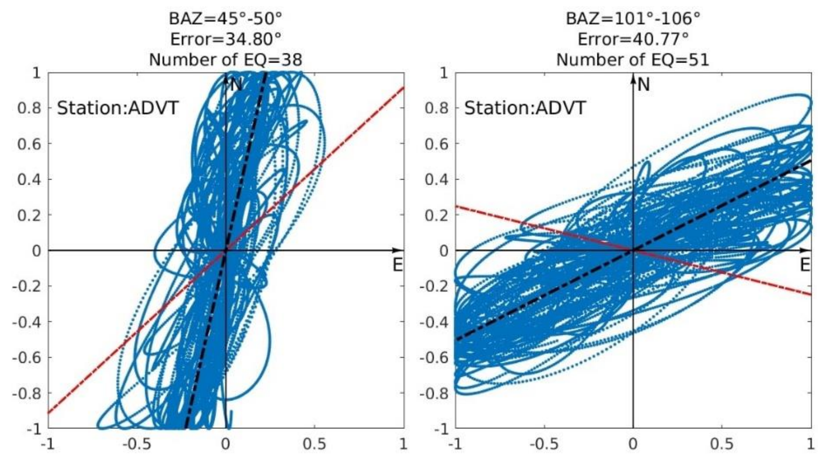

Figure 4.13. The results of particle motion of the ADVT station for 38 earthquakes having BAZ 45-50 called Group 1 (left) and 51 earthquakes having BAZ 101-106 called Group 2 (right).

STATION: ARMT

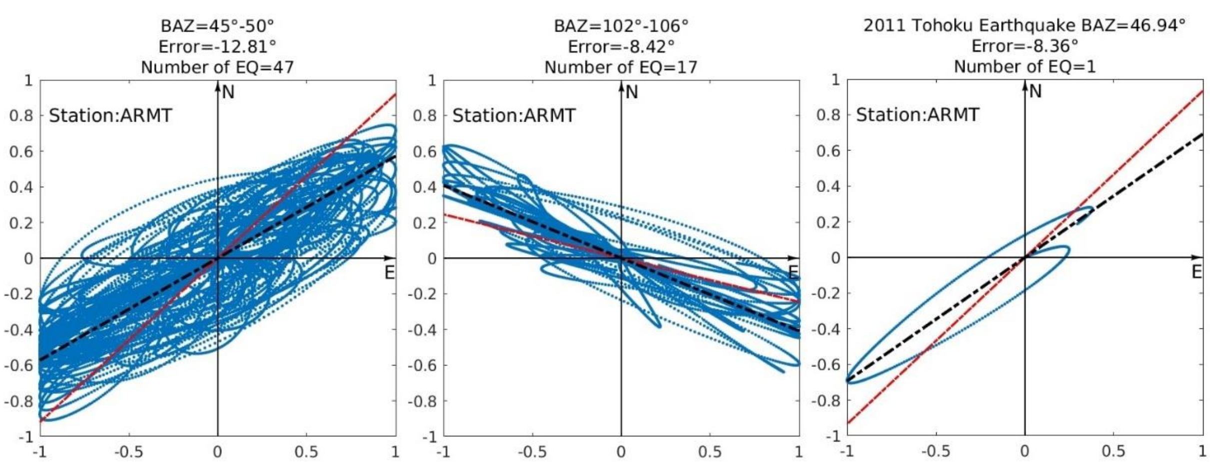

Figure 4.14. The results of particle motion of the ARMT station for BAZ 45-50 called Group 1 (left), BAZ 101-106 called Group 2 (middle), and 2011-03-11 Mw=8.9 Tohoku Earthquake (right).

STATION: BGKT (Before 30.11.2016)

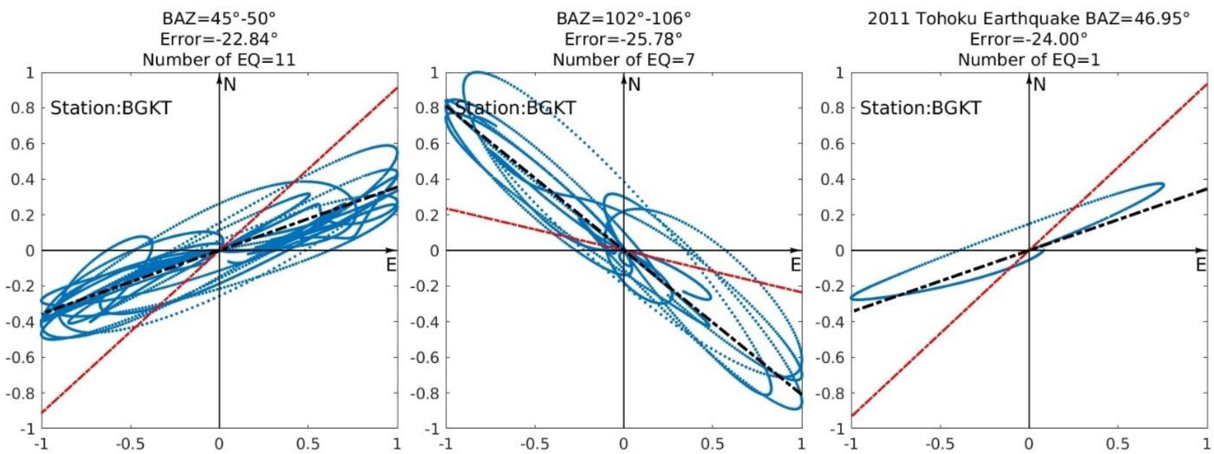

Figure 4.15. The results of particle motion of the BGKT station for BAZ 45-50 called Group 1 (left), BAZ 101-106 called Group 2 (middle), and 2011-03-11 Mw=8.9 Tohoku Earthquake (right) before 30.11.2016.

STATION: BGKT (After 30.11.2016)

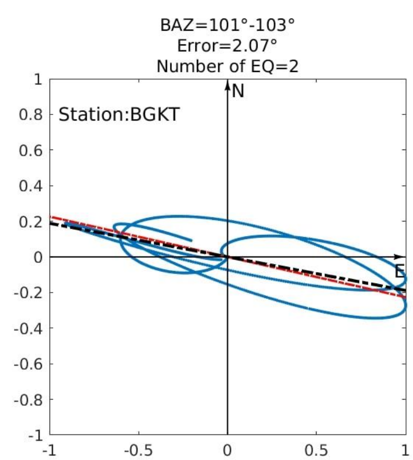

Figure 4.16. The results of particle motion of the BGKT station for BAZ 101-103 called Group 2 after 30.11.2016.

STATION: CAVI

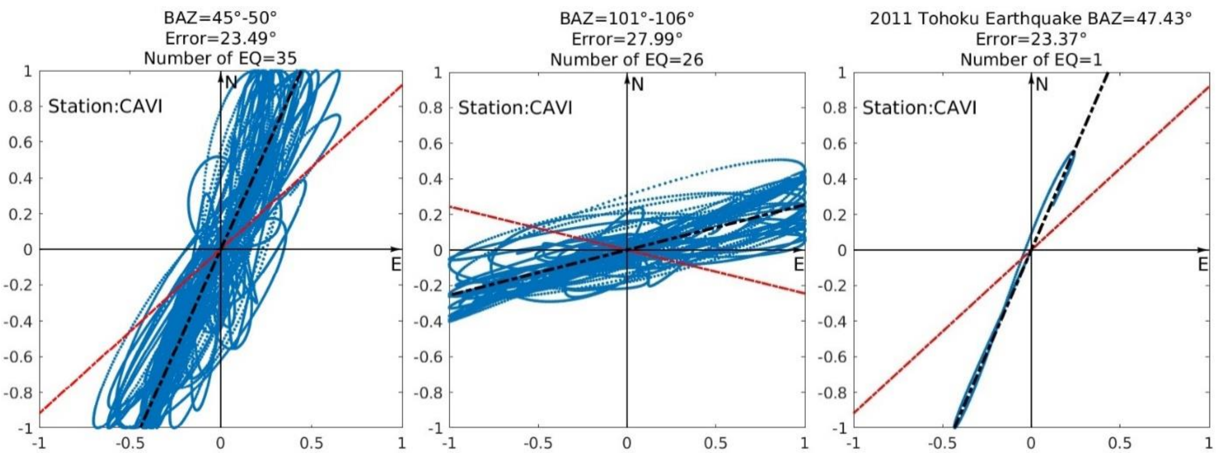

Figure 4.17. The results of particle motion of the CAVI station for BAZ 45-50 called Group 1 (left), BAZ 101-106 called Group 2 (middle), and 2011-03-11 Mw=8.9 Tohoku Earthquake (right).

STATION: CTKS

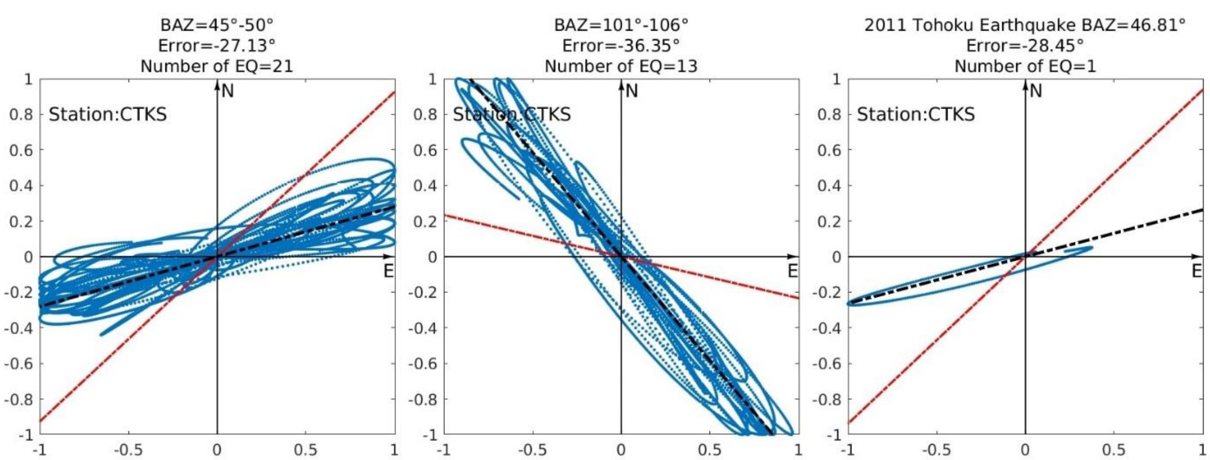

Figure 4.18. The results of particle motion of the CTKS station for BAZ 45-50 called Group 1 (left), BAZ 101-106 called Group 2 (middle), and 2011-03-11 Mw=8.9 Tohoku Earthquake (right).

STATION: CTYL (Before 2011.06.22)

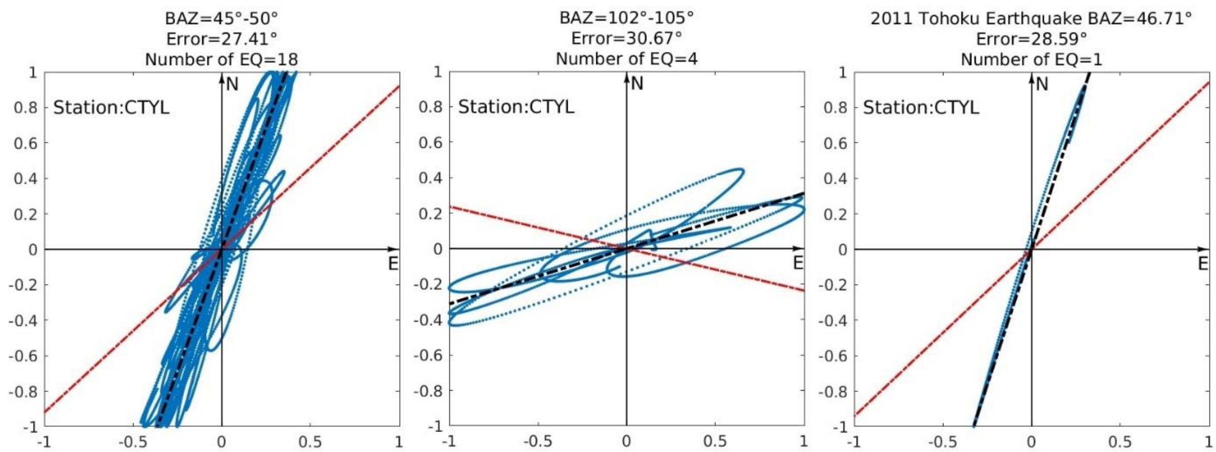

Figure 4.19. The results of particle motion of the CTYL station for BAZ 45-50 called Group 1 (left), BAZ 102-105 called Group 2 (middle), and 2011-03-11 Mw=8.9 Tohoku Earthquake (right) before 2011.06.22.

STATION: CTYL (After 2011.07.23)

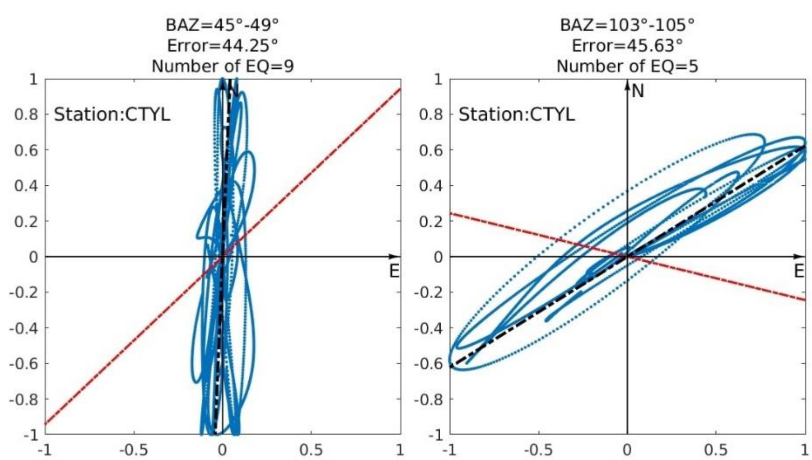

Figure 4.20. The results of particle motion of the CTYL station for BAZ 45-49 called Group 1 (left), BAZ 103-105 called Group 2 (right), after 2011.07.23.

STATION: EDC

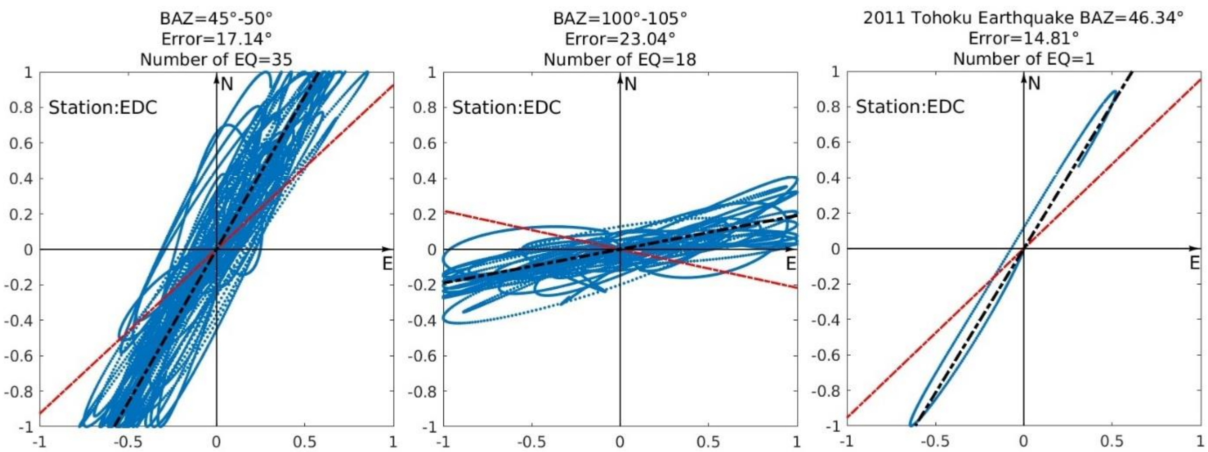

Figure 4.21. The results of particle motion of the EDC station for BAZ 45-50 called Group 1 (left), BAZ 100-105 called Group 2 (middle), and 2011-03-11 Mw=8.9 Tohoku Earthquake (right).

STATION: GEMT

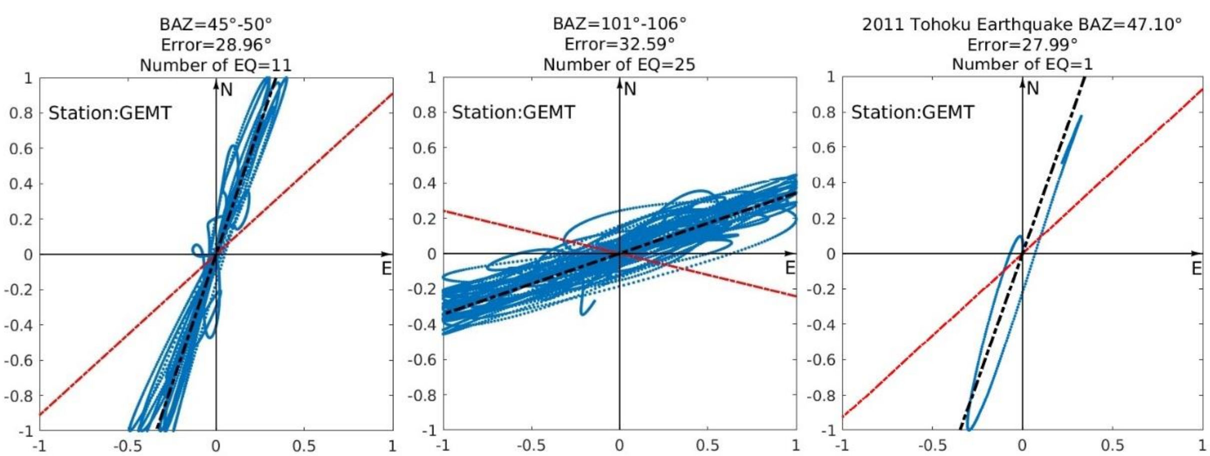

Figure 4.22. The results of particle motion of the GEMT station for BAZ 45-50 called Group 1 (left), BAZ 101-106 called Group 2 (middle), and 2011-03-11 Mw=8.9 Tohoku Earthquake (right).

STATION: HRTX

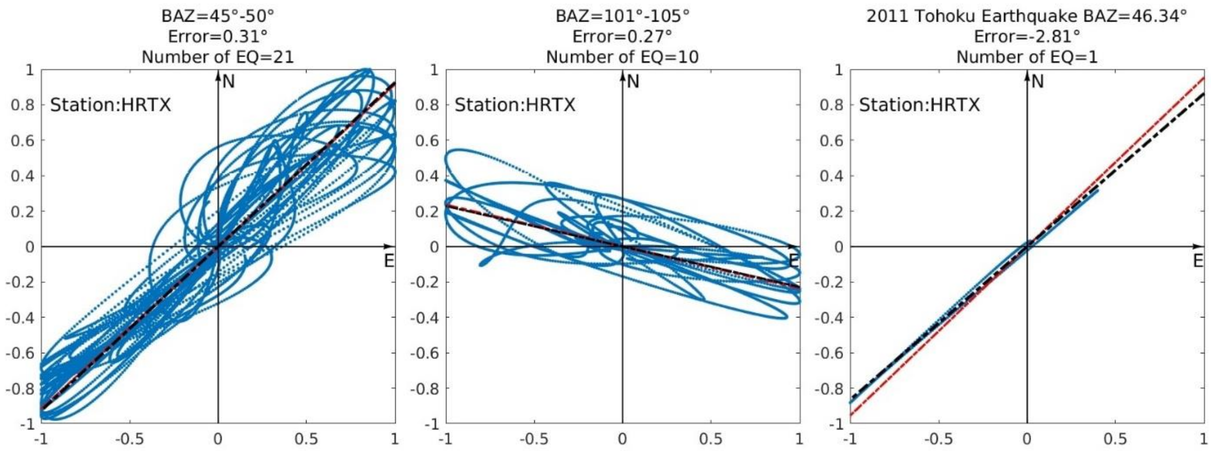

Figure 4.23. The results of particle motion of the HRTX station for BAZ 45-50 called Group 1 (left), BAZ 101-105 called Group 2 (middle), and 2011-03-11 Mw=8.9 Tohoku Earthquake (right).

STATION: ISK

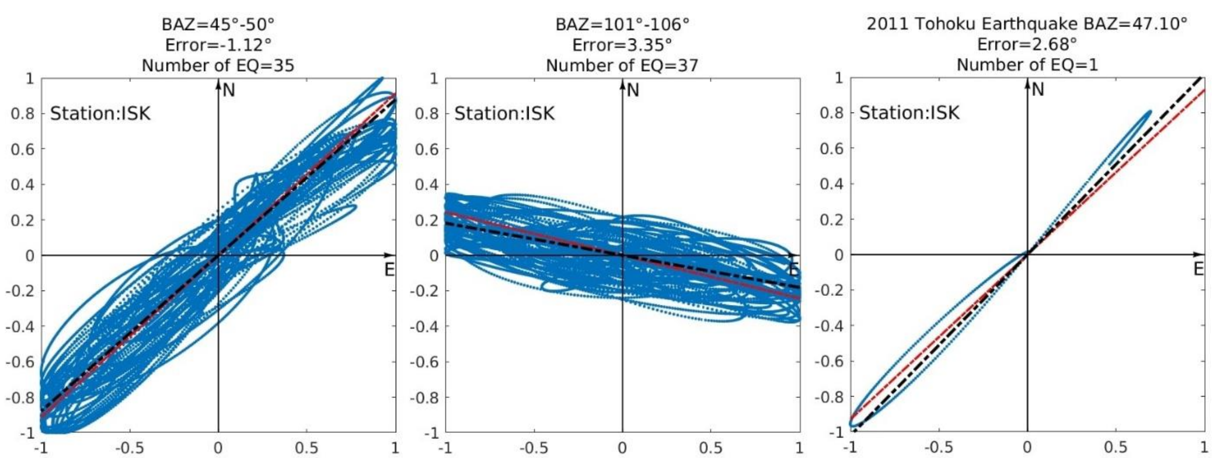

Figure 4.24. The results of particle motion of the ISK station for BAZ 45-50 called Group 1 (left), BAZ 101-106 called Group 2 (middle), and 2011-03-11 Mw=8.9 Tohoku Earthquake (right).

STATION: KCTX

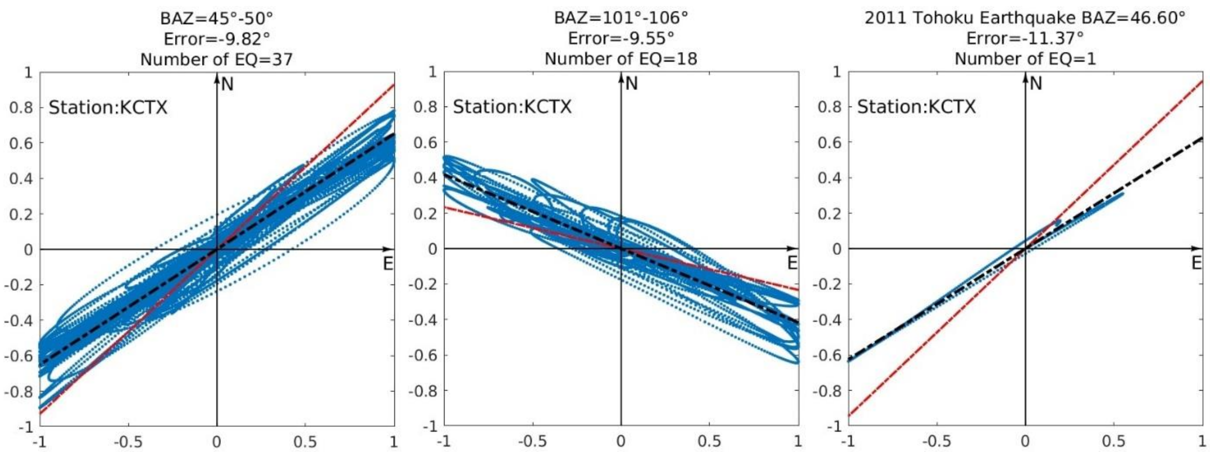

Figure 4.25. The results of particle motion of the KCTX station for BAZ 45-50 called Group 1 (left), BAZ 101-106 called Group 2 (middle), and 2011-03-11 Mw=8.9 Tohoku Earthquake (right).

STATION: KLYT (Before 2009.02.14)

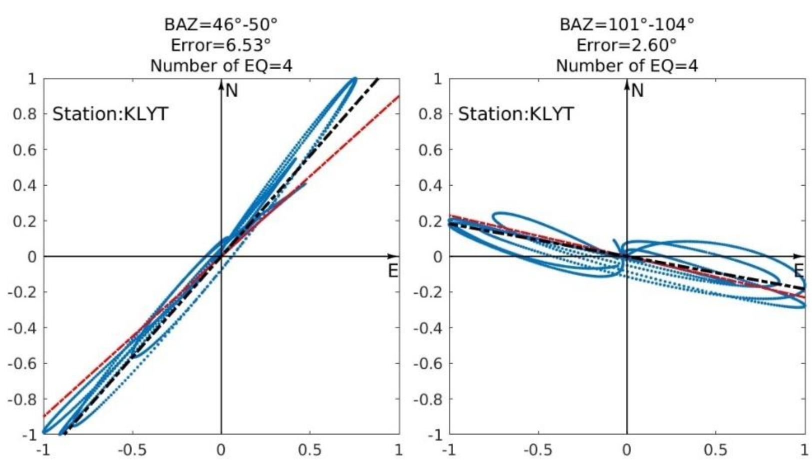

Figure 4.26. The results of particle motion of the KLYT station for BAZ 46-50 called Group 1 (left), BAZ 101-104 called Group 2 (right), and before 2009.02.14.

STATION: KLYT (After 2009-02-14)

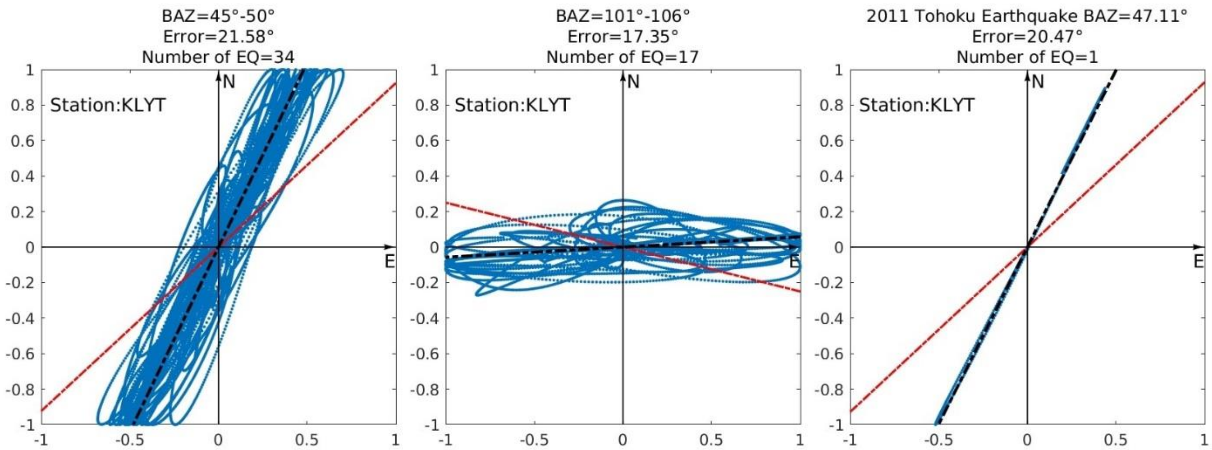

Figure 4.27. The results of particle motion of the KLYT station for BAZ 45-50 called Group 1 (left), BAZ 101-106 called Group 2 (middle), and 2011-03-11 Mw=8.9 Tohoku Earthquake (right) after 2009.02.14.

STATION: MDNY

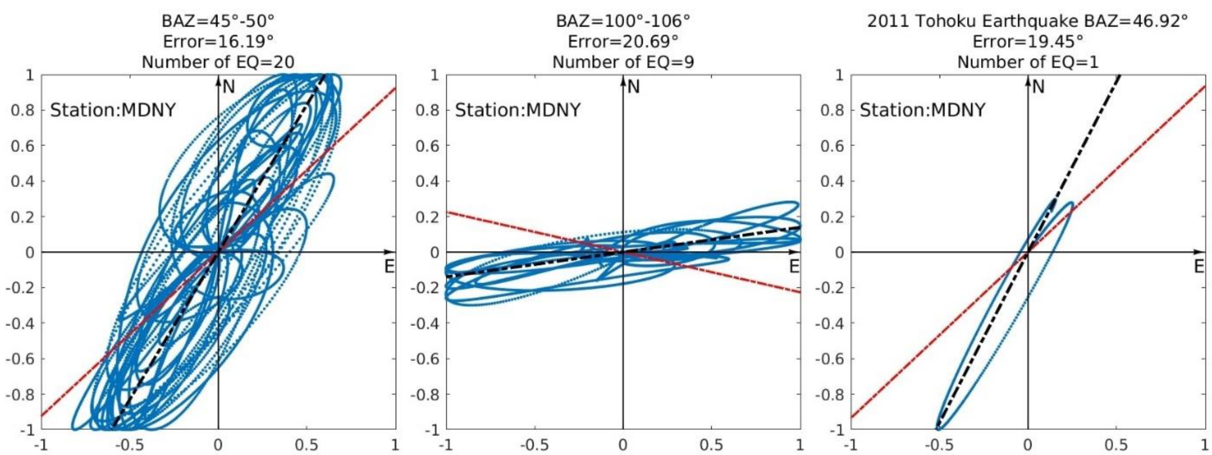

Figure 4.28. The results of particle motion of the MDNY station for BAZ 45-50 called Group 1 (left), BAZ 101-106 called Group 2 (middle), and 2011-03-11 Mw=8.9 Tohoku Earthquake (right).

STATION: SILT

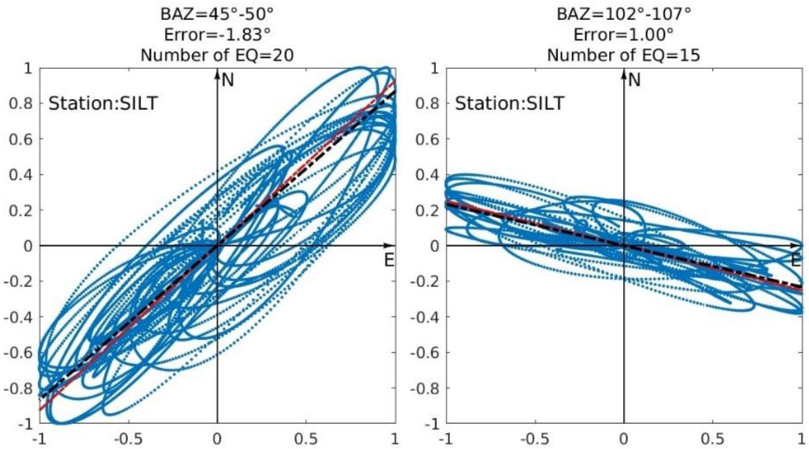

Figure 4.29. The results of particle motion of the SILT station for BAZ 45-50 called Group 1 (left), BAZ 102-107 called Group 2 (middle), and 2011-03-11 Mw=8.9 Tohoku Earthquake (right).

STATION: YLV

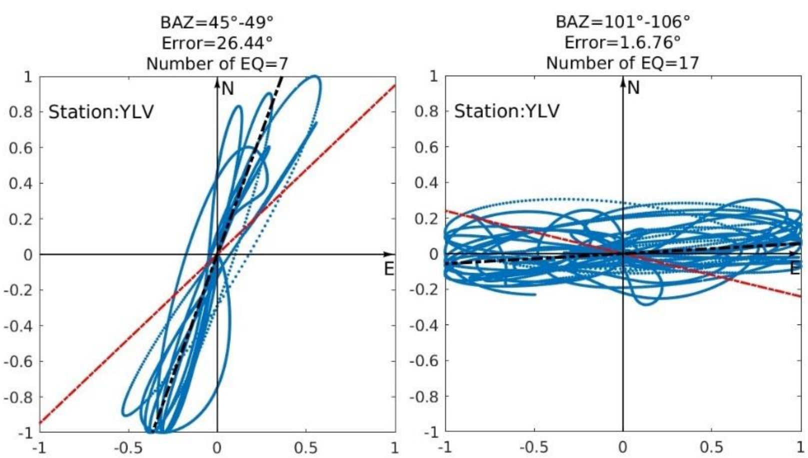

Figure 4.30. The results of particle motion of the YLV station for BAZ 45-49 called Group 1 (left), BAZ 101-106 called Group 2 (right).

In general, no major change is not detected in the orientation of the seismometer during the period of observation except for BGKT, CTYL, and KLYT stations having 2 different results for operating time. The error is nearly the same (0°-6°) for all the azimuths. However, deviation up to 9°-10° degree in CTKS and YLV station are observed. The difference of particle motion likely to be caused by structural effects such as anisotropy, and the presence of 2D or 3D structure. Average angle of deviation for stations of KOERI Network used in the study listed in Table 4.4 and plotted in Figure 4.31.

Table 4.4. Average angle of deviation for stations of KOERI Network used in the study.

No	Station Name	Date	Angle of Deviation
1	ADVT		37.8
2	ARMT		-9.9
3	**BGKT**	Before - 30.11.2016	-24.2
		After - 30.11.2016	2.1
4	CAVI		25.2
5	CTKS		-30.6
6	**CTYL**	Before - 22.06.2011	28.9
		After - 23.07.2011	44.9
7	EDC		18.3
8	GEMT		29.9
9	HRTX		-0.7
10	ISK		1.6
11	KCTX		-10.2
12	**KLYT**	Before - 14.02.2009	4.6
		After - 14.02.2009	19.8
13	MDNY		18.8
14	SILT		-0.4
15	YLV		21.6

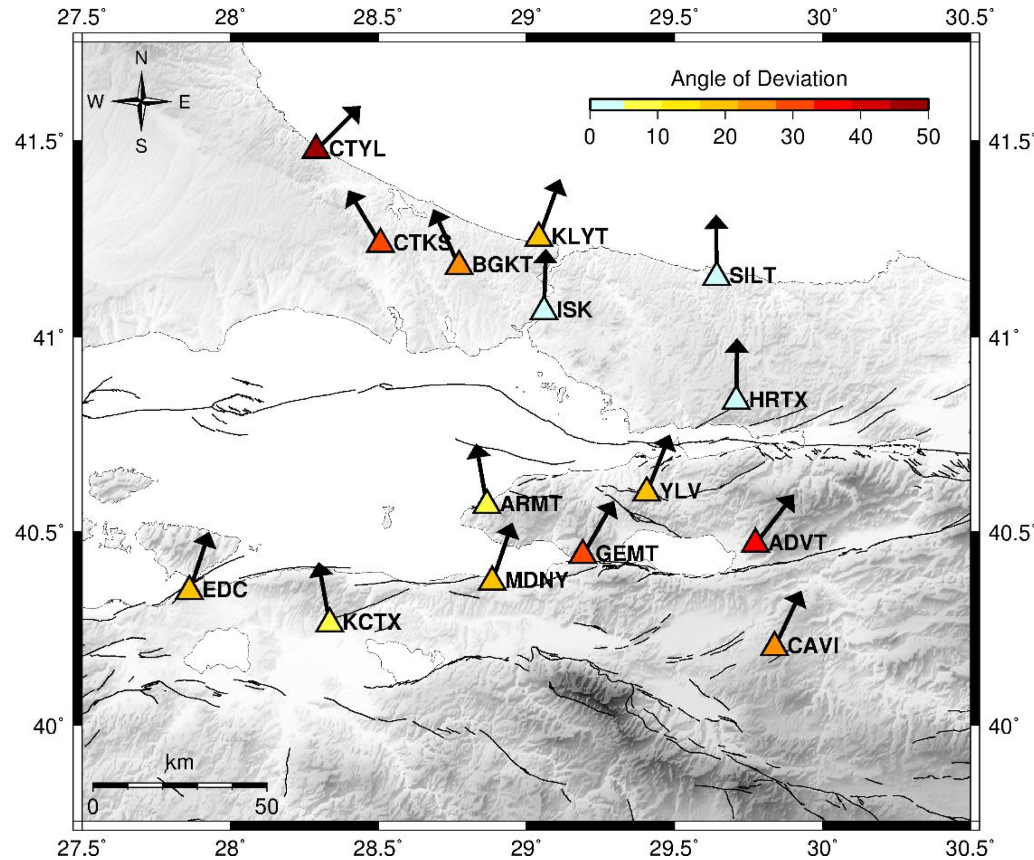

Figure 4.31. Angle of deviation for stations of KOERI Network between 01.01.2012-30.11.2016.

To sum up, the P-wave particle motion was calculated to predict the sensor orientation for a small part of broadband stations operated by KOERI network in the Marmara Region. It is observed that 2/3 stations have misaligned sensor more than 15°. The effect of this misorientation on receiver function can be seen clearly on waveforms, especially on transverse component causing the high amplitude and polarity. If this problem is not considered in the preprocessing step, results of the receiver function modelling might be misinterpreted. It is therefore very important to estimate instrument orientation and determining misoriented stations causing wrong interpretation. Our main goal is to extend this study to all stations operated by KOERI network and improve the quality of the network in the future by providing users of this network a correction rotation reference for their rotation-based seismic analyses

4.3. CCP Stacking Results of All Stations

Receiver function traces which are obtained can vary with the directions according to the location of seismic stations in different tectonic regions. Therefore, to analyze the receiver functions in terms of their BAZ gives us an important aspect for understanding overall pattern from different distances and directions. From this point of view, approximately 8000 radial receiver functions that are obtained for 26 stations were used to calculate the ray tracing as a starting point. For this reason, 5 main 2D profiles of CCP Stacking Method up to 100km depth were plotted representing the ray tracing through the 1D reference Earth model AK135 which is mentioned in the Chapter 3.5 to figure out general trends in 3-D view, at a regional scale.

CCP Stacking of Profile A

Profile A represents the northern part of Marmara Region which is constituted by CTYL, KLYT, CTKS, BGKT and SILT stations. Profile A corresponds to a NNE-SSW transects, which corresponds to the structure along the coastline of the Black Sea as shown in Figure 4.32. This area corresponds the Rodope-Pontide zone, which locally includes the Istranca massif and Istanbul metamorphic basements. Firstly, Moho depth gets thicker towards the eastern direction, as seen in KLYT and SILT (35 km) stations. A gradual thinning is also observed around BGKT station (30 km) towards the south. This transect does not include a major fault structure and the RF profiles look quite stable feature. From the point of deeper structures such as upper mantle, a transition zone between 65 km and 70 km pointing LAB which is not so clear as much as Moho boundary is also revealed in the Profile A.

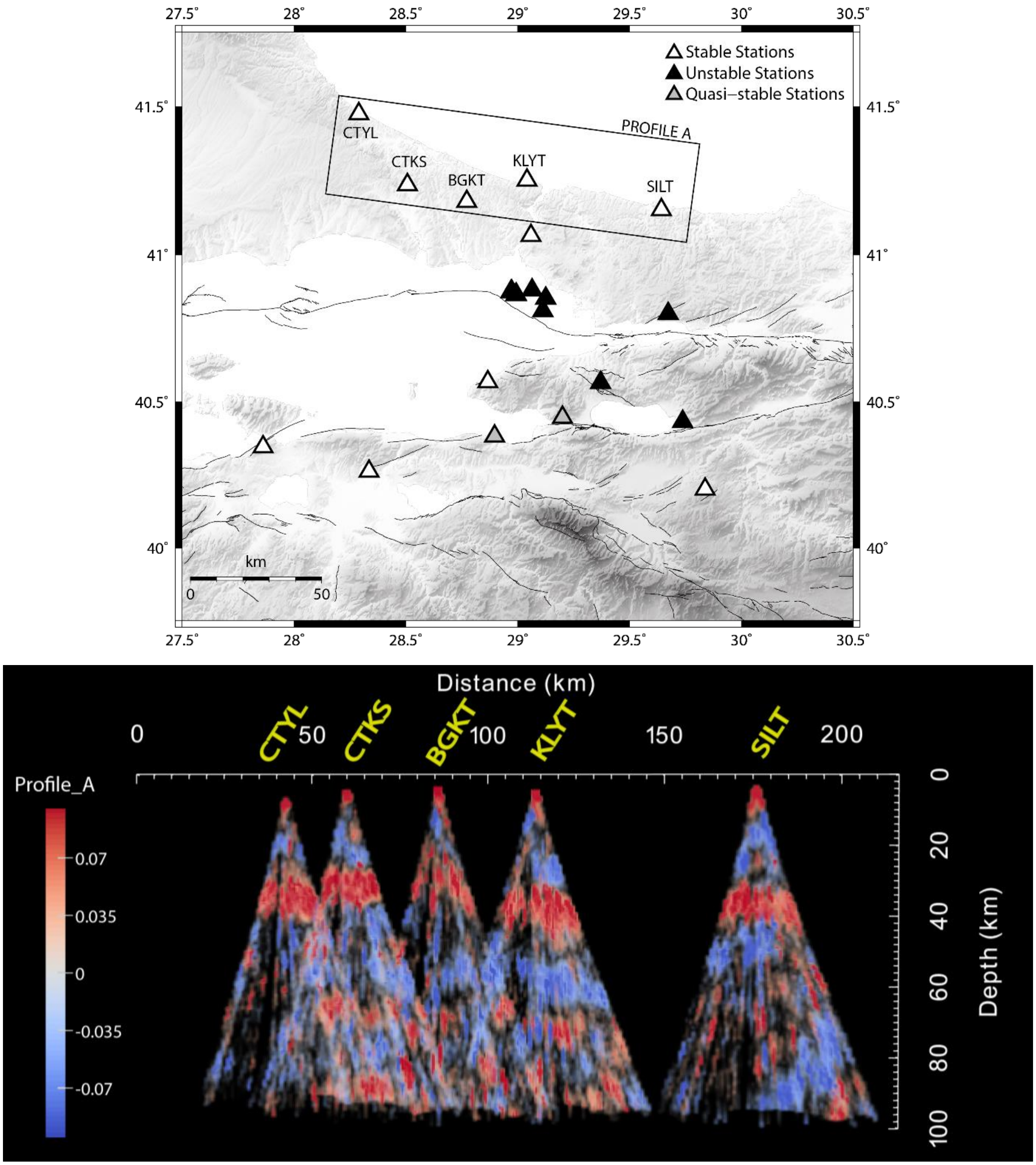

Figure 4.32. The location of Profile A (up) and CCP stacking result of Profile A (down).

CCP Stacking of Profile B

Profile B represents the eastern part of Marmara Region which is constituted by SILT, HRTX, ADVT, and CAVI stations. The stability is not observed for the NS Profile B consisting of Sakarya and Istanbul Zones, where the transect crosses the NAF at two different areas, which corresponds to two different branches of the NAF as shown in Figure 4.33. The stations HRTX and ADVT are located on the crosspoint of the transect with the NAF. Especially for these unstable stations near to the NAF some apparent azimuthal variations exist. In particular, the southern slope (rhs) of the cone of HRTX shows a vertical anomaly (colored as red) which extends from between 12 km and 25 km. This may well correspond to the velocity contrast caused by the northern branch of NAF. One can also see that Moho thickness gets thinner in the south direction and thicker in the north direction of the fault zone for both stations. This is also clearly observed on the azimuthal variation of the pulse arrivals in the radial component of RF waveforms. HRTX station in Profile B shows a pulse at 2 sec which is not as obvious as the Moho arrival implies a strong mid-crust at around 15 km. Finally, the wide negative pulse observed around 7 sec for three stations (HRTX, ADVT, CAVI) corresponds to the LAB located at approximately 65 km depth. It is observed that Moho depth thickens from about 30 km (CAVI station) to 35 km (SILT station) from south to the north direction in the eastern part of Marmara Region.

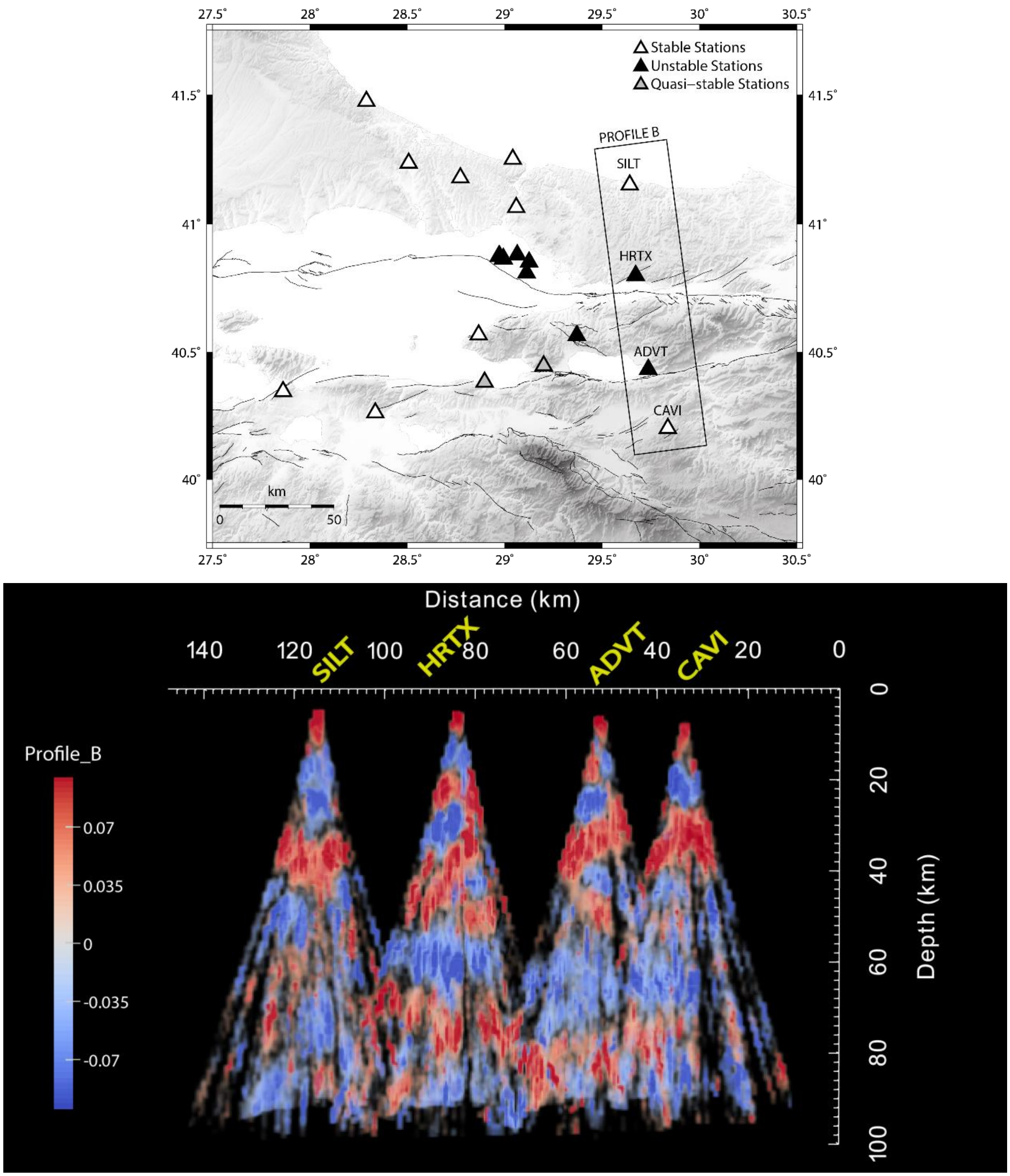

Figure 4.33. The location of Profile B (up) and CCP stacking result of Profile B (down).

CCP Stacking of Profile C

Profile C represents the southern part of Marmara Region which is constituted by EDC, KCTX, MDNY, GEMT, and CAVI stations as shown in Figure 4.34. In the southern part of the Marmara Region corresponding to the Sakarya Zone where the south branch of NAF in Marmara region, the Moho depth is stable around 30-32 km below the EDC, KCTX, and CAVI stations. However, radial RFs under the MDNY and GEMT stations which are close to the south branch of NAF demonstrate Moho declination. This Moho depth variation is not as sharp as in northern branch of NAF given in Profile B. This is may be a result of the southern part of NAF has less effect than northern part of NAF in terms of crustal thickness variation. Moreover, LAB is not as apparent compared to the northern stations due to the gap of the stations. It is mostly seen KCTX, MDNY and GEMT stations nearly at 60 km.

CCP Stacking of Profile D

Profile D represents the NS direction in Marmara Region which is constituted by KLYT, ISK, Prince Islands, ARMT, and MDNY stations as shown in Figure 4.35. Moho depth undulations is very notable from south to the north direction for NS Profile D. Prince islands area consisting of 11 stations specifically is thinnest part of that profile D and a strong mid-crust exists around at 12 km corresponding to 2 sec pulse before Moho arrival existing on waveforms similar to HRTX station in Profile C which is located in the near latitude. For the upper mantle structure, LAB is apparent for KLYT, ISK, ARMT and MDNY at near 60km.

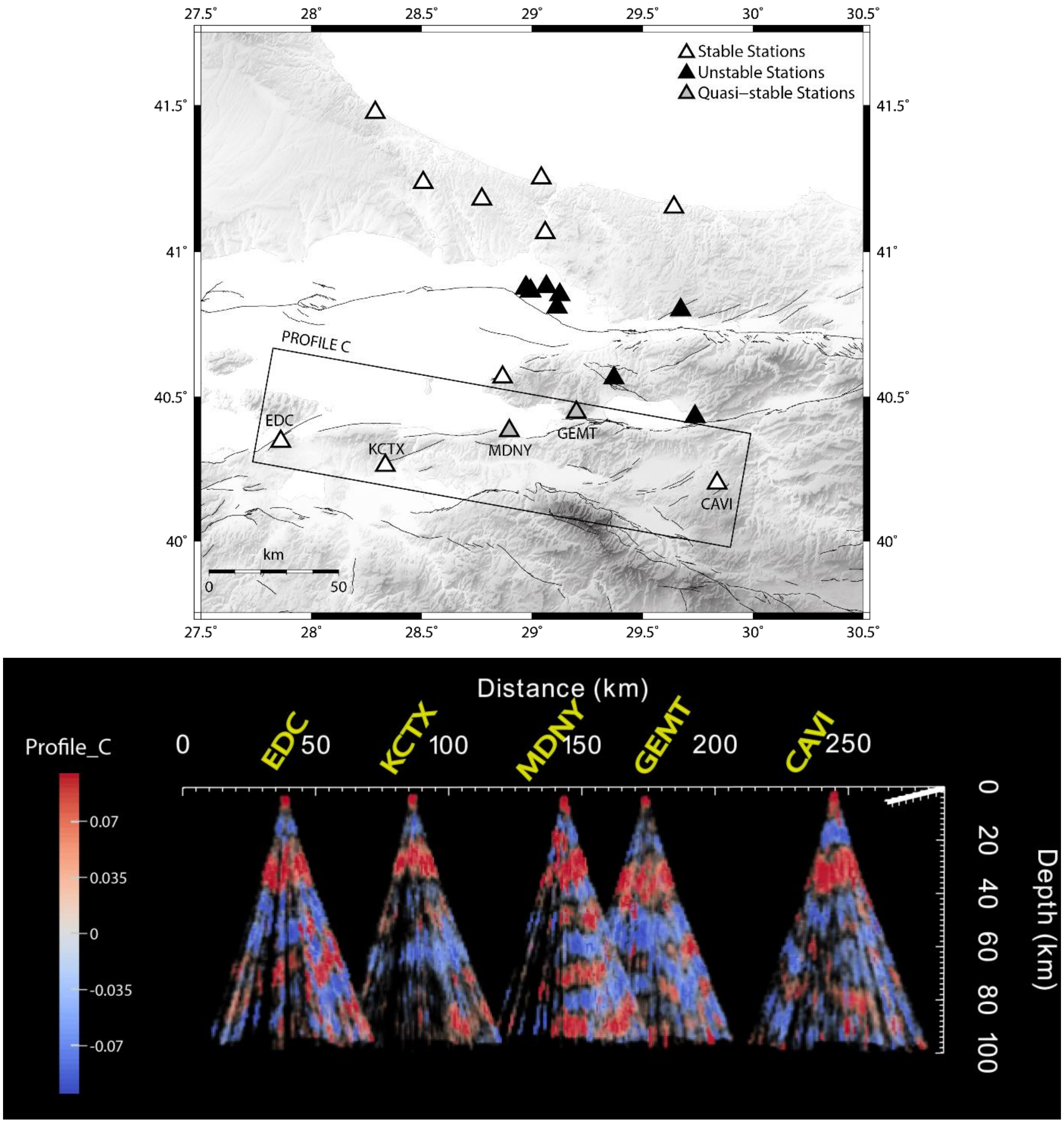

Figure 4.34. The location of Profile C (up) and CCP stacking result of Profile C (down).

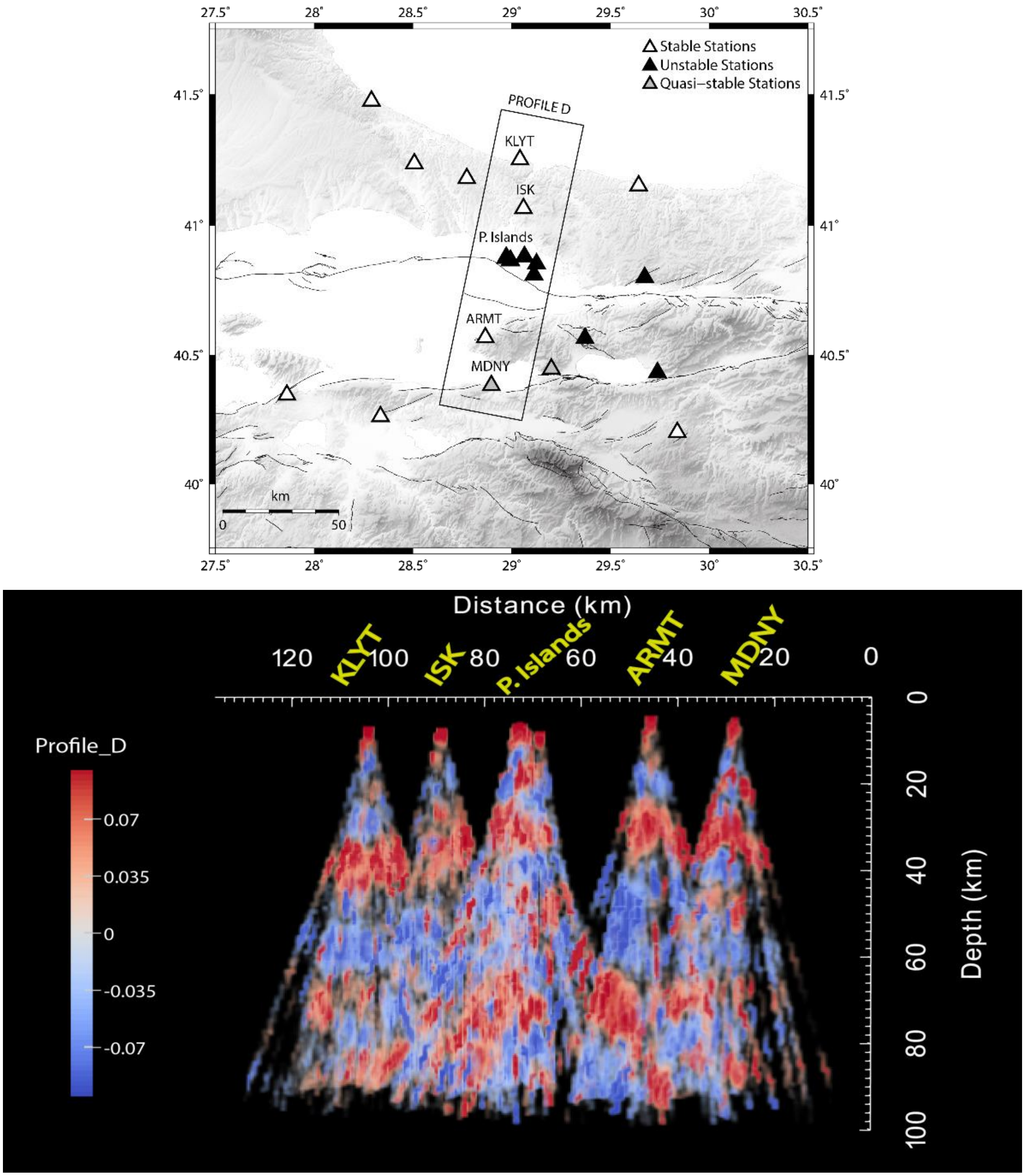

Figure 4.35. The location of Profile D (up) and CCP stacking result of Profile D (down).

CCP Stacking of Profile E

Profile E represents the SE-NW direction in Marmara Region which is constituted by CTYL, CTKS, BGKT, Prince Islands, and YLV, ADVT, and CAVI stations as shown in Figure 4.36. This profile is longer than the other profiles. Perturbations for Moho depth in the Profile E take place from southwest to the northwest direction. Moho gets thinner in Prince Islands and BGKT nearly 30km. In the northest part of the Profile E which is located CTYL station the crustal thickening is observed with respect to the other stations. In the deeper part of the Profile E, LAB is also observed near 60-65km similar to other profiles. However, this is boundary is not apparent as much as Moho discontinuity.

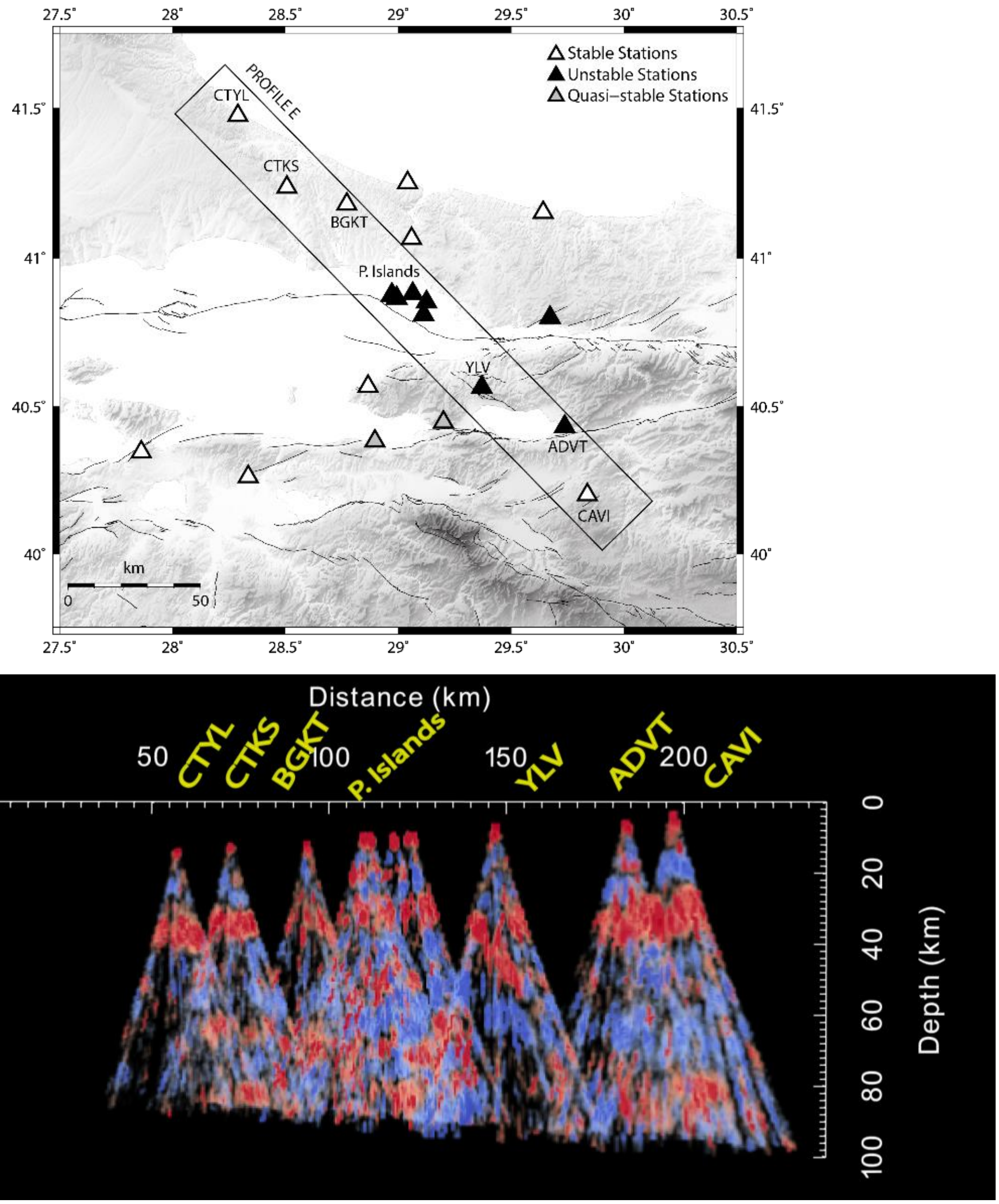

Figure 4.36. The location of Profile E (up) and CCP stacking result of Profile E (down).

4.4. H-κ Stacking Results

In this thesis, two different types of stations according to the character of the receiver function are observed as mentioned in Data Analysis Section 4.1. The arrival time of pulses on RF waveforms show much variability (2 sec) and are very complex for *Unstable Stations*. On the other hand, *Stable Stations* have less arrival time variation (0.2 sec) and are simpler RF waveform. These two stations which show an intermediate characteristic between stable and unstable ones called as Quasi-Stable Stations.

In the previous CCP stacking method, the data of both types of stations was used to observe the azimuthally dependent crust-mantle structure for different profiles. However, in the CCP method, the apparent thicknesses vary according to a default velocity model such as AK135 and this method gives us an idea of the geometrical variation of the structure along the profiles. However, for obtaining the absolute value of the velocities and thickness one has to use more analytical approaches as in the following section.

H-κ Stacking method (Zhu and Kanamori, 2000) that is described in Section 3.2 is frequently used in RF studies in order to obtain crust thickness for each station in more accurate way with respect to the CCP Stacking method. This method has an advantage of rapid calculation of the Moho thickness depending on an average crustal P wave velocity for large number of earthquakes. On the other hand, this method is disadvantageous because it assumes simple horizontal layers with no lateral variations, of which the average velocity is assumed to be known.

If it is taken into account the advantages and disadvantages of this method as mentioned in Section 3.2, this method provides a better result for basic RF waveform containing apparent Moho pulse. Therefore, it is clear that unstable station in our study, especially those close to the north branch of NAF are not suitable for this method. In these stations, additional pulses such as mid-crust phases occur between direct P and Moho pulse and the signal is quite complex. Converted and reverberated phases from different times in this type of stations can interfere with each other through this stacking method and may result in inaccurate results. So this method was implemented in stable and quasi-stable in order to obtain reliable results by using earthquakes in the BAZ range 0-120 where azimuthal coverage is dominant.

As it is mentioned above, in order to determine the crustal thickness and Vp/Vs ratios H-κ method has been applied to receiver functions. The H-κ stacking method introduced by Zhu and Kanamori (2000) implies the summation over the receiver functions of the weighted amplitudes of each phase at the predicted arrival times for different values of H and κ as explained in details in Chapter 3. In this method, receiver functions from different distances and back-azimuths could be stacked with correspondingly ray parameters. In addition to the ray parameter, a fixed average P wave velocity value in the crust is an important parameter to identify and describe the variation of thickness of the crust. In this study Vp value was chosen 6.3 km/s according to previous studies.

In this study, weighting parameters, w1, w2, and w3, mentioned in Chapter 3 were chosen 0.7, 0.2, and 0.1 according to visibility of the converted Ps phase and its multiples PpPs, PpSs, respectively. As a result, all receiver functions were stacked by using all parameters above mentioned and the crustal thickness and Vp/Vs ratio can be found stacking three phases coherently.

The results of this method listed for each station in Table 4.6 and also presented in Figure 4.37 for northern part of the region and in Figure 4.38 for southern part of the region, respectively. According to our H-K result, CTYL, KLYT and SILT stations which are located in the northern part of the Marmara Region along the coastline of the Black Sea, Moho depth is between 34-36 km and Vp/Vs ratio is between 1.75-1.80. In the southern part of these stations, the Moho depth is between 29 – 33 km for CTKS, BGKT, and ISK stations, Vp/Vs ratios (1.73-1.80). Zor (2006) found a similar Moho depth of 32 km for the ISK station from receiver function study. In the southern part of the Marmara region, the Moho depth is nearly between 29 - 32 km and Vp /Vs ratio changes between 1.68-1.76 for the EDC, KCTX, ARMT, MDNY, GEMT and CAVI stations. In our study, it is found that the average Moho depth and average Vp/Vs ratio are 32 km and 1.76, respectively. Average Moho depth in our result matches well with the previous studies such as Horasan *et al*. (2002), Zor *et al*. (2006), Mutlu (2011) and Vanacore *et al*. (2013).

Table 4.5. H- κ results for stable and quasi-stable stations.

Station (Name)	H (km)	$\kappa = Vp/Vs$
ARMT	31.8 ± 0.62	1.70 ± 0.04
BGKT	29.9 ± 0.14	1.73 ± 0.01
CAVI	31.5 ± 0.45	1.70 ± 0.03
CTKS	32.9 ± 0.95	1.73 ± 0.04
CTYL	34.7 ± 1.34	1.75 ± 0.06
EDC	30.1 ± 0.63	1.74 ± 0.02
GEMT	33.6 ± 0.58	1.76 ± 0.03
ISK	30.6 ± 0.40	1.80 ± 0.02
KCTX	28.7 ± 0.43	1.73 ± 0.03
KLYT	36.8 ± 0.72	1.78 ± 0.03
MDNY	32.9 ± 1.45	1.68 ± 0.07
SILT	35.1 ± 0.34	1.80 ± 0.02

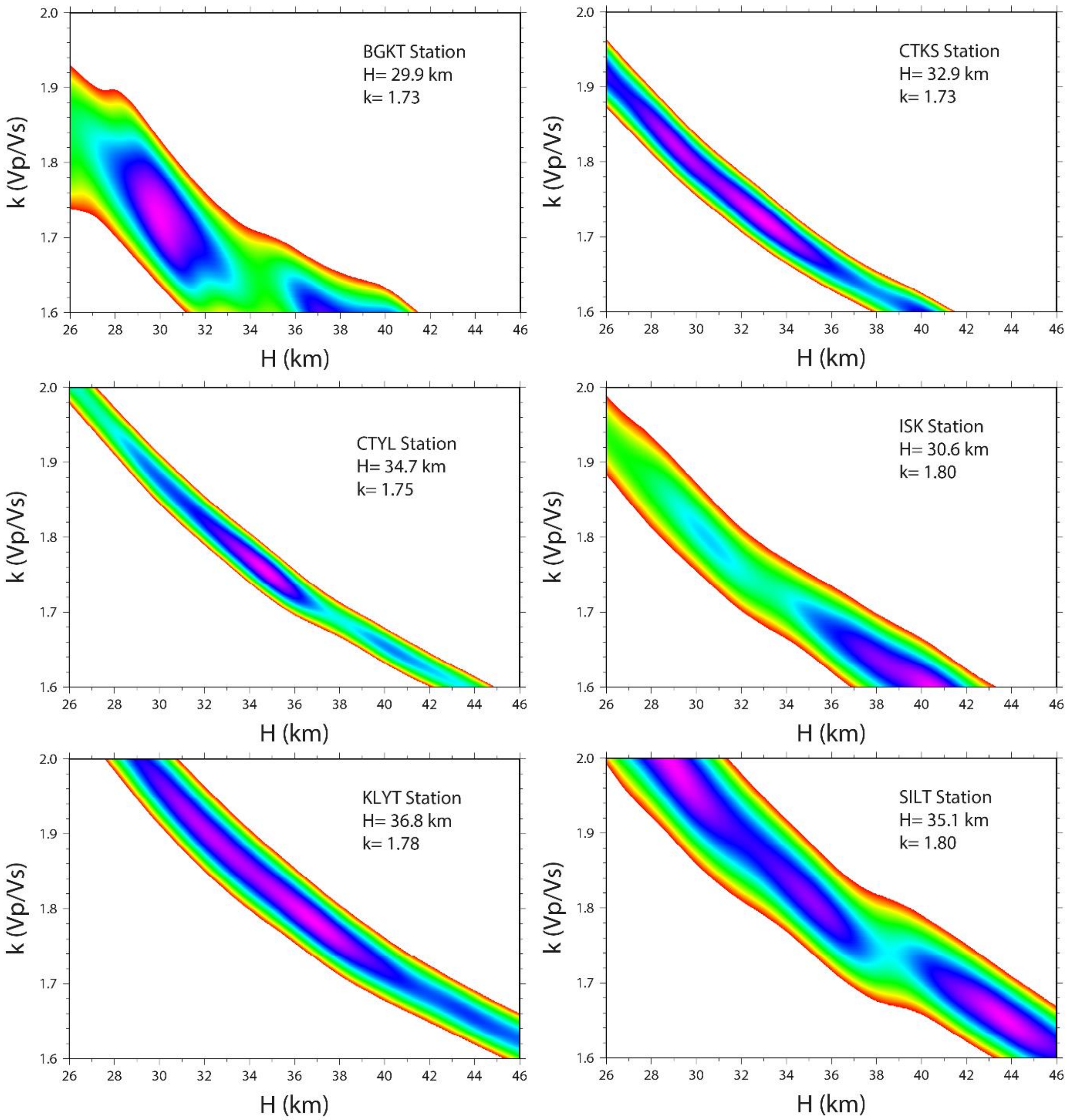

Figure 4.37. H-κ stacking results for northern stations BGKT, CTKS, CTYL, ISK, KLYT, and SILT.

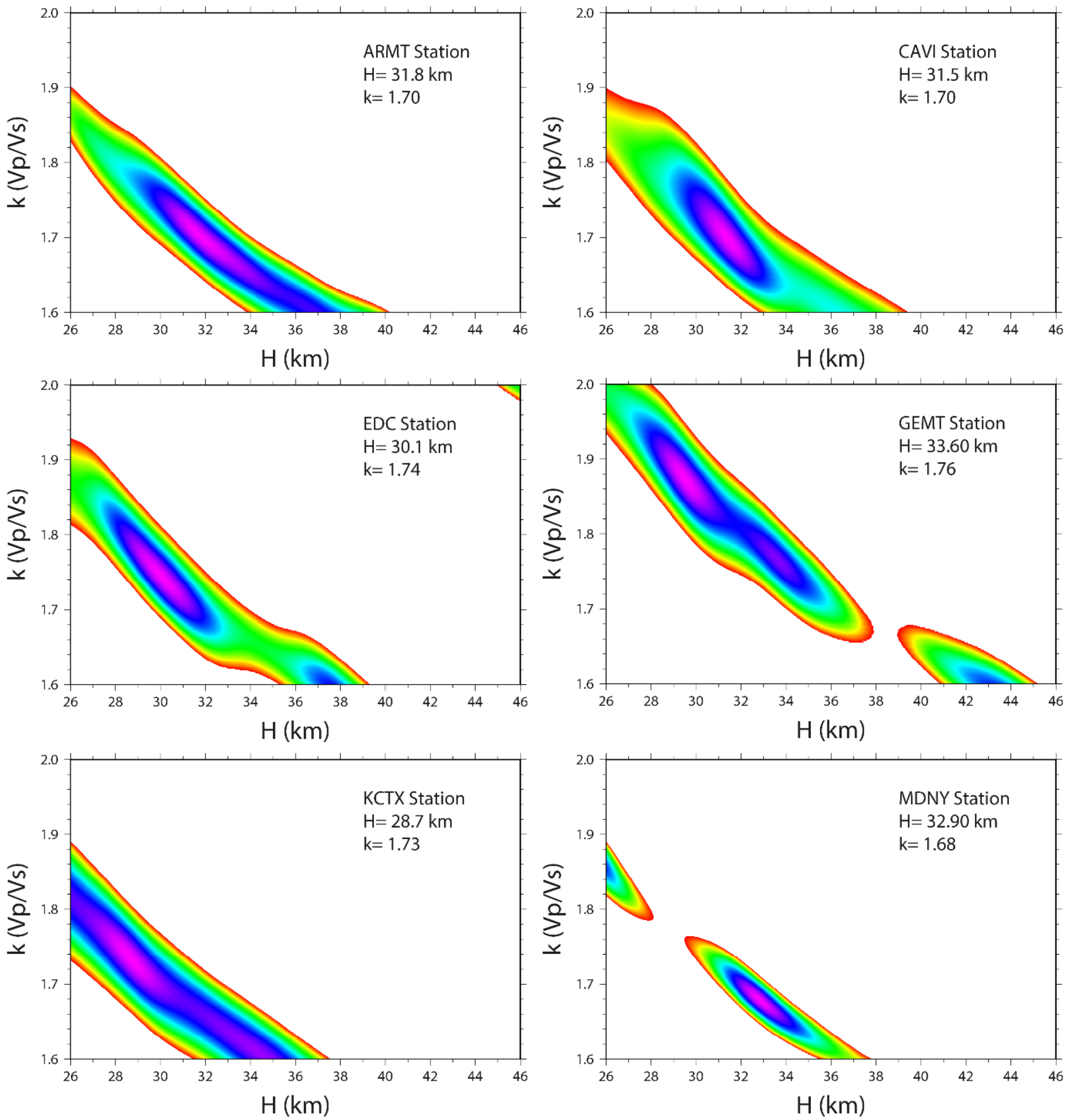

Figure 4.38. H-κ stacking results for southern stations ARMT, CAVI, EDC, GEMT, KCTX, and MDNY.

As a result, the crustal thicknesses in the north Marmara are approximately 35 km at the stations located at the intersection of Istranca Massif and Istanbul Zone. 4 km thinning is observed at stations located between Thrace Basin and Istranca Massif. Complex geological structure in the north of Marmara Region has allowed us to see the variation even in a very small area. In the south of our region, in Sakarya Zone, the crustal thickness is approximately 32 km, but the thinnest crust is found in the Karacabey (KCTX) station (28.7 km). Moho thicknesses show more stability in the southern Marmara. In the vicinity of Armutlu Peninsula and Mudanya, Vp/Vs ratio is lower than neighboring stations. This may be resulted from the average crustal S wave velocity is higher than the other stations.

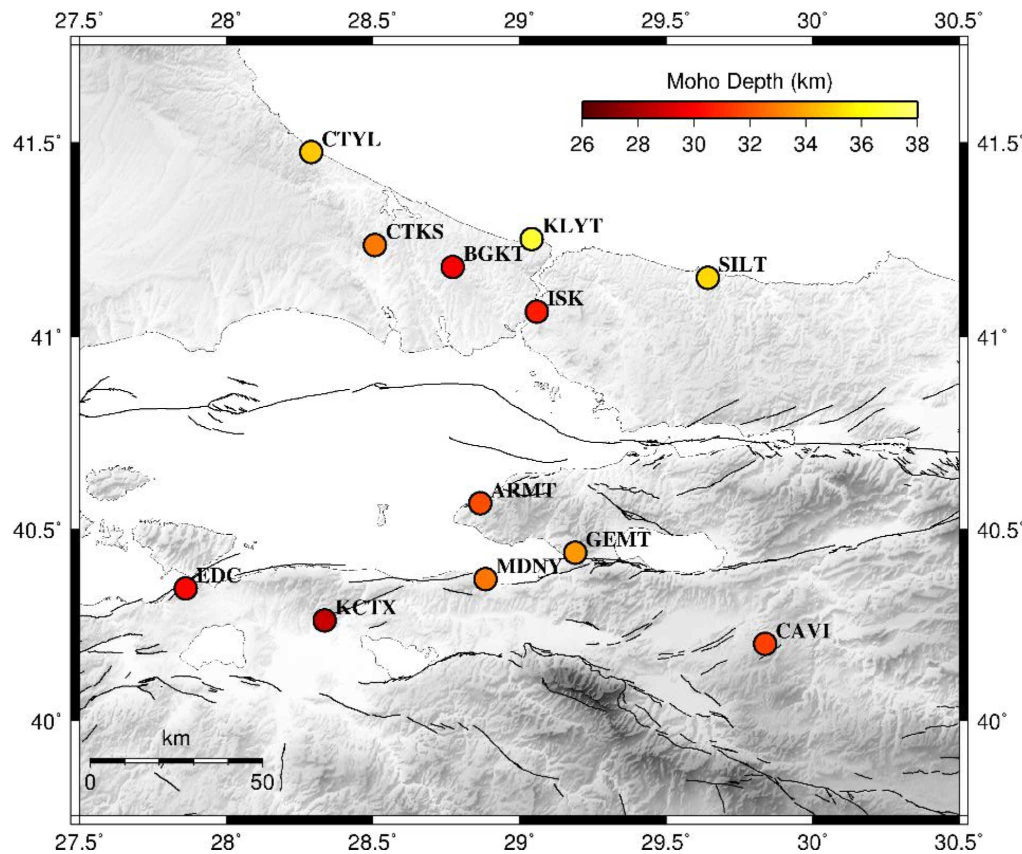

Figure 4.39. The final Moho depth map Stable and Quasi-stable stations used in the study.

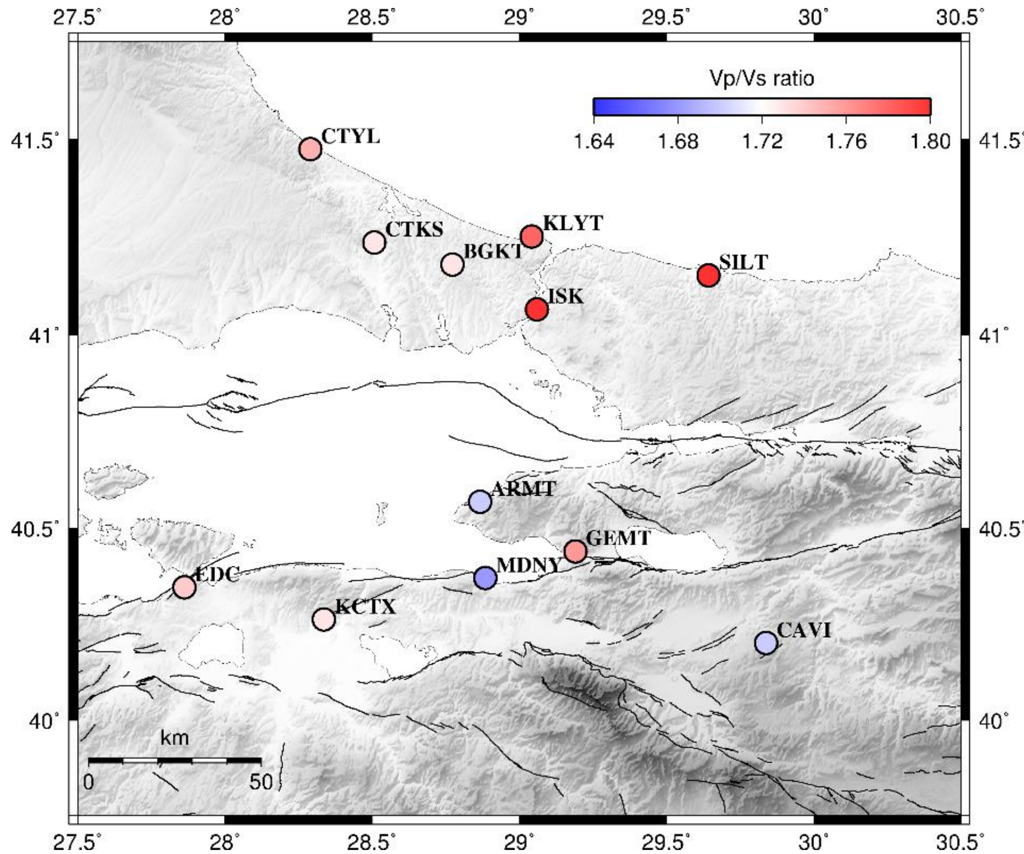

Figure 4.40. The final Vp/Vs ratio map for Stable and Quasi-stable stations used in the study.

4.5. 1D RF Inversion Results

In this section, the radial receiver functions calculated using the method described in the Chapter 3.1 are represented. The inversion is done only for the stations that are classified as stable and quasi-stable. Stations which are located close to NAF and which therefore show 3D complexities are excluded at this step and they are analyzed in the next chapter. Receiver functions for each station are displayed with respect to their back azimuth. The receiver functions are stacked over intervals of 100 each and the average is displayed as the representative one for this slot. The full results, which show the variation of receiver functions over the total 360 azimuth range, are given in APPENDIX A1 and APPENDIX A2 for receiver functions for KOERI and PIRES network stations, respectively. Both the radial and transversal components are shown for each station separately. This section includes only the portion of the azimuth where the receiver functions remain stationary. The inversion is done over the average receiver function, which is found by stacking over the selected azimuth range. This average is given on the top left corner of each figure. The results of the inversion are given as velocity depth profile on the right bottom. The observed and synthetic waveforms resulting from the inversion are included with the ray parameter-fit value. Additionally, H-K result is also inserted on the top right in order to make a comparison of the Moho depth found by both methods. The inversion results for a total of 12 stations are shown in the Figure 4.41 – Figure 4.52, in the alphabetical order.

The database in this study is made up of 12 years data and where the dominant BAZ values lies between 0^{o}-120^{o} ranges. This corresponds to mainly Japan and South-East Asia region where the events are the most numerous. This interval is chosen for the inversion since it guarantees the highest SNR. All waveforms are stacked from that BAZ range in order to create a reliable representation of the receiver function for that station. Note that RFs at the stable and quasi-stable may show about 1 sec variation with respect to the BAZ, even inside the selected azimuth range. Therefore, the stacking has to be made carefully by taking into account the arrival time of the pulses. In this study, the initial model for the 1D inversion is chosen as a default velocity model suggested by Karabulut et al., (2011).

The majority of the inversion give the Moho as the strongest boundary where a velocity change of the order of 0.4-0.5 km/s can be observed. The depth values for the Moho show a remarkable consistency between stations results as well as with the H-K analysis. The most delayed Moho pulse arrival is observed at most northern stations located between Istranca Massif and İstanbul Zone. These are CTYL (4.5 sec), KLYT (5 sec), and SILT (5 sec) from the west to east. The amplitude of Moho is not sharp at SILT station. It is noticed that Moho boundary at both KLYT and SILT stations, has a gradually increasing character, which is different from the other stations where an abrupt change is observed.

For CTKS, BGKT and ISK stations located between Istanbul Zone and Thrace basin, Moho pulse arrival is near 4 sec, 3.8 sec, and 4 sec, respectively from east to west. Amplitude of this pulse is more apparent in CTKS station than the other stations having gradually increasing Moho boundary similar to the most northern station (KLYT-SILT). S wave velocity 4.40 km/sec and Moho depth is about 32 km at CTKS station. Inversion results for these 3 stations are plotted jointly in Figure 4.53. It is clear that these 3 stations which are close to each other and aligned in EW direction, show similar characteristics and therefore point to a single and common structural unit.

In the southern part, Moho boundary is around at 32 km for EDC, KCTX, ARMT, MDNY, GEMT, and CAVI stations located in Sakarya Zone. Moho arrival is around 3.8 – 4 sec and the sharpest Moho is observed at MDNY station with the highest S wave velocity 4.70 km/sec at this boundary. It is observed that between 14 km and 22 km there is a low velocity especially at MDNY and ARMT stations as shown in Figure 4.54. The velocity structures of these stations are plotted jointly in Figure 4.55. It is also clear that the southern stations also show common characteristics in terms of the Moho depth and the general shape of the velocity-depth variation. In particular, a rather weak low-velocity zone appears between 14-23 km depth in all stations. This velocity zone is also observed in the joint inversion results as will be discussed in the next section, but it is even weaker. This is therefore highly likely that it corresponds to the real situation and not an artifact of the inversions. In terms of geodynamics of the region, this slow S-velocity in the lower crust may be interpreted as the sign of a heated crust. It is not surprising to have a hot crust in an environment where the Aegean extension becomes the most prominent geodynamic process. The fact that this low velocity zone is not observed in the northern stations seems to support this idea. It is known that the Aegean extension does not extend beyond the NAF zone and only restricted to region where the southern stations are located.

The general trend of the receiver function inversion at the stable stations show that there is no significant change of the crustal properties on the north and south of the NAF. The variation of the Moho depth is of the order of 1-4 km at most, which is an observation supported by part of the previous work Zor *et al*., (2006), Mutlu (2011) and Vanacore *et al*., (2013), but contradicts other (Kahraman *et al*., 2015; Frederiksen *et al*., 2015). This issue is discussed in more detail in later sections.

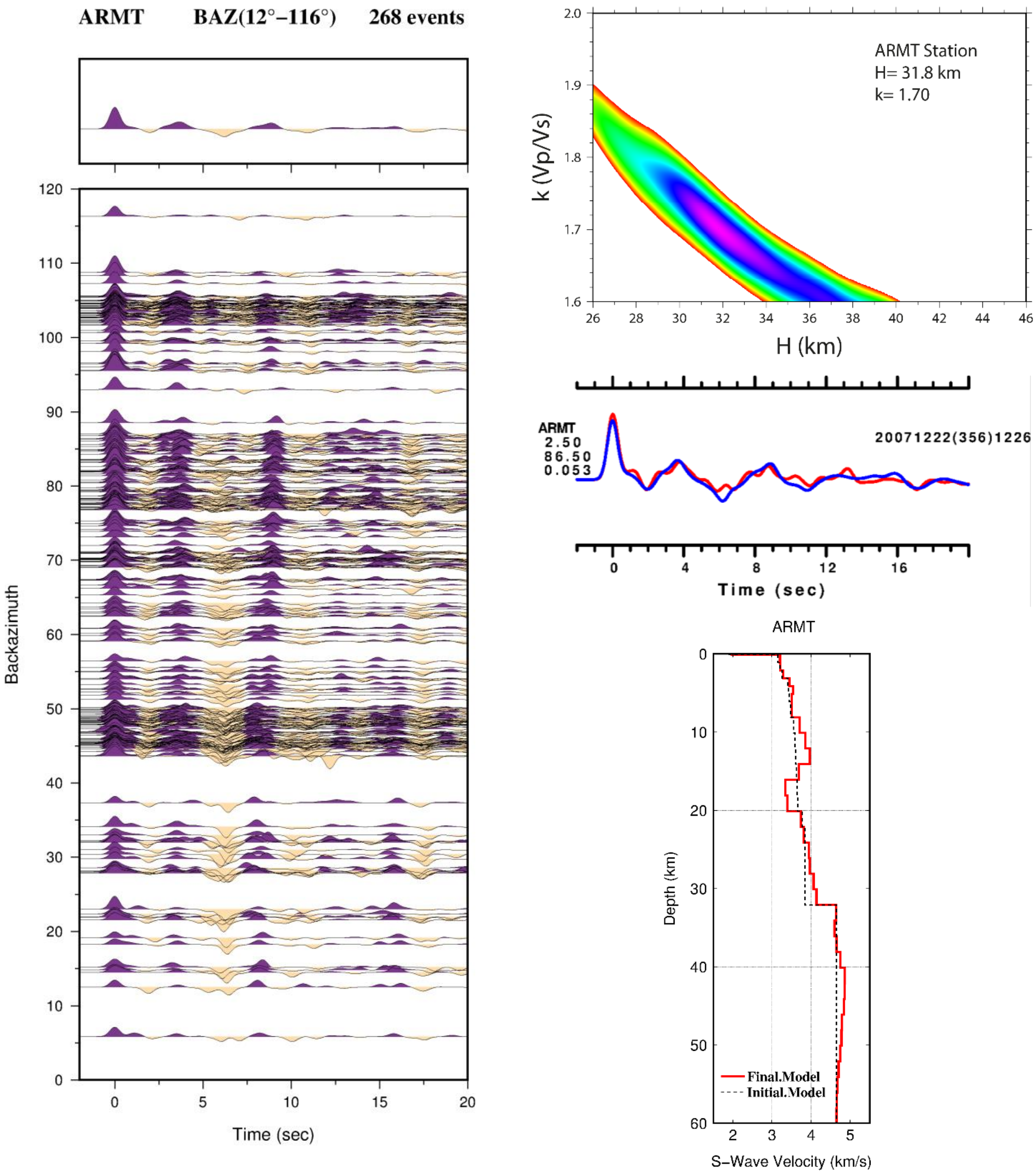

Figure 4.41. ARMT station radial RFs for BAZ 12^{o} - 116^{o} (down-left) and stacked waveform for 268 events (top-left), H-K result (up-right). Blue signal is observed stacked waveform and red signal is predicted waveform for 1D inversion for the initial model (mid-right). 1D inversion result (down-right).

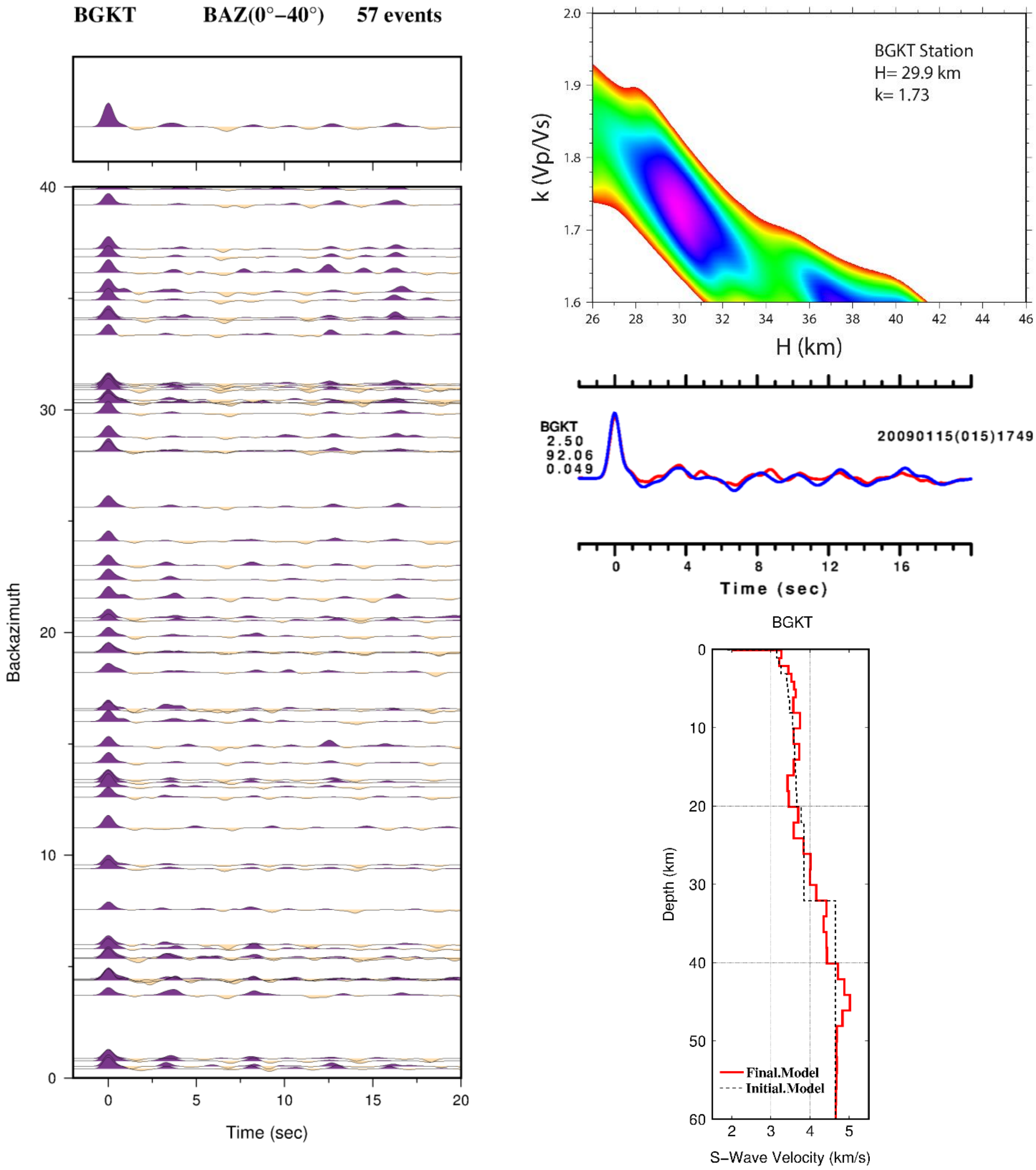

Figure 4.42. BGKT station radial RFs for BAZ 0° - 40° (down-left) and stacked waveform for 57 events (top-left), H-K result (up-right). Blue signal is observed stacked waveform and red signal is predicted waveform for 1D inversion for the initial model (mid-right). 1D inversion result (down-right).

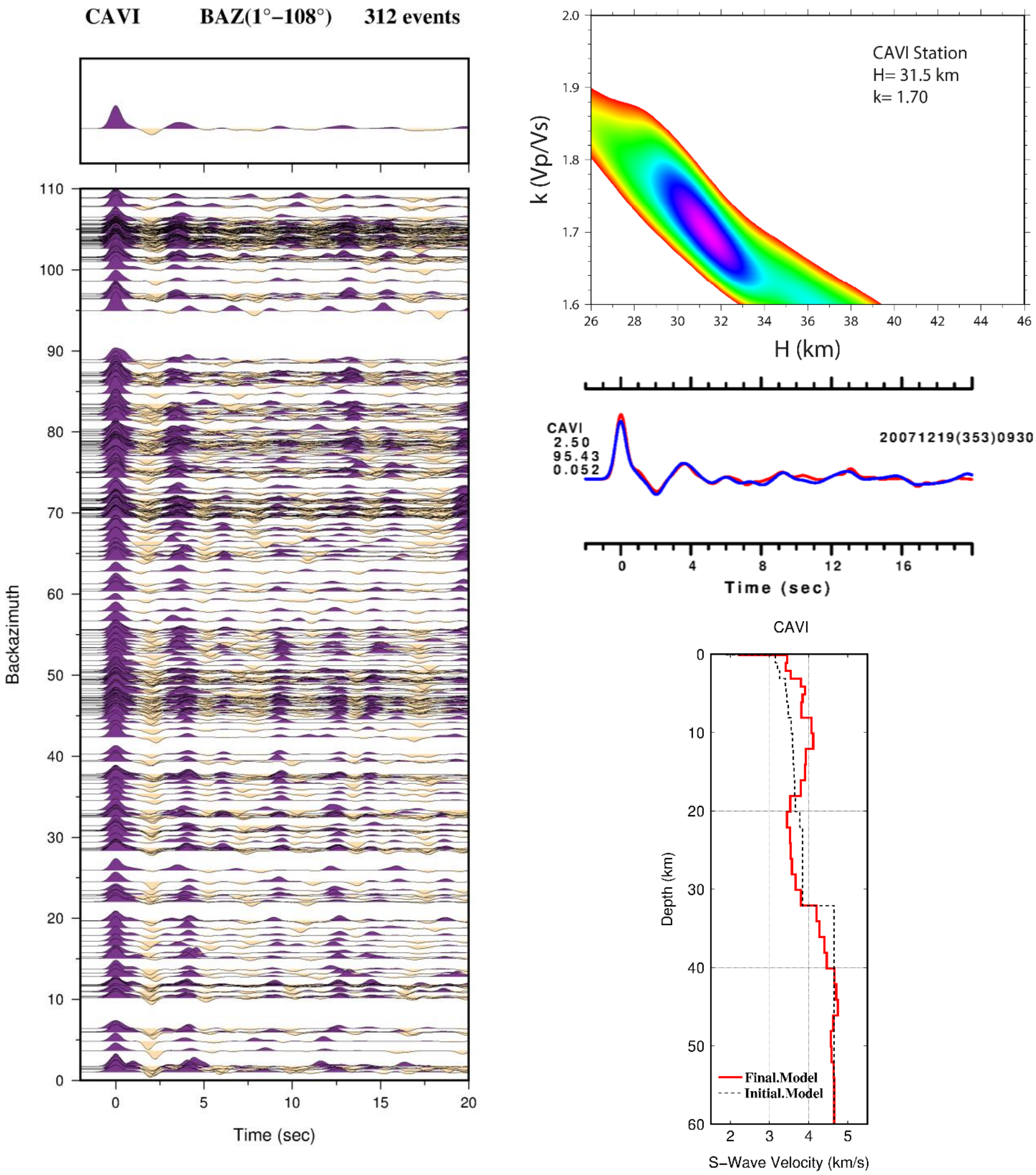

Figure 4.43. CAVI station radial RFs for BAZ 1º - 108º (down-left) and stacked waveform for 312 events (top-left), H-K result (up-right). Blue signal is observed stacked waveform and red signal is predicted waveform for 1D inversion for the initial model (mid-right). 1D inversion result (down-right).

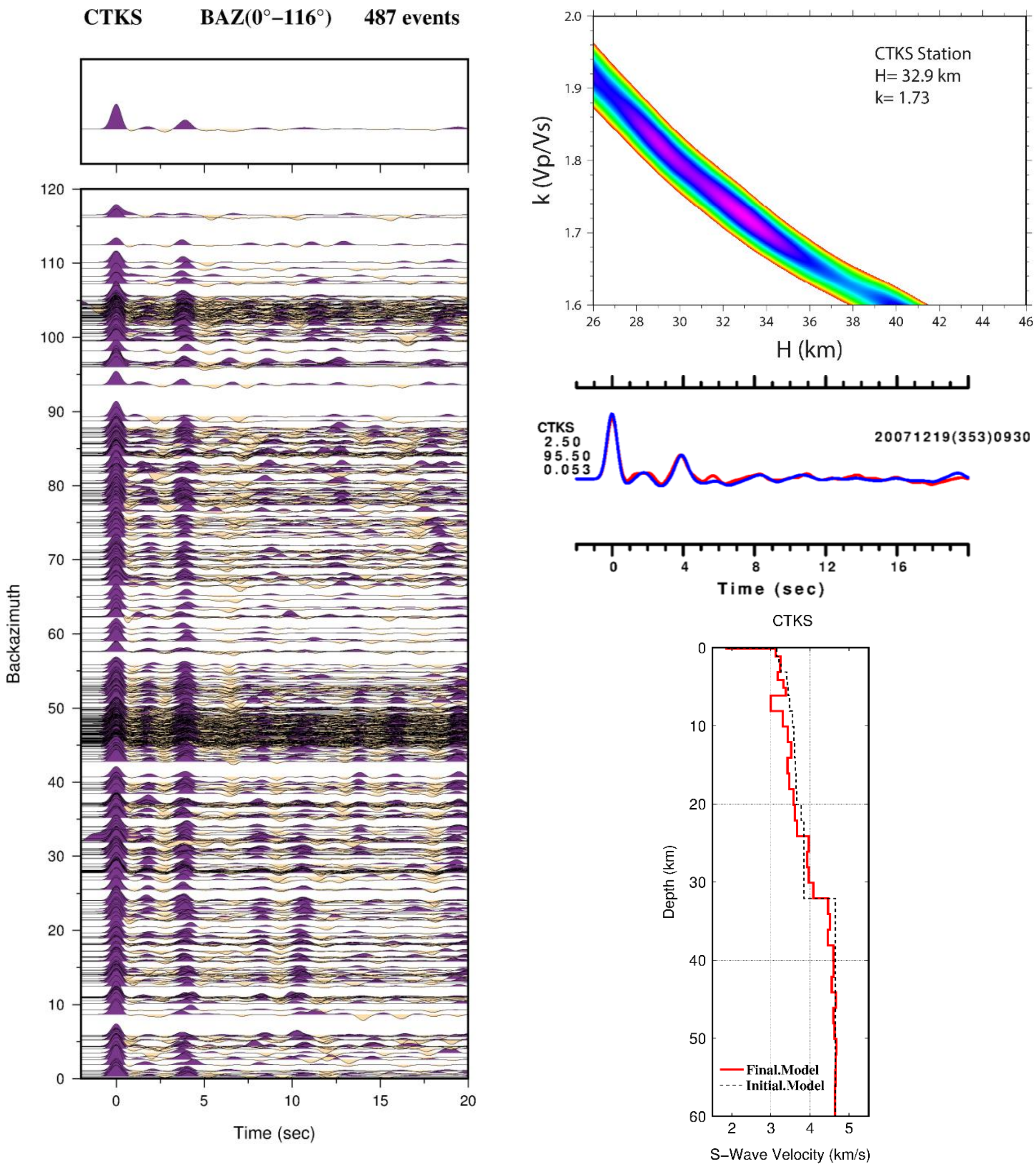

Figure 4.44. CTKS station radial RFs for BAZ 0° - 116° (down-left) and stacked waveform for 487 events (top-left), H-K result (up-right). Blue signal is observed stacked waveform and red signal is predicted waveform for 1D inversion for the initial model (mid-right). 1D inversion result (down-right).

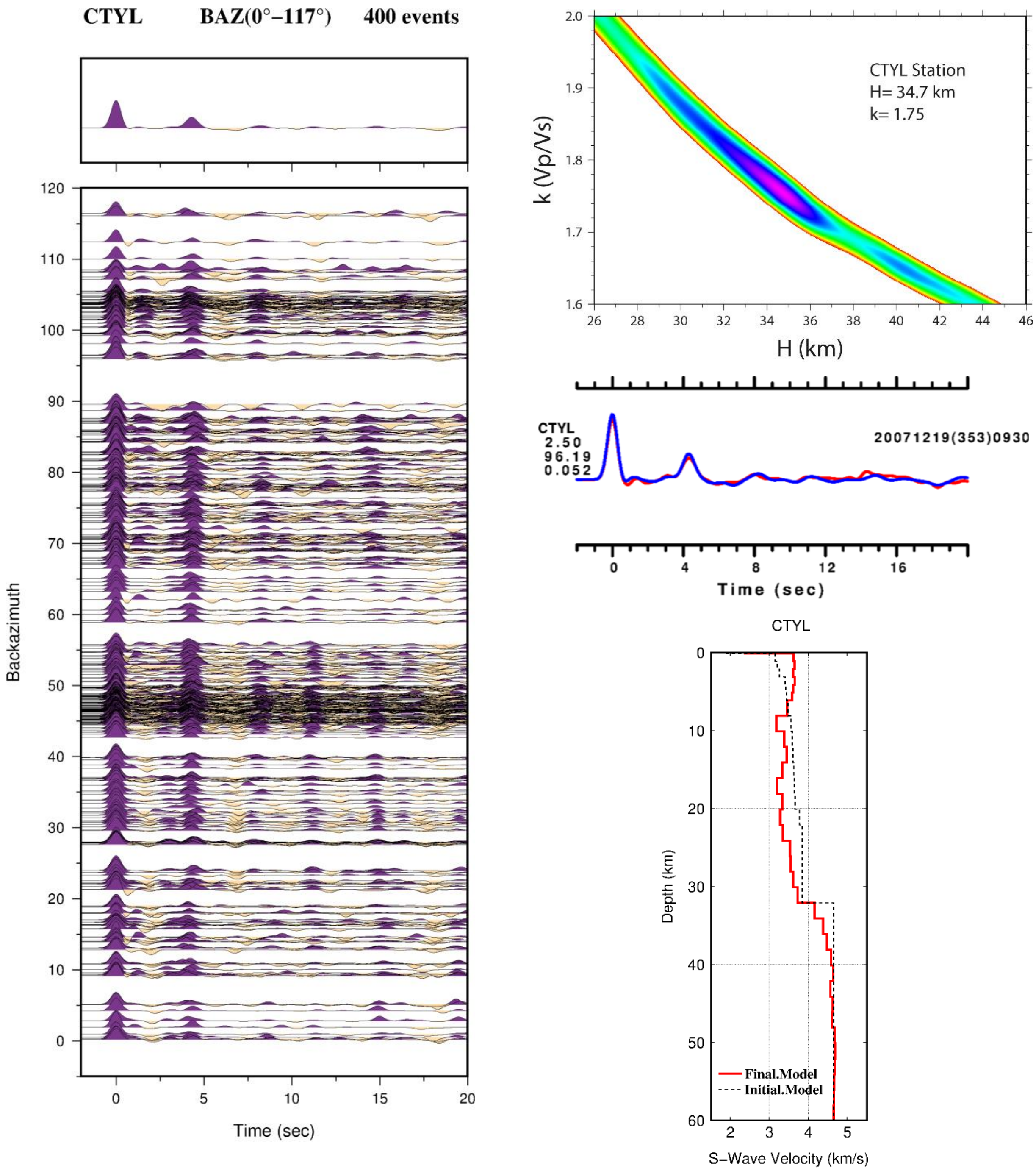

Figure 4.45. CTYL station radial RFs for BAZ 0° - 117° (down-left) and stacked waveform for 400 events (top-left), H-K result (up-right). Blue signal is observed stacked waveform and red signal is predicted waveform for 1D inversion for the initial model (mid-right). 1D inversion result (down-right).

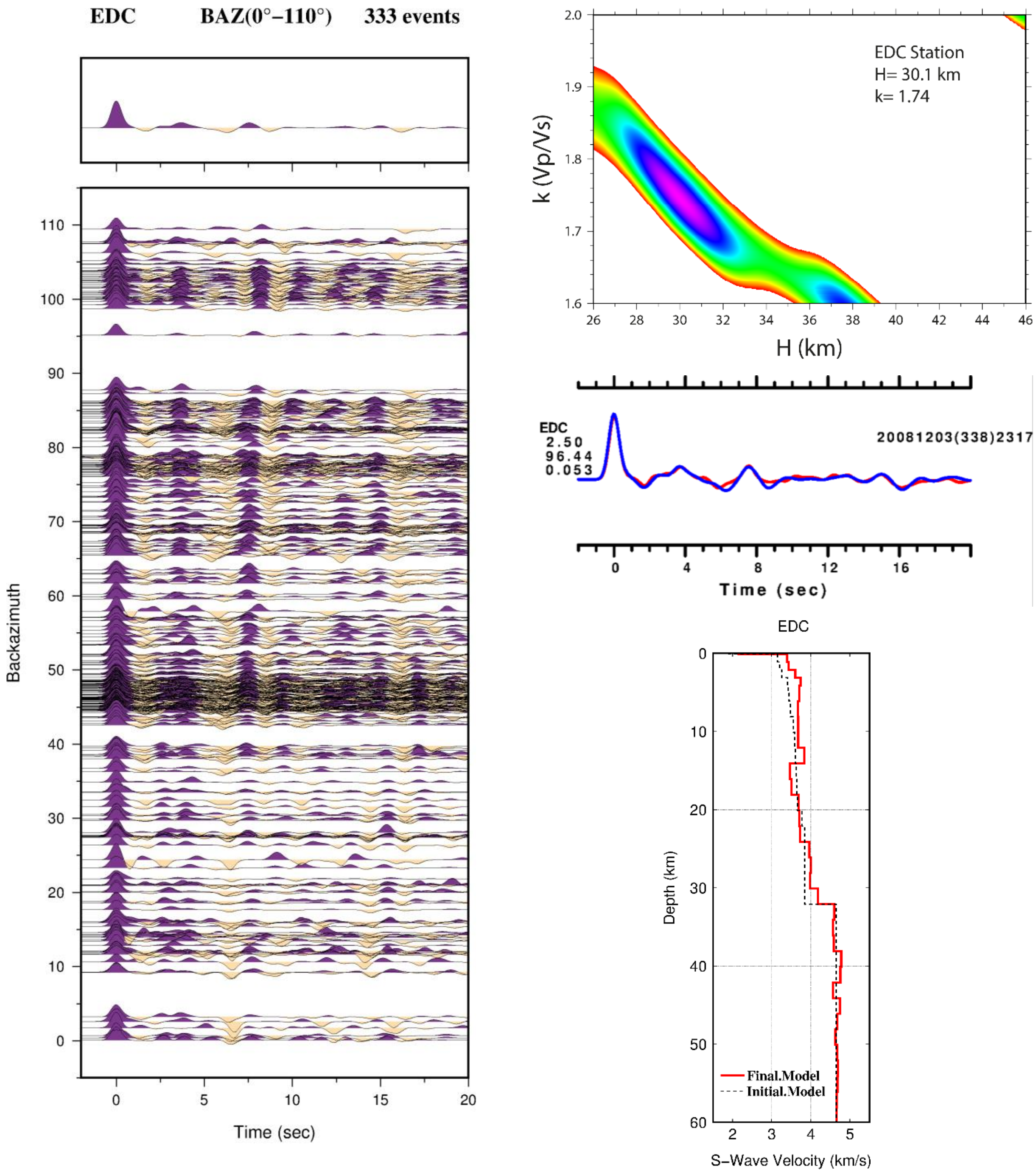

Figure 4.46. EDC station radial RFs for BAZ 0° - 110° (down-left) and stacked waveform for 333 events (top-left), H-K result (up-right). Blue signal is observed stacked waveform and red signal is predicted waveform for 1D inversion for the initial model (mid-right). 1D inversion result (down-right).

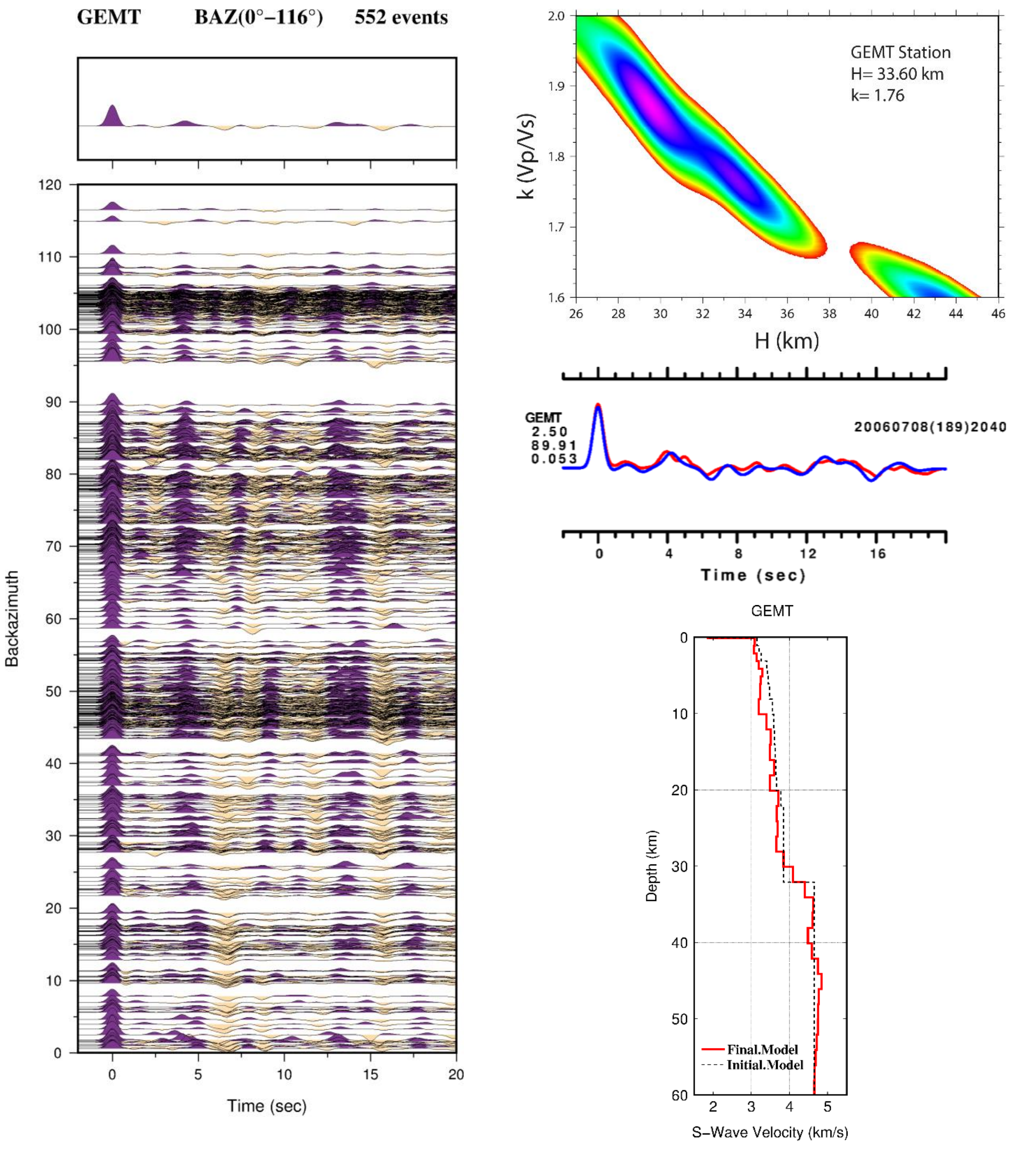

Figure 4.47. GEMT station radial RFs for BAZ 0° - 116° (down-left) and stacked waveform for 552 events (top-left), H-K result (up-right). Blue signal is observed stacked waveform and red signal is predicted waveform for 1D inversion for the initial model (mid-right). 1D inversion result (down-right).

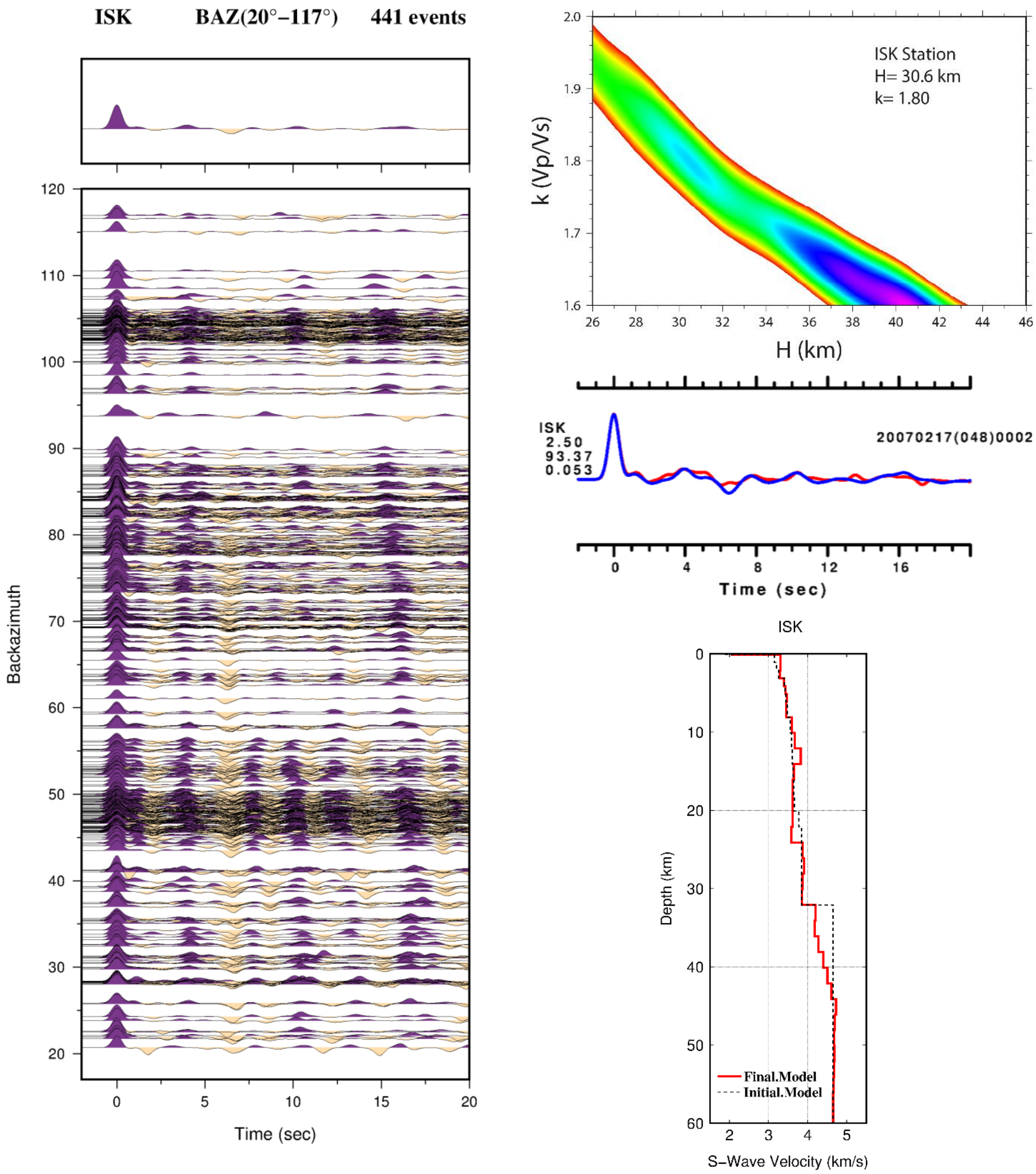

Figure 4.48. ISK station radial RFs for BAZ 20º - 117º (down-left) and stacked waveform for 441 events (top-left), H-K result (up-right). Blue signal is observed stacked waveform and red signal is predicted waveform for 1D inversion for the initial model (mid-right). 1D inversion result (down-right).

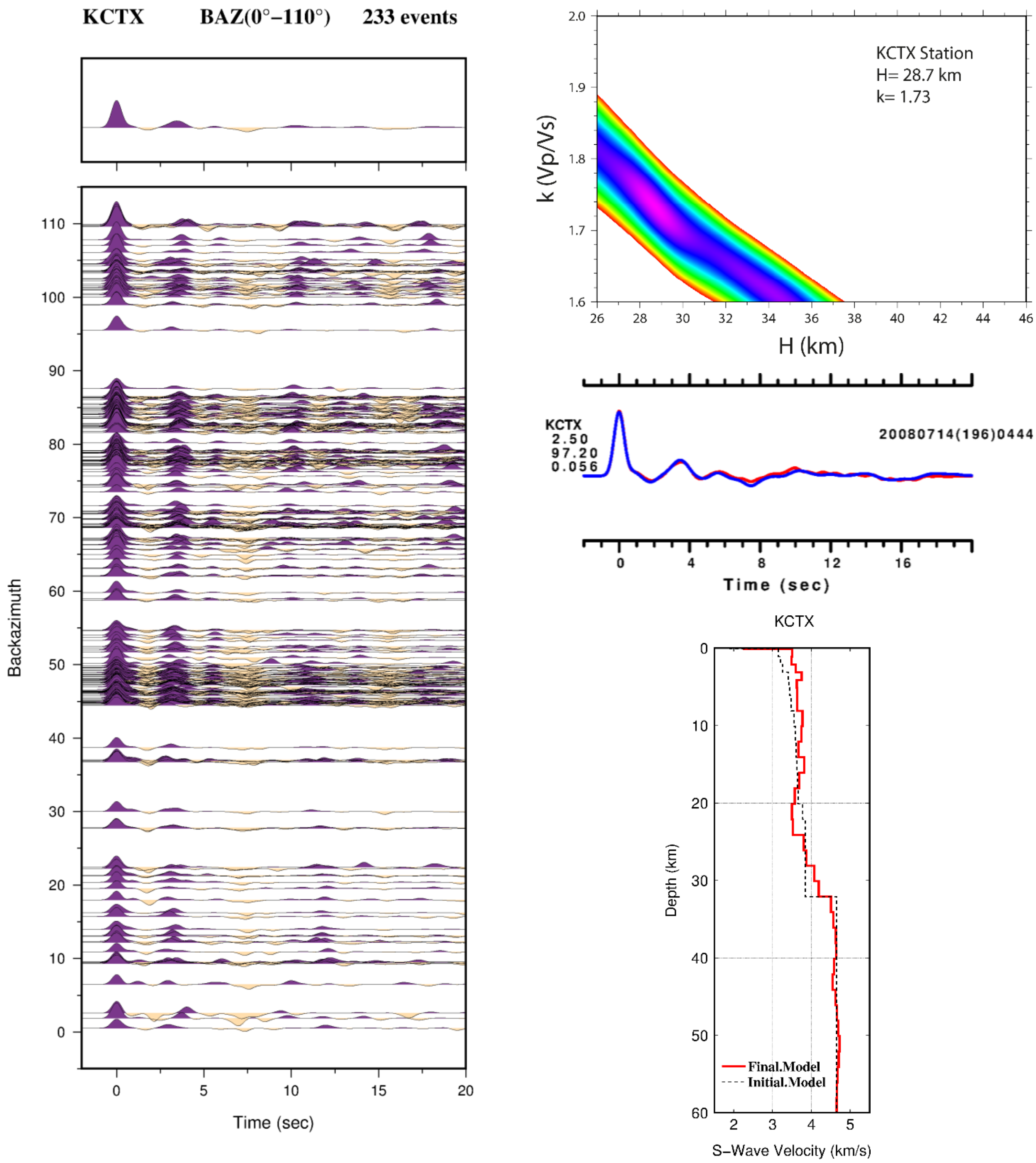

Figure 4.49. KCTX station radial RFs for BAZ 0° - 110° (down-left) and stacked waveform for 233 events (top-left), H-K result (up-right). Blue signal is observed stacked waveform and red signal is predicted waveform for 1D inversion for the initial model (mid-right). 1D inversion result (down-right).

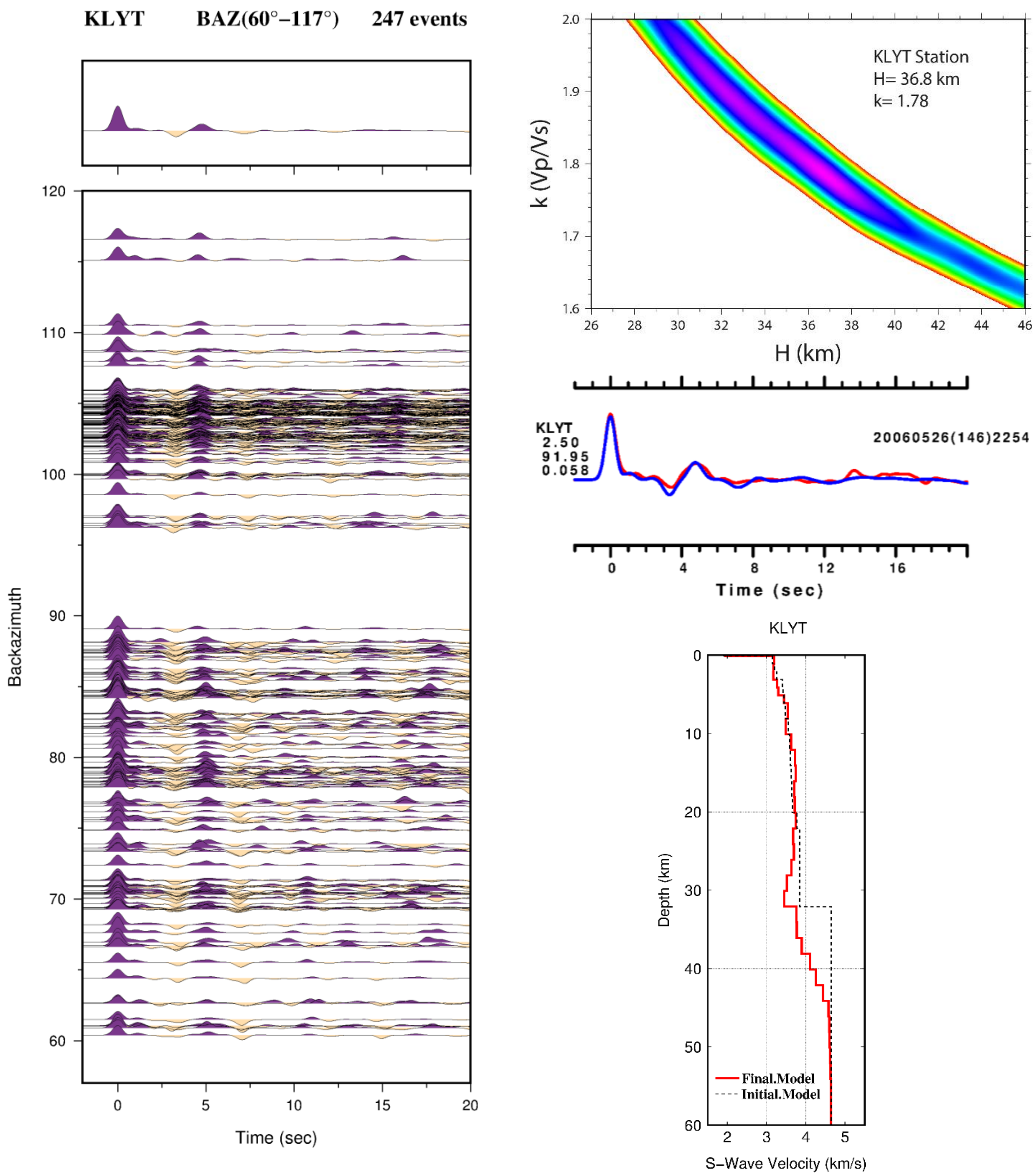

Figure 4.50. KLYT station radial RFs for BAZ 60º - 117º (down-left) and stacked waveform for 247 events (top-left), H-K result (up-right). Blue signal is observed stacked waveform and red signal is predicted waveform for 1D inversion for the initial model (mid-right). 1D inversion result (down-right).

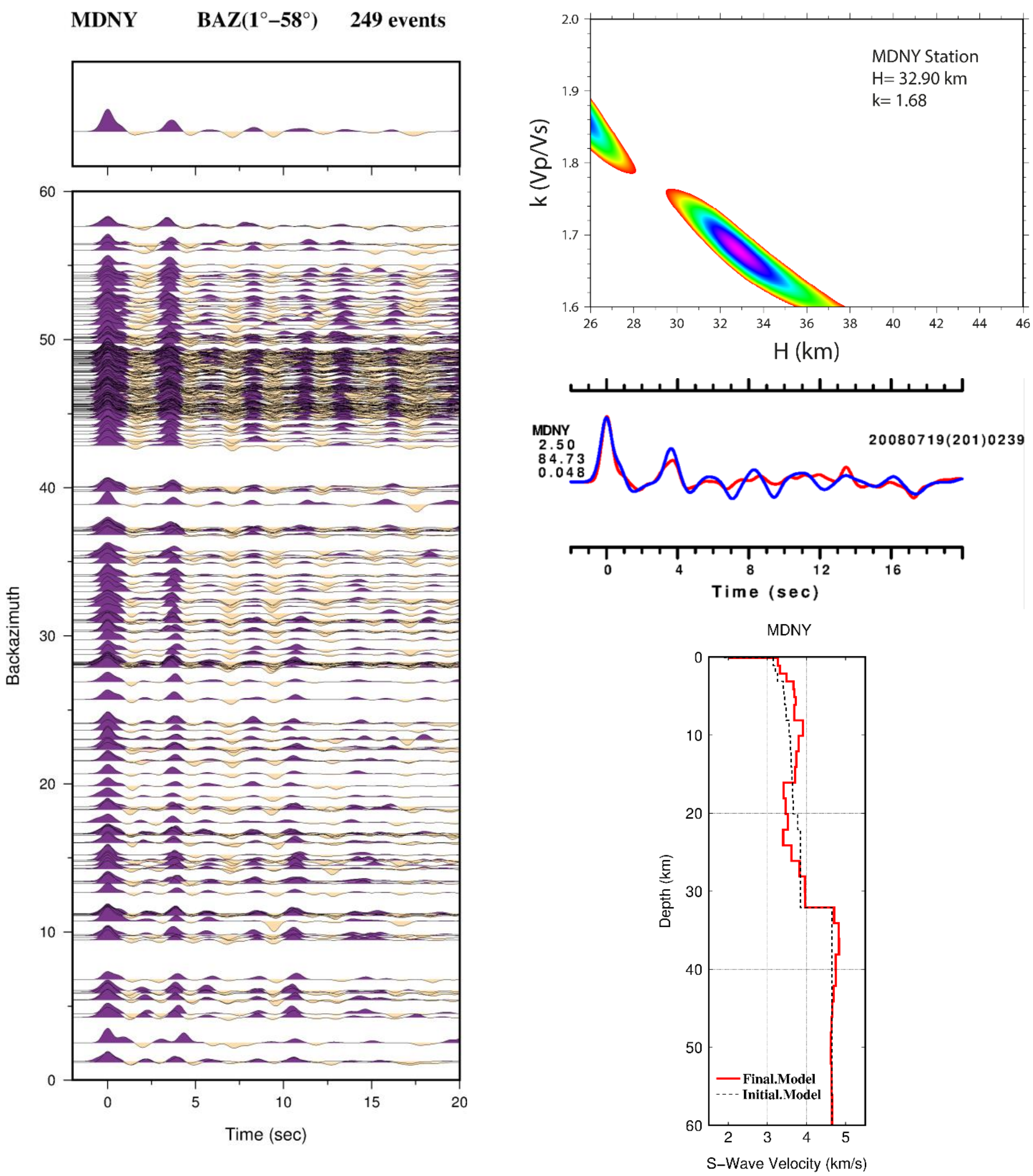

Figure 4.51. MDNY station radial RFs for BAZ 1º - 58º (down-left) and stacked waveform for 249 events (top-left), H-K result (up-right).). Blue signal is observed stacked waveform and red signal is predicted waveform for 1D inversion for the initial model (mid-right). 1D inversion result (down-right).

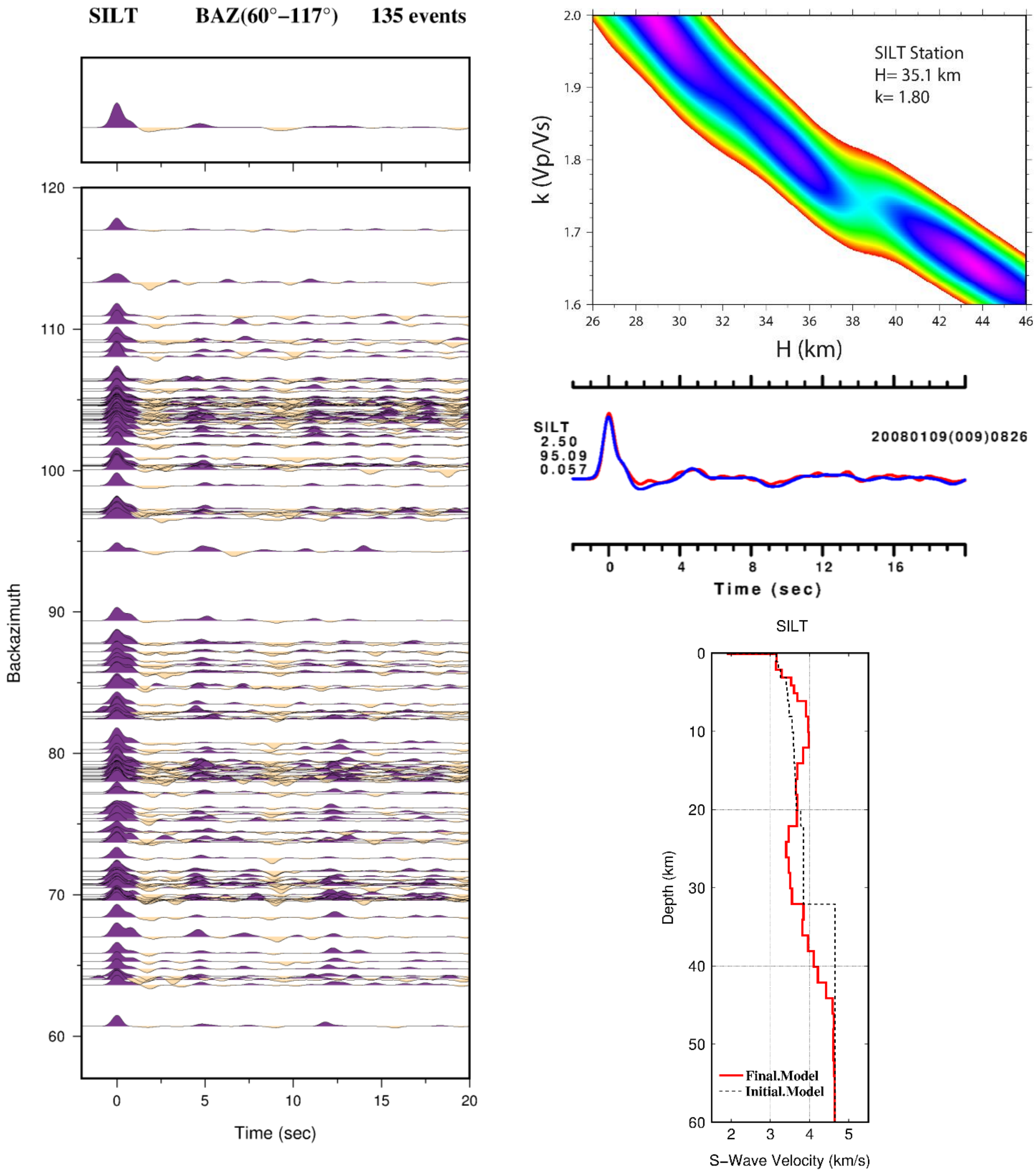

Figure 4.52. SILT station radial RFs for BAZ 60° - 117° (down-left) and stacked waveform for135 events (top-left), H-K result (up-right). Blue signal is observed stacked waveform and red signal is predicted waveform for 1D inversion for the initial model (mid-right). 1D inversion result (down-right).

4.5.1. 1D RF Inversion Results of Northern Stations

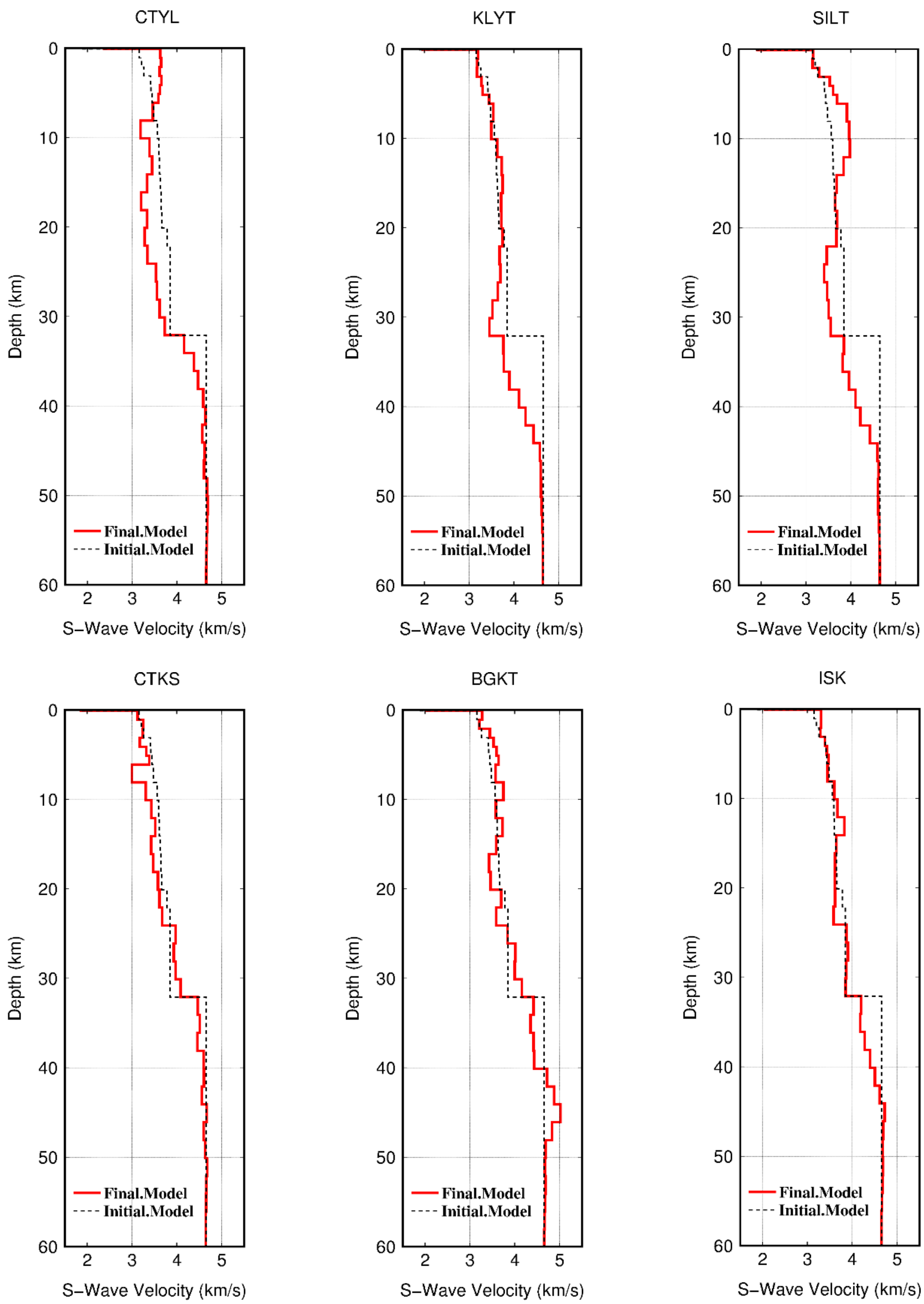

Figure 4.53. 1D inversion results for Northern Stations. Black dotted lines show the initial model (Karabulut et al., 2011). Red lines show the predicted final models.

4.5.2. 1D RF Inversion Results of Southern Stations

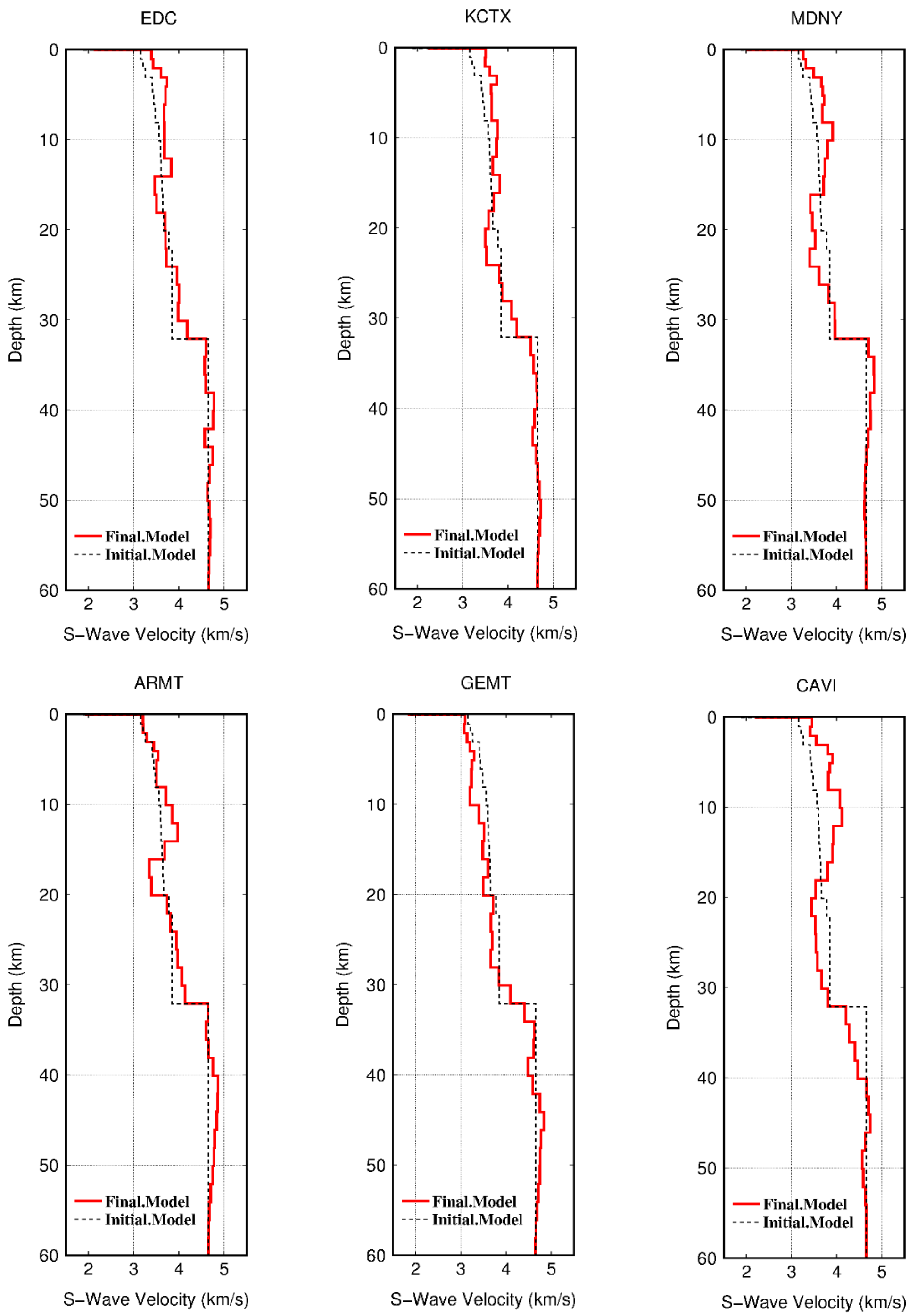

Figure 4.54. 1D inversion results for Southern Stations. Black dotted lines show the initial model (Karabulut et al., 2011). Red lines show the predicted final models.

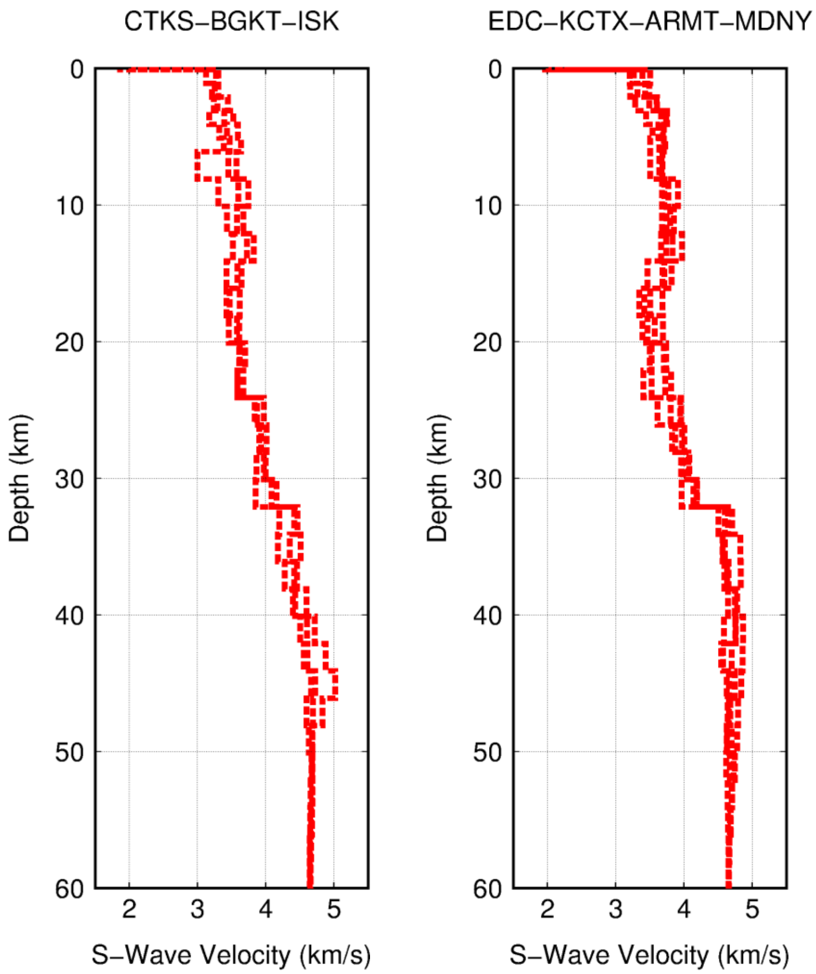

Figure 4.55. 1D inversion results for neighboring stations in northern part of the region (CTKS-BGKT-ISK) and in southern part (EDC-KCTX-ARMT-MDNY).

4.6. Joint Inversion Results

4.6.1. Results of Surface Wave Analysis

After getting results from H-κ, CCP, and 1D inversion technique for stable stations, in order to constrain layers and velocities in a better form, surface wave analysis was applied. 1D receiver function inversion modelling technique is disadvantageous due to the high velocity perturbations between mid-layers while it defines main layers in an advantageous way. For surface wave analysis, group and phase velocity are frequently used especially for deeper part of Earth because they have lower frequency and longer wavelength with respect to the body waves. However, for moderate sized earthquakes have a tendency of surface wave clipping if station and event are close to each other. Therefore, surface waves can be misinterpreted. In order to overcome this risk, event and station should be distant from one another. This study covers a relatively small area and using distant earthquake for getting surface wave is not suitable for our work especially in terms of group velocities representing the whole ray-path velocity information. In order to adapt surface waves to our study two station method was applied by using phase velocities to restrict the surface wave information between two stations. This method is very appropriate for small region like our region.

After a detailed analysis for event selection because dispersion is not appeared from every direction, 2 earthquakes were used from Italy corresponding ray path for south and north of our region separately since represent particular different tectonic structure. Inter-station Rayleigh wave phase velocities from the Italy earthquakes 2016-10-30T06:40:19 Mw=6.5 and 2016-08-24T01:36:34 Mw=6.2 which are shown in Figure 4.5 for CAVI-EDC and EDRB-CTKS stations was calculated between these two stations which can be seen on the map in Figure 4.56 The vertical components and the fundamental modes recorded at two stations on the great circle path corresponding to the event used in the analysis are shown in Figure 4.57 and Figure 4.58.

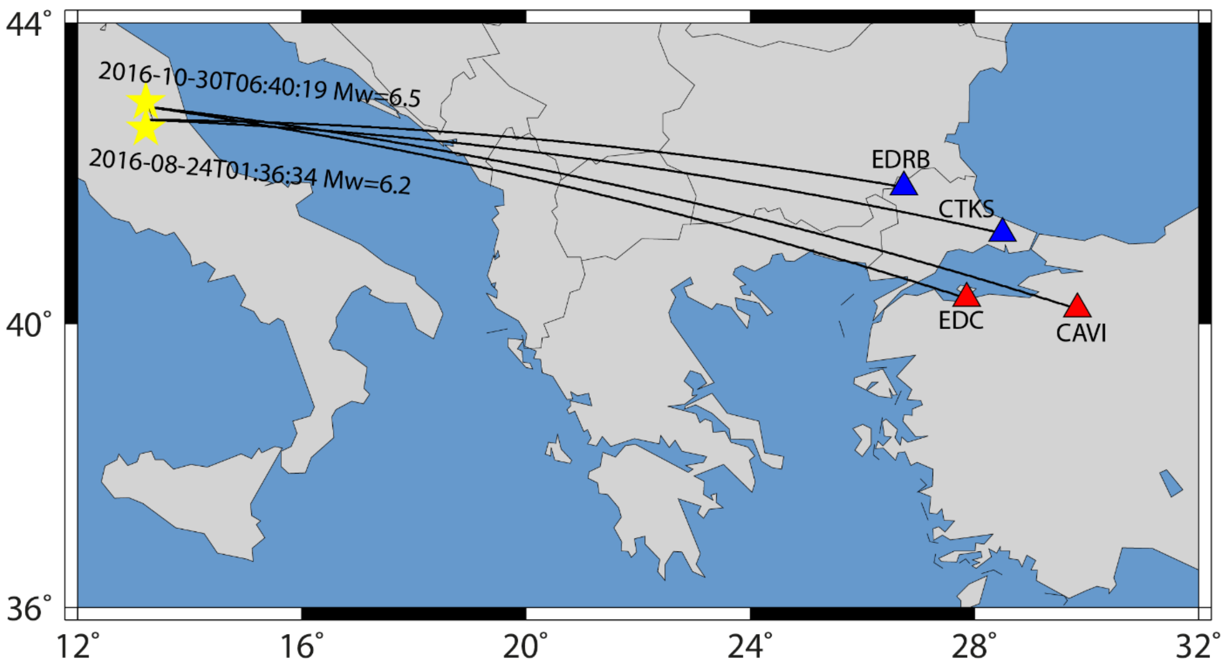

Figure 4.56. Ray paths of Central Italy earthquakes 2016-10-30T06:40:19 Mw=6.5 for EDC-CAVI station (red-triangles) and 2016-08-24T01:36:34 Mw=6.2 for EDRB-CTKS (blue-triangles).

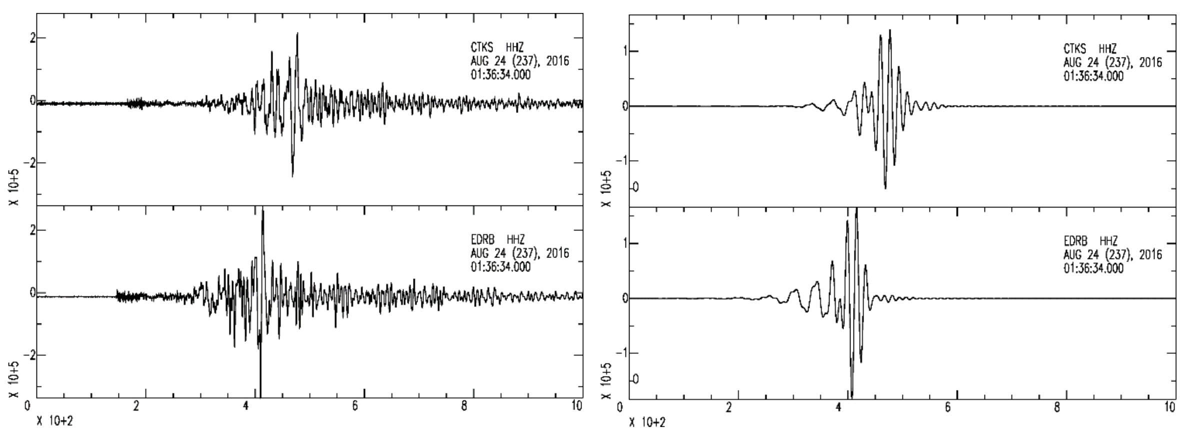

Figure 4.57. BHZ components for Central Italy Earthquake 2016-08-24T01:36:34 Mw=6.2 in EDRB-CTKS stations (left) and the fundamental modes (right).

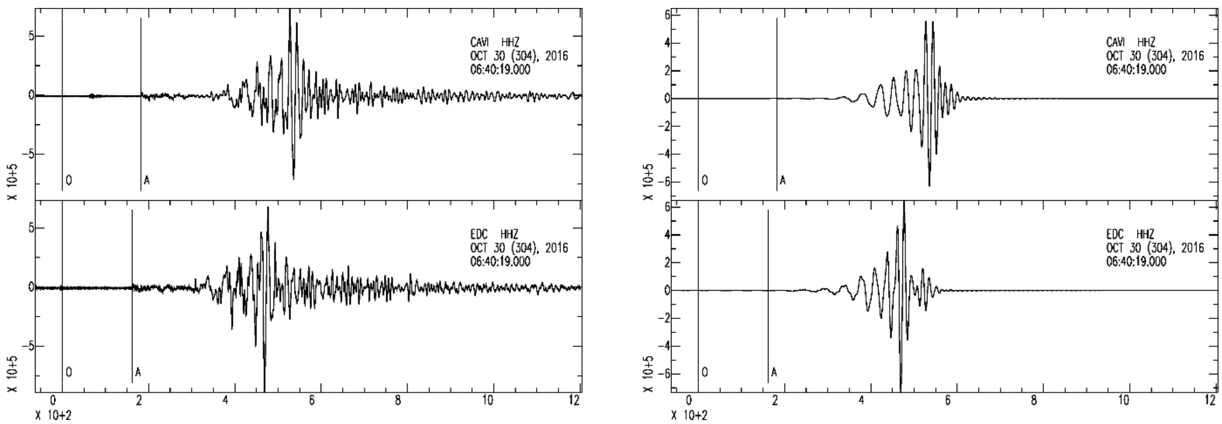

Figure 4.58. BHZ components for Central Italy Earthquake 2016-10-30T06:40:19 Mw=6.5 in EDC and CAVI stations (left) and the fundamental modes (right).

The two different ray-paths used in the study was chosen carefully because of the geologic and tectonic features in Marmara Region. In the northern part, the ray-paths for Central Italy Earthquake 2016-08-24T01:36:34 recorded between EDRB-CTKS stations pass through the Istranca zone and Rhodope Massif. In the southern part, the ray-paths for Central Italy Earthquake 2016-10-30T06:40:19 Mw=6.5 between EDC-CAVI stations cover Thrace Basin, Marmara Sea and Sakarya Zone. In both region, dispersive property is dominant between 10sec and 30 sec which covers our interested depth crustal structure. Phase velocities in the northern part are slightly higher than southern area and S-wave velocities, relatively as shown in Figure 4.59.

Consequently, two S–wave velocity models were presented for different areas in the Marmara region representing as north and south part. On the contrary the RF inversion, surface waves generate smoother S wave velocities and provide better constrain between mid-layers velocities.

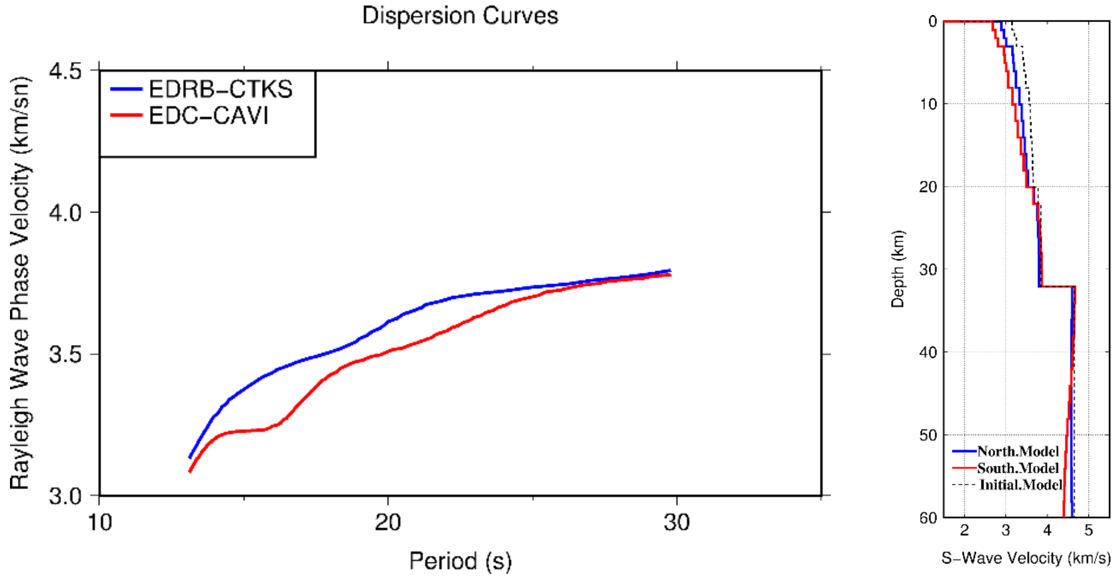

Figure 4.59. The Rayleigh wave phase velocity dispersion curves between EDRB-CTKS and EDC-CAVI pairs (left). Surface wave inversion results in the (right). Blue line representing northern Marmara and red one shows southern Marmara. Black dotted lines show the initial model (Karabulut et al., 2011).

In the next step, joint inversion of receiver functions and surface wave dispersion measurements is used to obtain 1-D S-wave velocity models for selected stations (Julia *et al.*, 2000). Using two different data set jointly gives more reliable results. It is very important to select the weighting parameter (p factor) which influence factor whose value should between 0 and 1, is an a priori parameter that controls the relative contribution of each data set to the solution. If p = 0, the receiver function will be the only data set to contribute to the solution. On the contrary, if p = 1, the surface wave dispersion is the only data set for the inversion. The computer program joint96 implements the joint inversion method (Herrmann and Ammon, 2002). The 1-D S-wave velocity models are directly constructed from the program. In this study p = 0.3 was used to constrain layers mainly from receiver functions.

4.6.2. Joint Inversion Results of Northern Stations

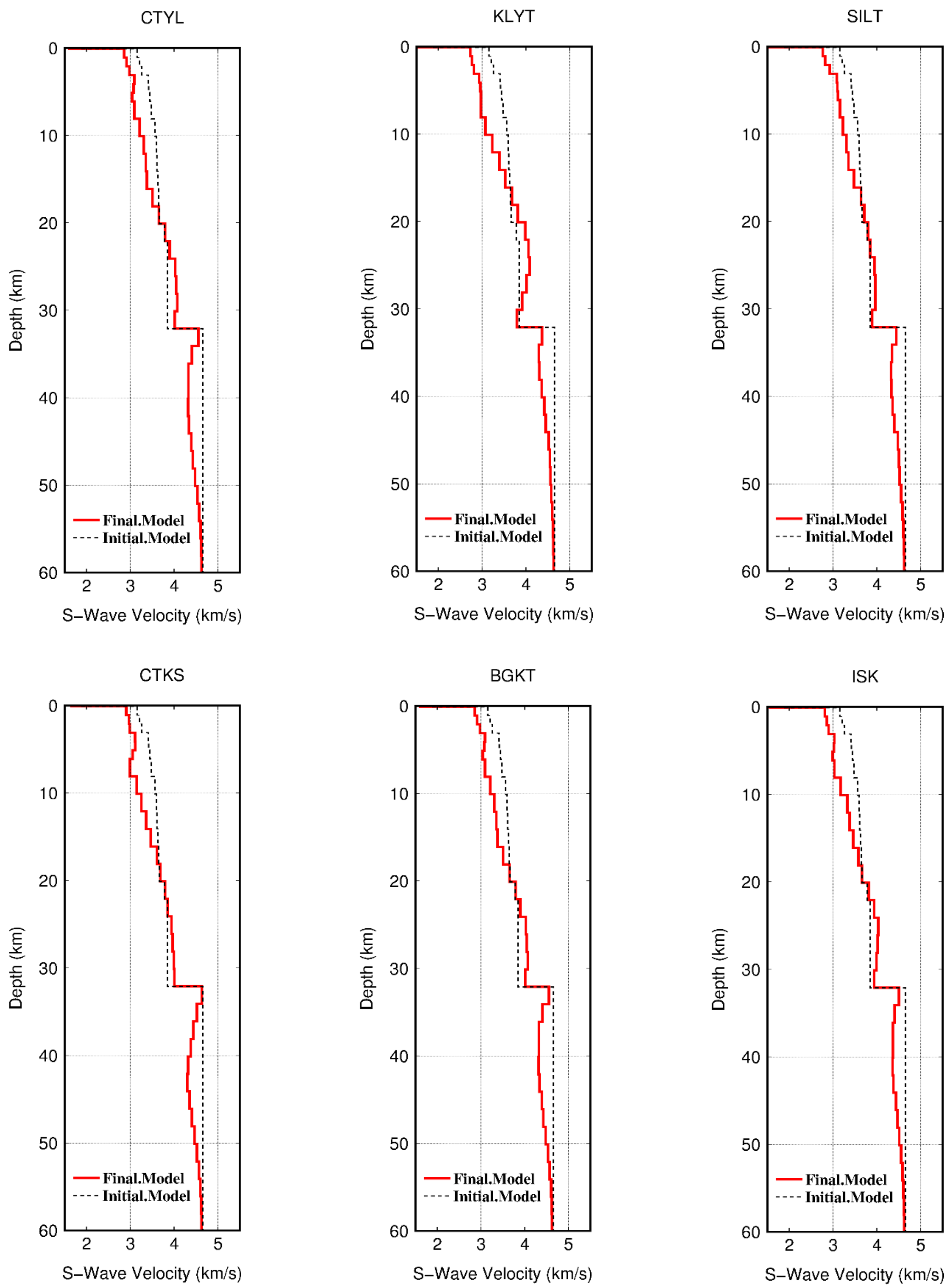

Figure 4.60. Joint inversion results for Northern Stations. Black dotted lines show the initial model (Karabulut et al., 2011). Red lines show the predicted final models.

4.6.3. Joint Inversion Results of Southern Stations

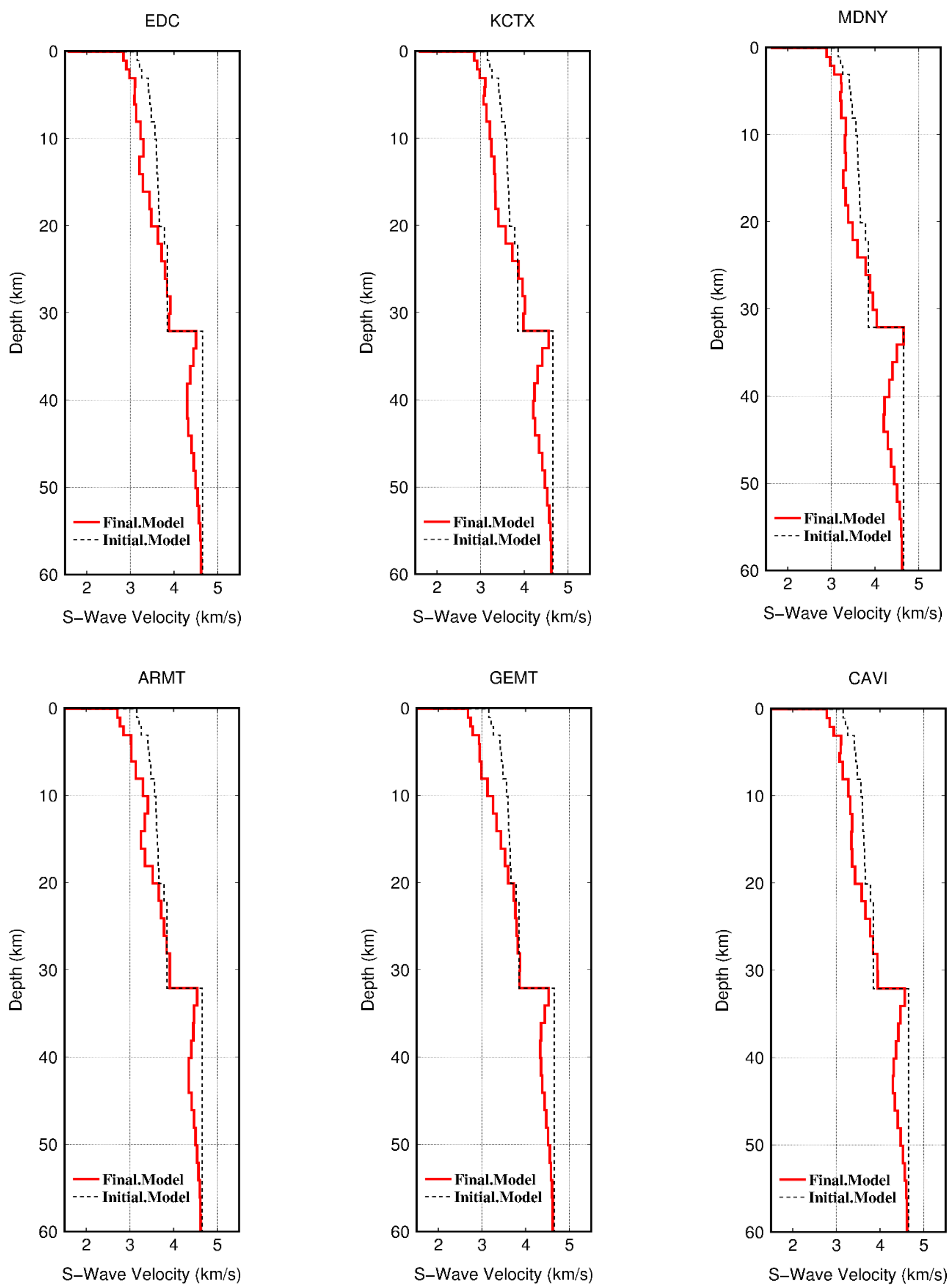

Figure 4.61. Joint inversion results for Southern Stations. Black dotted lines show the initial model (Karabulut et al., 2011). Red lines show the predicted final models.

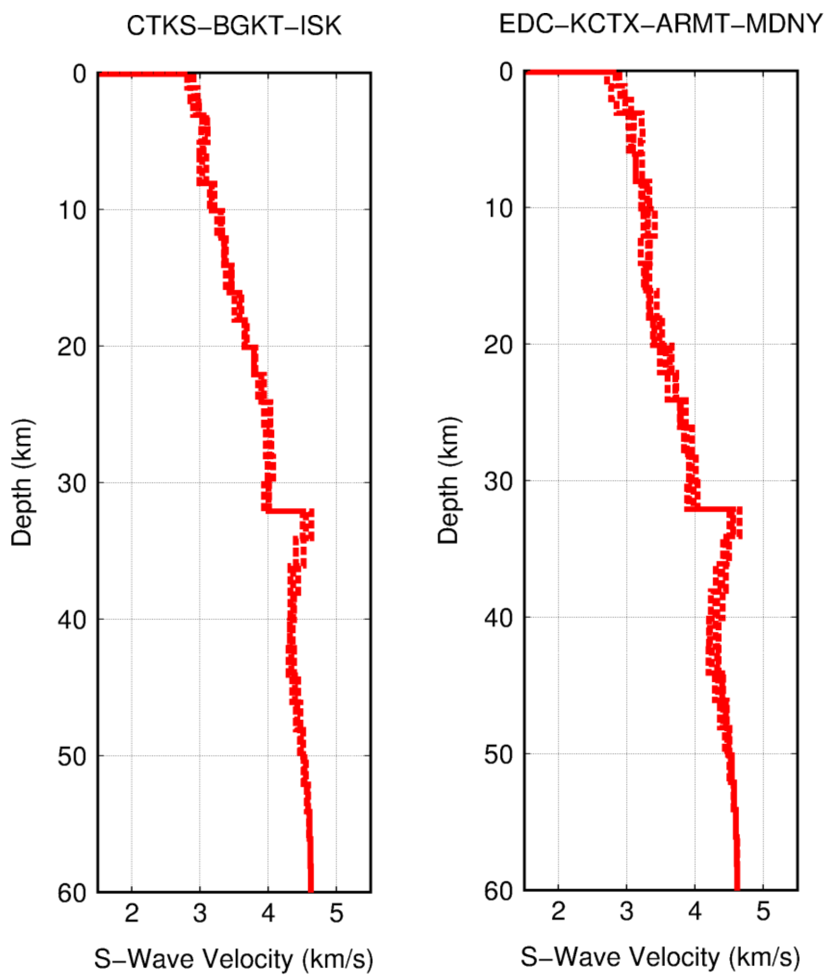

Figure 4.62. Joint inversion results for neighboring stations in northern part of the region (CTKS-BGKT-ISK) and in southern part (EDC-KCTX-ARMT-MDNY).

As a consequence, joint inversion models with respect to the other 2 inversion methods give more realistic results and a better way of interpretation and realistic results. In Figure 4.62, two different S-wave velocity models are shown for north and south part of the Marmara Region. The velocity models get closer to each other for stations situated in the same tectonic regime with a smooth mid-layer and apparent main layers. S wave velocities at between 3-8 km depth are near 3 km/s and 3.2 km/s in the north and south stations, respectively. In the deeper part, southern stations show lower velocity (Vs=3.2-3.5km/s) than northern stations (Vs=3.2-3.9km/s) at 10-20km. Moho thickness is about 32 km for both regions and S wave velocity is about 4.5-4.7 km/s in this boundary. The results are in an agreement with the majority with the previous studies as mentioned before. However, the crustal thickness variation observed across the fault in the Adapazarı area claimed by Frederiksen *et al*., (2015) and Kahraman *et al*., (2015) is not supported in this analysis. These latter studies concern a different area located slightly east of the focus area of this thesis, although with a partial overlapping. However, a major variation of the main characteristics of the crust between these two regions in particular in terms of crustal thicknesses should not be expected. It is therefore likely that these two studies have the drawback of using a data recorded over a short time period and with temporary stations installed over the deep basin of Adapazarı.

5. THREE DIMENSIONAL MODELLING OF RECEIVER FUNCTIONS

The stations that are classified as an unstable are ADVT, HRTX, YLV, and all of the stations at PIRES array. Additionally, two stations, namely GEMT and MDNY show a much less degree of “quasi-stable” characteristics and therefore stand at nearly half way between the two types. In other words, these last two stations were in included in the 1D inversion process of 4.5, such that a horizontal crustal model were obtained for these cases.

Note that all of these “unstable” stations are the ones that are located very close to the NAF, with the exception of YLV. It is clear that the crustal complexity is certainly due to the presence of the fault. Below the 3D modeling for these “unstable” stations are given, namely for the ADVT and HRTX. At the present stage of the study, the 3D model fitting failed the remaining stations. In particular, all stations of PIRES presented very complex receiver function variations, and therefore more involved approaches may be necessary to obtain satisfactory solution, if ever such solution exists.

The characteristics of the receiver functions at station ADVT implies that it should be classified as an unstable station. Some important characteristics can be observed. The first and most important remark is that the transverse component contains significant energy, which implies that there is 3-D effect that influences the receiver functions. In particular, the energy from radial component leaks into the transverse component due the deviation of the incident wave at some particular angles. The second important remark is that the direct pulse (first arrival) of the transverse component changes polarity according to the azimuth of the incoming ray. The polarity is negative roughly for the rays between 0^0-180^0, while it is positive for the 180^0-360^0. This particular pattern, which is typical for a dipping boundary, encourages the introduction of a non-horizontal structure into our model. In this context, an effort is made to produce a shallow dipping layer that will fit the present data in the best possible way.

The initial model that is chosen as a template, corresponds to the structure of the nearest stations with horizontal layers. The receiver function for this model is given in Fig 5.1. Note that since the layering is purely horizontal, the energy at the transverse component is zero, which clearly contradicts the observed data. This simple model is continuously modified by hand and by visual inspection by taking into account the polarity, amplitude, and arrival times of individual pulses in both the radial and transversal components of the receiver functions. The 3D ray tracing code by T. J. Owen (1984) is used for forward modeling and therefore producing the synthetic receiver functions.

The first step is a rough production of receiver functions for the purely horizontal initial model. The fact that only one polarity change is observed in the transversal implies that the only one single dipping structure is enough to produce the required waveform. Since the polarity change is rather strong and early in the transversal, it is concluded that the dipping layer is quite shallow. It is also noted that the polarity changes of the first pulse (at 0 second) in the transversal occurs at 0^0 and180^0 (which corresponds to zero amplitude of the first pulse) with positive polarity in the 180^0-360^0 range. The mid-point between the azimuths where amplitude is zero (ie 0^0 and180^0 in the present data) gives the direction of the strike. Note that the maximum amplitude is at 270^0 and the minimum is at around 70^0-90^0. Considering the geometry, this means that the sallow dipping layer has a strike in the EW direction and it is the dipping towards the North as shown in Figure 5.2. This model produces the required polarity variation observed in the transversal components, and fits well the observed data. The second pulse in the transversal arriving at around 1 sec is also well produced and fits the observed data. Looking at the forward model in the radial component the second pulse arriving 1.0 and 1.5 second later than the first pulse corresponds to the one converted at the shallow layer. Note that this pulse is closer to the direct P at the azimuth of 180^0. This verifies that the fastest arrival meaning updip side, corresponds to south direction in the present case.

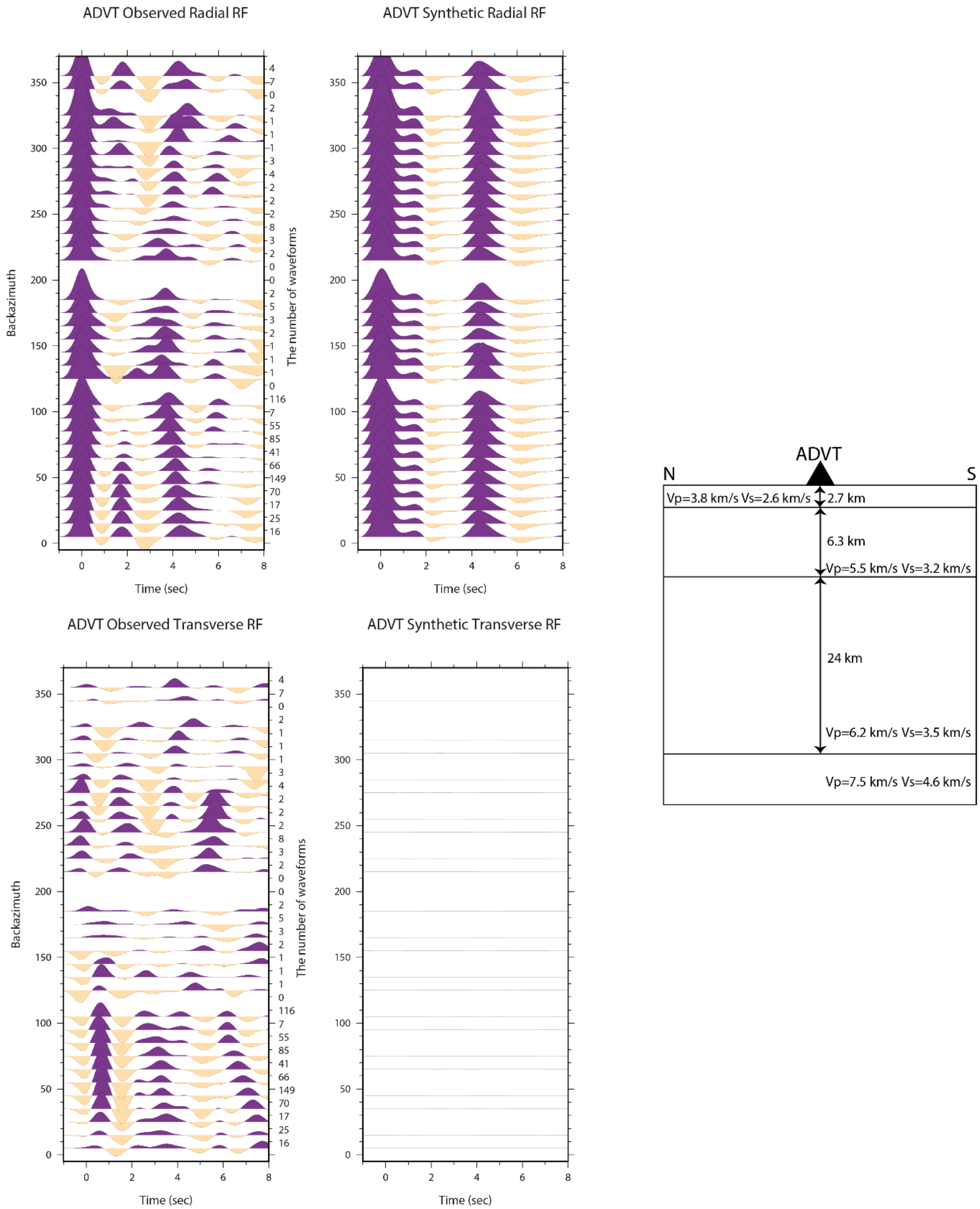

Figure 5.1. ADVT station observed radial RF and synthetic radial RF (upper left). Velocity model for this station with no dipping layer (middle-right). Observed transverse RF and synthetic transverse RF (lower left).

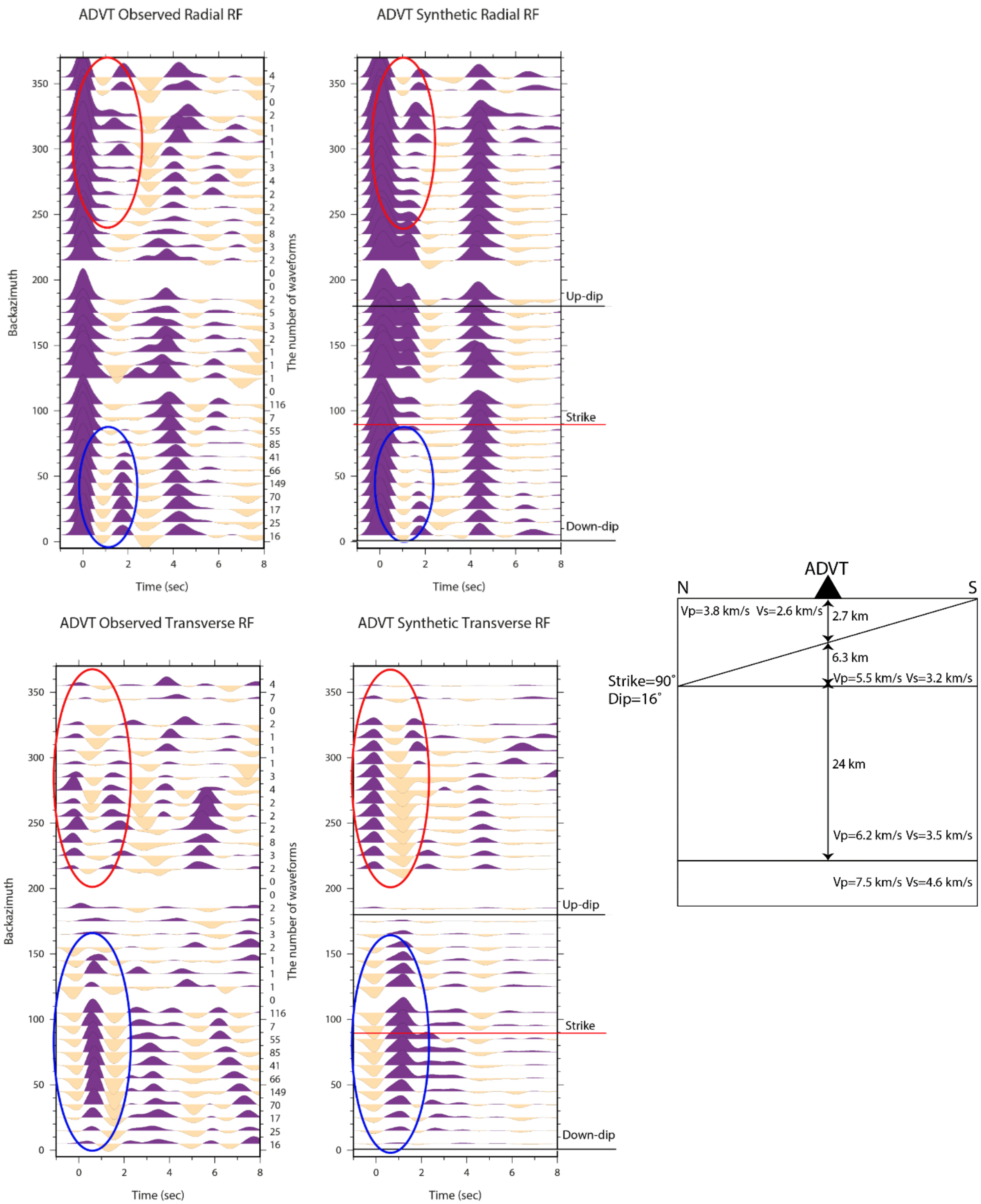

Figure 5.2. ADVT station observed radial RF and synthetic radial RF (upper left). Velocity model for this station with a shallow dipping layer. Vertical axis is not plotted to scale for clarity (middle-right). Observed transverse RF and synthetic transverse RF (lower left).

Note that although the general trends of a shallow dipping layer model satisfy the observed data for both the radial and transversal components, the exact fitting of receiver function requires a fine adjustment of both velocity and depth values. This step of the forward modeling is highly complex and depends on the experience of the performing doing the analysis.

The HRTX station is also classified as an “Unstable” station. The receiver function distribution at this station is quite similar to the ADVT. Once again the direct pulse (located 0-1 sec) of the transversal component has a polarity reversal, while it is positive for the 160^0-340^0 and with negative amplitude between 340^0-160^0. The strike of dipping is 20^0 different as compared to ADVT as shown in Figure 5.3. The second pulse on the tangential which follows the direct one arrives at 0.8 second approximately. This roughly corresponds to the direct phase converted at the shallowest layer. Using the arrival time of this second pulse one can estimate the thickness and velocity pair for the shallowest layer. For the HRTX it found that the shallow layer is much thinner (2 km) as compared to ADVT. The lower layers are horizontal. The exact values of depth and velocities are once more adjusted by hand in order to obtain the best fit visually.

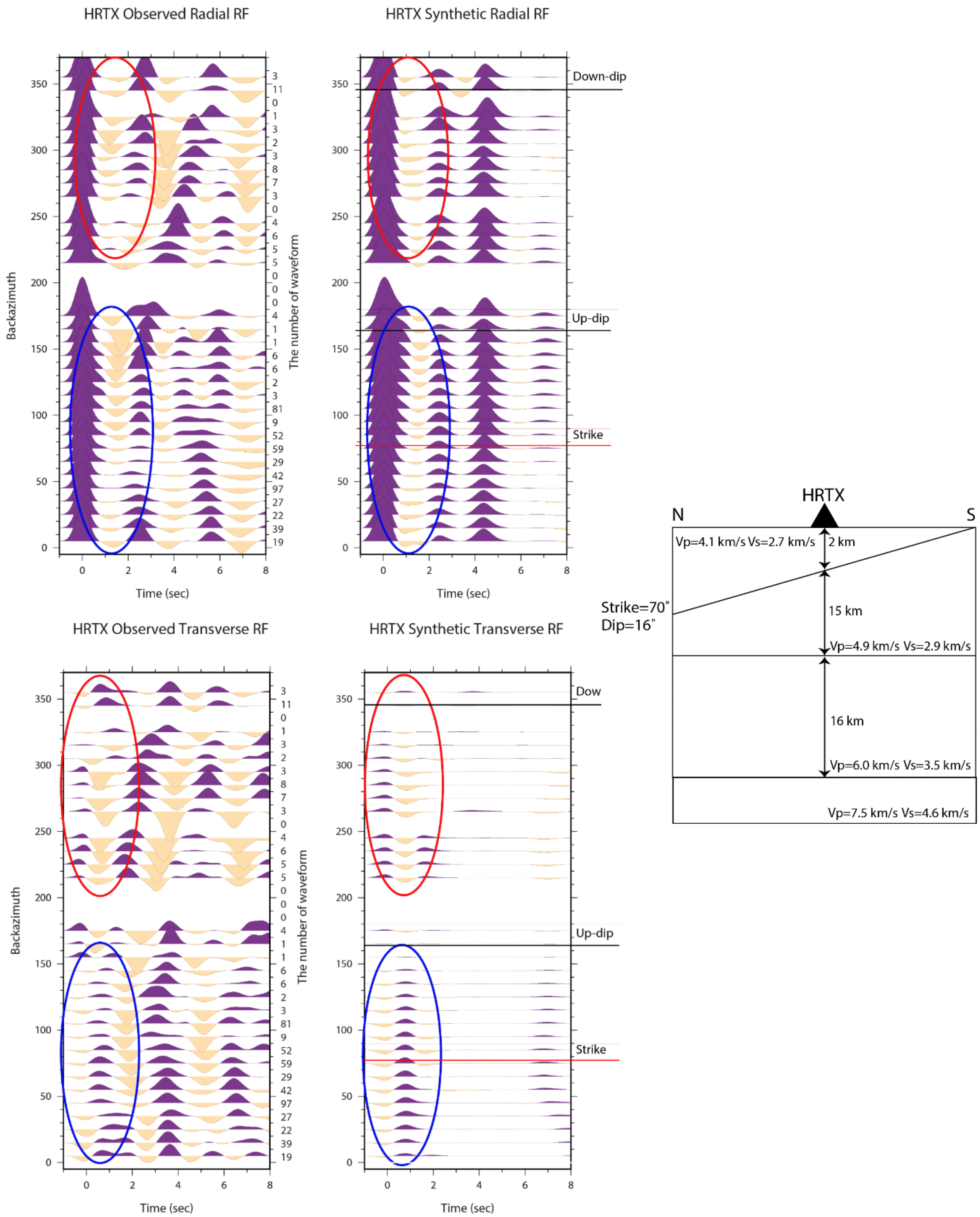

Figure 5.3. HRTX station observed radial RF and synthetic radial RF (upper left). Velocity model for this station with a shallow dipping layer. Vertical axis is not plotted to scale for clarity (middle-right). Observed transverse RF and synthetic transverse RF (lower left).

6. CONCLUSIONS AND DISCUSSIONS

This study focuses on the crust-upper mantle of the Eastern Marmara region in NW Turkey and aims at revealing the general trends of the crustal structure and how it is modified locally by the NAF. The majority of previous studies took the area as a whole and ended up in a single model, which outline an average structure and therefore fails to explain any local deviations due to the NAF. The recent data set from the KOERI and PIRES networks provide more comprehensive source of information as compared to previous studies for this part of the NAF (~10km). The main contribution of this work is to distinguish between two sets of observations, the first one that reflect the general trends of the crust with no interference from the fault lines and the second one which entirely depends on the local deviations due to the proximity of NAF. The first one, in a sense, show the state of a hypothetical crust, which is not disturbed by any major fault line. This case naturally corresponds to a more stable case of observations, where RF have a minimum azimuth variations and identical for close stations. Therefore, the stations that show this particular characteristic are named as “Stable Stations”. It is noted that for stable stations the Moho arrivals and other visible multiples in the radial RFs show about 0.2 sec variation at most. At the other extreme, there is the case of the stations which are at a very close distance the fault line, and therefore the RF entirely reflect the complexity of fault structure, and reveals very little information concerning about the general trend of the crust. In this case, data are characterized by strong azimuth variation and in general hints to a mid-crustal layer and/or a strongly dipping Moho with about 2 sec variations in the radial RFs. The stations which show these characteristic features of unstability are named as “Unstable Stations”. Additionally, two stations which show an intermediate characteristic between stable and unstable ones called as “Quasi-Stable Stations”.

During this study, the data quality of the stations has been examined in detail. In studies where the data coverage extends over many years just like in this thesis, it becomes important critical to check the station health, periodically. The true orientation of the seismometer is important to record horizontal components more reliably and provides a better interpretation of the final results. It is therefore very important to estimate instrument orientation and determine misoriented seismometer. In receiver function studies, azimuthal variation has a critical effect on radial and transverse components. Therefore, a detailed polarization analysis was applied for earthquakes from different directions by calculating their apparent and true back azimuths. It is presented the results for 15 KOERI stations which were used in this study. As a result of this study it is observed that 10 seismometers have a deviation more than 15 degrees from the true north. According to this information, the data was first rotated to correct position before any RF calculation. It is considered that especially this part of study will contribute to the studies of anisotropy, focal mechanism as well as receiver function in the future.

Various methods were applied and interpreted the results in a combined fashion. A total of 6 different methods were applied: CCP stacking, H-K method, RF 1D inversion, surface wave analysis, RF-surface wave joint inversion and 3D forward modelling of RF.

It was started with CCP stacking of RF, which provides the general trends in 3-D view, at a regional scale. Than H-K method was applied to all RF, and estimated the Moho depth below each station in a numerical way. Next in 1D inversion of RF is applied for the most preferred azimuth range that provides a stable result. Surface wave analysis is applied in order to reveal the average properties of the study area. RF and surface wave inversion are treated in a combined way, by applying joint inversion technique. Finally, radial and transverse component are combined in 3D forward RF modelling for two of unstable stations. The results of each step were presented in the following.

Our first approach is to study the receiver functions using CCP stacking method. This method not only allows a joint interpretation of neighboring stations, but also reveals the azimuth variations below a single station. Both information combined give the general trend of all the boundary fluctuations, including the Moho. The software which is called PARAVIEW for displaying CCP stack allows the 3-D rotation of the image, such that any trend can be studied by inspection from every angle of view. In the hardcopy however, results are shown in 2-D views. In this method, all ray paths are combined at each station and represent the trends that are observed in 5 different profiles. The crust and upper mantle structure variation up to 100 km in general and fault geometry are illustrated. The crust-upper mantle variation is evaluated for different cross-sections. It is found that Moho gets thicker at the most northern stations (CTYL-KLYT-SILT) and thinner slightly around Prince Islands segments. Unstable stations and quasi-stable stations show complexity and azimuthal variation for the Moho boundary and mid-crust. Although not clearly seen in all stations, most profiles reveal a negative pulse at 7-8 sec which correspond to the LAB at 60-65 km.

According to our H-K results, the crustal thicknesses in the north Marmara are approximately 35 km at the stations located at the intersection of Istranca Massif and Istanbul Zone. A crustal thinning of 4 km is observed at stations located between Thrace Basin and Istranca Massif. Complex geological structure in the north of Marmara Region has allowed us to see the variation even in a very small area. In the south of our region, in Sakarya Zone, the crustal thickness is approximately 32 km, but the thinnest crust is found in the Karacabey (KCTX) station (28.7 km). Moho thicknesses show more stability in the southern Marmara (south of NAF). Vp/Vs ratio is relatively high at the north stations and varies between 1.75-1.80. In our study, it is found that the average Moho depth and average Vp/Vs ratio are 32 km and 1.76, respectively. Average Moho depth in our result matches well with the previous studies such as Horasan *et al*., (2002), Zor *et al*., (2006), Mutlu (2011) and Vanacore *et al*., (2013).

Focusing on the 1-D Receiver Function inversion results, the majority of the inversion give the Moho as the strongest boundary where a velocity change of the order of 0.4.0.5 km/s can be observed. The depth values for the Moho show a remarkable consistency between individual stations as well as with the outcome of the H-K analysis. The most delayed Moho pulse (5.0 sec) arrival is observed at most northern stations located between Istranca Massif and İstanbul Zone. It is noticed that Moho boundary at both KLYT and SILT stations, has a gradually increasing character, which is different from the other stations where an abrupt change is generally observed. A better modelling of the shallow structures may contribute to the inversion of these stations. However, at this stage complementary data from other sources (reflection, refraction, etc.) are required in order to obtain a better estimation of these shallow layers. In the southern part, Moho boundary is around at 32 km for stations located in Sakarya Zone. Moho arrival is around 3.8 – 4 sec and the sharpest Moho is observed at MDNY station with the highest

S wave velocity of 4.70 km/sec at this boundary. It is also clear that the southern stations also show common characteristics in terms of the Moho depth and the general shape of the velocity-depth variation. In particular, a rather weak low-velocity zone which appears between 14km-23km depth in all stations. This velocity zone is also observed in the joint inversion results but it is even weaker. This is therefore highly likely that it corresponds to the real situation and not an artifact of the inversions. In terms of geodynamics of the region, this slow S-velocity in the lower crust may be interpreted as the sign of a heat flow increase. It is not surprising to have a hot crust in an environment where the Aegean extension becomes the most prominent geodynamic process. The fact that this low velocity zone is not observed in the northern stations seems to support this idea. It is known that the Aegean extension does not extend beyond the NAF zone and only restricted to region where the southern stations are located.

The study uses two main line of analysis, which are complementary in a sense: receiver functions and surface wave analysis. The first one provides “pointwise” information about the crust and concerns a conical volume below the station, which spans an area of at most 10 km of radius at the Moho depth. Surface wave studies on the other hand cover an area large enough, so that dispersive properties can clearly be observed especially between 10-30 sec for group and phase velocities. In our case two-station method by Herrmann (1987) is used so that the average properties of the crust were studied along travel path of about 150 km in length. Two different S wave velocity path are selected in the study due to the tectonic and geologic structure difference in north and south of the region.

Combining surface waves and receiver function in the joint inversion give more realistic and smooth velocities resulting in a better interpretation. Only stable and quasi-stable stations are considered as in the previous case. The stations couple are selected so that two different S-wave velocity model are obtained for north and south part of the Marmara Region. The velocity models get closer to each other for stations situated in the same tectonic regime with a smooth mid-layer and apparent main layers. S wave velocities between 3-8 km depth are around 3 km/s and 3.2 km/s in the north and south stations, respectively. In the deeper part (10-20km), southern stations show a lower velocity (Vs=3.2-3.5km/s) than northern stations (Vs=3.2-3.9km/s). This low S-velocity in the lower crust was also observed in 1D RF inversion as mentioned above. It is considered that heated crust due to the Aegean extension regime in the geodynamic process may be a reason of low velocity in the lower crust. A low velocity zone is not observed in the northern stations. Moho thickness is about 32 km for both regions (north and south of NAF) and S wave velocity reaches 4.5-4.7 km/s at this boundary. Note that, the crustal thickness variation observed across the fault in the Adapazarı area claimed by Frederiksen *et al*., (2015) and Kahraman *et al*., (2015) is not supported by our analysis. These two studies concern a different area located slightly east of the focus area of this thesis, although with a partial overlapping. However, it is should not expected a major variation of the main characteristics of the crust between these two regions in particular in terms of crustal thicknesses.

Finally, in order to better understand the crustal structure in the case where the simple 1D assumption fails due to the fault geometry, an attempt is made for the 3D modelling of RFs. This approach which lies beyond the routine procedures of the classical method of RF, is highly complex and rarely seen in the literature. The results obtained, although preliminary in many sense, are the first application for this region and therefore constitute one of the most significant contribution of the study. It is applied 3D forward modelling to both radial and transverse components so that the azimuth variation of RF is interpreted in a broader sense. Two of the unstable stations near the NAF successfully modelled with including dipping shallow layers. This additional structure is sufficient to satisfy the majority of the pulse generation at in the early part of the RF. It is however observed that the section of the azimuth which correspond to the location of the fault still present some minor complex disturbances which are not easily to satisfied with forward modelling.

REFERENCES

Aktar, M., Fault Structures in Marmara Sea (Turkey) and Their Connection to Earthquake Generation Processes. *Active Global Seismology: Neotectonics and Earthquake Potential of the Eastern Mediterranean Region*, John Wiley & Sons, pp. 225–238, 2017.

Altıner, D., A. Koçyiğit, A. Farinacci, U. Nicosia, M.A. Conti, "Jurassic-Lower Cretaceous Stratigraphy and Paleogeographic Evolution of the Southern Part of North-Western Anatolia (Turkey)", *Geologica Romana*, 27, pp. 13–80, 1991.

Ammon, C.J., G.E. Randall, and G. Zandt, "On the non-uniqueness of receiver function inversions", *J. Geophys. Res.*, 95, pp. 15303–15318, 1990.

Ammon, C. J., "The isolation of receiver effects from teleseismic P waveforms" *Bull. Seismol. Soc. Am.*, 81 (6), pp. 2504–2510, 1991.

Aydın, Y., *Etude pétrographique et géochimique de la parte centrale du Massif d'Istranca (Turquie)*, Ph.D. Thesis, Université de Nancy, 1974.

Badal, J., V. Corchete, G. Payo, L. Pujades, and J. A. Canas, "Imaging of shear wave velocity structure beneath Iberia", *Geophys. J. Int.*, 124, pp. 591–611, 1996.

Barış, Ş., Nakajima, J., Hasegawa, A., Honkura, Y., Ito, A., Üçer, B., "Three-Dimensional Structure of Vp, Vs and Vp/Vs in the Upper Crust of the Marmara Region, NW Turkey" *Earth, Planets and Space*, 57 (11), pp. 1019–38, 2005.

Bohnhoff, M., F. Bulut, G. Dresen, P. E. Malin, T. Eken, and M. Aktar, "An earthquake gap south of Istanbul, *Nature Communications*, 4, pp. 1–6, 2013.

Bourjot, L. and B. Romanowicz, “Crust and upper mantle tomography in Tibet using surface waves”, *Geophys. Res. Lett*., 19, pp. 881–884, 1992.

Brune, J.N. and J. Dorman, “Seismic waves and earth structure in the Canadian shields”, *Bull. Seismol. Soc. Am.*, 53, pp. 167–210, 1963.

Burdick, L. J. and C. A. Langston, “Modeling crustal structure through the use of converted phases in teleseismic body wave forms”, *Bull. Seism. Soc. Am*., 67, pp. 677–691, 1977.

Cassidy, J. and R. Ellis, “S wave velocity structure of the Northern Cascadia subduction zone”, *J. Geophys. Res*., 98 (B3), pp. 4407–4421, 1993.

Cassidy, J.F., “Numerical experiments in broadband receiver function analysis”, *Bull, Seismol. Soc. Am*., 82, pp. 1453–1474, 1992.

Çemen I., and Y. Yılmaz., Neotectonics and Earthquake Potential of the Eastern Mediterranean Region. *Active Global Seismology: Neotectonics and Earthquake Potential of the Eastern Mediterranean Region*. John Wiley & Sons, pp. 1–8, 2017.

Darbyshire, F.A., Larsen, T.B., Mosegaard, K., Dahl-Jensen, T., Gudmundsson, O., Bach, T., Gregersen, S., Pedersen, H.A., Hanka, W., “A First Detailed Look at the Greenland Lithosphere and Upper Mantle, Using Rayleigh Wave Tomography”, *Geophys. J. Int.*, 158 (1), pp. 267–86, 2004.

Dean, W.T., F. Martin, O. Monod, O. Demir, R. B. Rickards, P. Bultynck, N. Bozdogan, “Lower Paleozoic stratigraphy, Karadere - Zirze area, Central Pontides, northern Turkey. In: M.C. Göncüoğlu, and A.S. Derman, (eds.), Early Paleozoic in NW Gondwana”, *Turkish Association of Petroleum Geologists*, 3, pp. 32–38, 1997.

Debayle E., and B.L.N. Kennett, “Anisotropy in the Australasian upper mantle from Love and Rayleigh waveform inversion”, *Earth Planet Set. Lett*, 184, pp. 339–351, 2000.

Denli, A., *3-D velocity structure of eastern Marmara region from local earthquake tomography*, M.Sc. Thesis, Boğaziçi University, 2008.

Dost, B., “Upper Mantle Structure Under Western Europe from Fundamental and Higher Mode Surface Waves Using the Nars Array”, *Geophys. J. Int*., 100 (1), pp. 131–151, 1990.

Frederiksen, A. W., Thompson, D. A., Rost, S., Cornwell, D. G., Gulen, L., Houseman, G. A., Kahraman, M., Altuncu Poyraz, S. A., Teoman, U. M., Turkelli, N., Utkucu, M., “Crustal Thickness Variations and Isostatic Disequilibrium across the North Anatolian Fault, Western Turkey.” *Geophys. Res. Lett*., 42 (3), pp. 751–757, 2015.

Gök, R., Türkelli, N., Sandvol, E., Seber, D., and Barazangi, M., “Regional wave propagation in Turkey and surrounding regions”, *Geophys. Res. Lett*., 27 (3), pp. 429– 432, 2000.

Gomberg, Joan S., and T. Guy Masters, “Waveform Modelling Using Locked-mode Synthetic and Differential Seismograms: Application to Determination of the Structure of Mexico”, *Geophys. J. Int.*, 94 (2), pp. 93–218, 1998.

Görür, N., M. N. Çağatay, M. Sakınç, M. Sümengen, K. Şentürk, C. Yaltırak, A. Tchapalyga, “Origin of the Sea of Marmara as deducted from the Neogene to Quaternary paleogeographic evolution of its frame”, *International Geology Review*, 39, pp. 342–352, 1997.

Güney, A. B., and Horasan, G., “Enhanced Ground Motions Due to Large-Amplitude Critical Moho Reflections (SmS) in the Sea of Marmara, Turkey”, *Geophys. Res. Lett*., 29(2), pp. 7–10, 2002.

Gürbüz, C., Püskülcü, S., Üçer, B., “A study of crustal structure in the Marmara region using earthquake data. In: Isikara, A.M., Honkura, Y. (Eds.), Multidisciplinary Research on Fault Activity in the Western Part of the North Anatolian Fault Zone. KOERI, pp. 29–42, 1992.

Gürbüz C., Aktar M., Eyidoğan H., Cisternas A., Haessler H., Barka A., Ergin M., Türkelli N., Polat O., Üçer B., Kuleli S., Barıs¸ S., Kaypak B., Bekler T., Zor E., Biçmen F., Yörük A., "The seismotectonics of the Marmara Region (Turkey): Results from a microseismic experiment", *Tectonophysics*, 316, pp. 1–17, 2000.

Herrmann, R. B., Computer programs in seismology. Tech. rep., St. Louis 570 University, St. Louis, Missouri, 1987.

Herrmann, R. B., Ammon, C. J., "Surface waves, receiver functions and crustal structure, in Computer Programs in Seismology, Version 3.30", Saint Louis University, 2002, http://www.eas.slu.edu/eqc/eqccps.htm.

Horasan, G., Kaşlılar-Özcan, A., Boztepe-Güney, A., and Türkelli, N., "S-wave attenuation in the Marmara region, Northwestern Turkey", *Geophys. Res. Lett*., 25, pp. 2733– 2736, 1998.

Horasan, G., Gülen, L., Pinar, A., Kalafat, D., Özel, N., Kuleli, H.S., Işıkara, A.M., "Lithospheric structure of the Marmara and Aegean regions, western Turkey", *Bull. Seism. Soc. Am*., 92, 1, pp. 322–329, 2002.

Jones, Craig H., and Robert A. Phinney, "Seismic Structure of the Lithosphere from Teleseismic Converted Arrivals Observed at Small Arrays in the Southern Sierra Nevada and Vicinity, California" *Journal of Geophysical Research: Solid Earth*, 103 (B5), pp. 10065–10090, 2004.

Julià, J., Josep, V., and Ramon, M., "The Receiver Structure beneath the Ebro Basin, Iberian Peninsula", *Bull. Seism. Soc. Am*., 88 (6), pp. 1538–47, 1998.

Julià, J., Ammon, C. J., Herrmann, R. B., & Correig, A. M., "Joint inversion of receiver function and surface wave dispersion observations", *Geophys. J. Int*., 143 (1), pp. 99-112, 2000.

Julià, J., Ammon, C. J., & Herrmann, R. B., "Lithospheric structure of the Arabian Shield from the joint inversion of receiver functions and surface-wave group velocities", *Tectonophysics*, 371 (1), pp. 1-21, 2003.

Julià, J., Herrmann, R. B., Ammon, C. J., Akinci, A. "Evaluation of Deep Sediment Velocity Structure in the New Madrid Seismic Zone" *Bull. Seism. Soc. Am*., 94 (1), pp. 334–40, 2004.

Kahraman, M., D. G. Cornwell, D. A. Thompson, S. Rost, G. A. Houseman, N. Türkelli, U. Teoman, S. A. Poyraz, M. Utkucu, and L. Gülen, "Crustal-Scale Shear Zones and Heterogeneous Structure beneath the North Anatolian Fault Zone, Turkey, Revealed by a High-Density Seismometer Array" *Earth and Planetary Science Letters*, 430, pp. 129–39, 2015.

Karabulut, H., Özalaybey, S., Taymaz, T., Aktar, M., Selvi, O., Kocaoğlu, A., "A Tomographic Image of the Shallow Crustal Structure in the Eastern Marmara", *Geophys. Res. Lett*., 30 (24), p. 2277, 2003.

Karabulut H, Schmittbuhl J., Özalaybey S., Lengliné O., Kömeç Mutlu, A., Durand V., Bouchon M., Daniel M.P., E "Evolution of the Seismicity in the Eastern Marmara Sea a Decade before and after the 17 August 1999 Izmit Earthquake" *Tectonophysics*, 510 (1–2), pp. 17–27, 2011.

Kikuchi, M., and Kanamori, H., "Inversion of complex body waves", *Bull. Seism. Soc. Am*., 72 (2), pp. 491-506, 1982.

Knopoff, L., "Observation and inversion of surface-wave dispersion", *Tectonophysics*, 13, pp. 497-519, 1972.

KRDAE, Boğaziçi University, Kandilli Observatory and Earthquake Research Institute, 2019, http://udim.koeri.boun.edu.tr.

Kuleli, H. S., Gürbüz, C., and Toksöz, M. N., “Seismic velocity distribution in the Aegean region, in Proceedings of International Earth Sciences Colloquium on the Aegean region”, Vol. 1, pp. 241-254. 1995.

Langston, C. A., “The effect of planar dipping structure on source and receiver responses for constant ray parameter”, *Bull. Seism. Soc. Am.*, 67, pp. 1029-1050, 1977.

Langston, C. A., “Structure under Mount Rainier, Washington, inferred from teleseismic body waves” *Journal of Geophysical Research: Solid Earth*, 84 (B9), pp. 4749-4762, 1979.

Larson, E.W.F., Ekström, G., “Determining Surface Wave Arrival Angle Anomalies” *Journal of Geophysical Research*, 107(B6), 2002.

Laske, G., “Global observation of off-great-circle propagation of long-period surface waves” *Geophys. J. Int*. 123, pp. 245–259, 1995.

Laske, G., Masters, G., “Constraints on global phase velocity maps from long period polarization data”, *J. Geophys. Res*., 101 (B7), pp. 16059–16075, 1996.

Ligorría, J. P., & Ammon, C. J., “Iterative deconvolution and receiver-function estimation”, *Bull. Seism. Soc. Am*., 89 (5), pp. 1395-1400, 1999.

Liggoria, J.P., *The Mantle-Crust Transition beneath North. America*, Ph.D. Thesis, Deparment of Earth Atmospheric. Sciences St. Louis University, 2000.

Lowrie, W., (2007). Fundamentals of geophysics. Cambridge University Press.

Mangino, Stephen G, George Zandt, and Charles J Ammon., “The Receiver Structure Beneath Mina, Nevada”, *Bull. seism. Soc. Am*., 83 (2): pp. 542–60, 1993.

McClusky, S., S. Balassania, A. Barka, C. Demir, S. Ergintav, I. Georgiev, O. Gurkan, M. Hamburger, K. Hurst, H. Kahle, L. Kastens, G. Kekelidze, R. W. King, V. Kotzev, O. Lenk, S. Mahmoud, A. Mishin, M. Nadariya, A. Ouzounis, D. Paradissis, Y. Peter, M. Prilepin, R. Reilinger, I. Sanli, H. Seeger, A. Taeleb, M. N. Toksoz, and G. Veis, GPS constraints on plate motions and deformation in the Eastern Mediterranean: Implications for plate dynamics, J. Geophys. Res., 105, 5695–5719, 2000.

McEvilly T. V., “Central U. S. crust-upper mantle structure from Love and Rayleigh wave phase velocity inversion, *Bull, seism. Soc. Am.*, 54, pp. 1997–2015, 1964.

McKenzie, D., “Active tectonics of the Mediterranean region”, *Geophys. J. Roy. Ast. Soc.*, 30, pp. 109-185, 1972.

Mokhtar, T.A., Ammon, C.J., Herrmann, R.B., Ghalib, H.A.A., “Surface wave velocities across Arabia”, *Pure Appl. Geophys.*, 158, pp. 1425–1444, 2001.

Moore, W.J., E.H. McKee, Ö. Akinci, “Chemistry and chronology of plutonic rocks in the Pontid Mountains, northern Turkey”, *European Copper Deposits*, Vol. 1, pp. 209–216, 1980.

MTA, General Directorate of Mineral Research and Exploration of Turkey, 2019, http://www.mta.gov.tr/eng/.

Mutlu, Ahu Kömeç, and Hayrullah Karabulut. “Anisotropic Pn Tomography of Turkey and Adjacent Regions.” *Geophysical Journal International*, 187(3): pp. 1743–58, 2011

Okay, A.I., O. Tüysüz, “Tethyan sutures of northern Turkey. In: Durand, B., Jolivet, L., Horváth, F., Séranne, M. (Eds.), The Mediterranean Basins: Tertiary Extension within the Alpine Orogen”, Geological Society, London, pp. 475–515 (special publications), 1999.

Okay, A I, and A Kas., “Active Faults and Evolving Strike-Slip Basins in the Marmara Sea, Northwest Turkey: A Multichannel Seismic Reflection Study”, 321, pp. 189–218, 2000

Okay, A., Geology of Turkey, *Anschnitt*, Vol. 21,19–42, 2008.

Oruç B., T. Sönmez, "The rheological structure of the lithosphere in the Eastern Marmara region, Turkey", *Journal of Asian Earth Sciences*, 139, pp. 183-191, 2017.

Owens, T. J., *Determination of crustal and upper mantle structure from analysis of broadband teleseismic P-waveforms*, Ph.D. thesis, Department of Geology and Geophysics, The University of Utah, 1984.

Owens, T. J., Zandt, G., & Taylor, S. R.," Seismic evidence for an ancient rift beneath the Cumberland Plateau, Tennessee: A detailed analysis of broadband teleseismic P waveforms", *Journal of Geophysical Research: Solid Earth* (1978–2012), 89 (B9), 7783-7795, 1984.

Reilinger, R., McClusky, S., Vernant, P., "GPS Constraints on Continental Deformation in the Africa-Arabia-Eurasia Continental Collision Zone and Implications for the Dynamics of Plate Interactions", *Journal of Geophysical Research*, 111, 2006.

Reilinger, R., S. McClusky, D. Paradissis, S. Ergintav, P. Vernant "Geodetic constraints on the tectonic evolution of the Aegean region and strain accumulation along the Hellenic subduction zone" *Tectonophysics*, 488, pp. 22-30, 2010.

Sambridge, M.S. and B.L.N. Kennett., "Boundary value ray tracing in a heterogeneous medium: A simple and versatile algorithm", *Geophys. J. Int*., 101: pp. 157–168, 1990.

Sandvol E, Seber D, Calvert A, Barazangi M, "Grid search modeling of receiver functions: Implications for crustal structure in the Middle East and North Africa", *J Geophys Res*., 103: pp. 26899-26917, 1998.

Scherbaum, F. and Johnson J., "PITSA, Programmable interactive toolbox for seismological analysis", In: Lee, W.H.K. (eds), IASPEI Software Library, USA. V 5, 269 pp., 1992.

Schulte-Pelkum, V., Masters, G. and Shearer, P. M.," Upper mantle anisotropy from long period P polarization", *J. Geophys. Res.*, 106 (B10), 21, 917-21, 934, 2001.

Schulte-Pelkum, Vera, Guy Masters, and Peter M. Shearer., "Upper Mantle Anisotropy from Long-Period P Polarization", *Journal of Geophysical Research: Solid Earth*, 106 (B10): pp. 21917–34, 2004.

Schulte-Pelkum, Vera, and Kevin H. Mahan., "A Method for Mapping Crustal Deformation and Anisotropy with Receiver Functions and First Results from USArray." *Earth and Planetary Science Letters*, 402 (C): pp. 221–33, 2014.

Shearer, Peter M., *Introduction to Seismology*, Cambridge: Cambridge University Press, p.220, 1999.

Sheehan, A. F., G. A. Abers, A. L. Lerner-Lam, and C. H. Jones, "Crustal thickness variations across the Colorado Rocky Mountains from teleseismic receiver functions", *J. Geophys. Res.*, 100, 20,391-20,404, 1995.

Shen, Weisen, Michael H. Ritzwoller, Vera Schulte-Pelkum, and Fan Chi Lin, "Joint Inversion of Surface Wave Dispersion and Receiver Functions: A Bayesianmonte-Carlo Approach.", *Geophysical Journal International* 192 (2): pp. 807–36, 2013.

Stachnik, J. C., Sheehan, A. F., Zietlow, D. W., Yang, Z., Collins, J. and Ferris, A., "Determination of New Zealand Ocean Bottom Seismometer Orientation via Rayleigh Wave Polarization", *Seismol. Res. Lett.*, 83(4), 704–713, 2012.

Stein, R. S., A. A. Barka, and J. H. Dieterich, "Progressive failure on the North Anatolian fault since 1939 by earthquake stress triggering", *Geophys. J. Int.*, 128, pp. 594–604, 1997.

Şengör, A. M. C., C. Grall, C. Imren, X. Le Pichon, N. Gorur, P. Henry, H. Karabulut, and M. Siyako, "The geometry of the North Anatolian transform fault in the Sea of Marmara and its temporal evolution: Implications for the development of intracontinental transform faults", *Can. J. Earth Sci*., 51 (3), pp. 222–242, 2014.

Tezel, T., Shibutani, T., Kaypak, B., "Crustal thickness of Turkey determined by receiver function", *Journal of Asian Earth Sciences*, 75, pp. 36–45, 2013.

Tüysüz, O., "A geo-traverse from the Black Sea to the Central Anatolia: Tectonic evolution of the northern Neo-Tethys", *Turkish Association of Petroleum Geologists Bulletin*. 5/1, pp. 1-33, 1993.

Vanacore, E.A., Taymaz, T., Saygin, E., "Moho structure of the Anatolian Plate from receiver function analysis", *Geophys. J. Int*. 193, 329–337, 2013.

Wittlinger, G., Vergne, J., Tapponnier, P., Farra, V., Poupinet, G., Jiang, M., Su, H., Herquel, G., Paul, A., "Teleseismic imaging of subducting lithosphere and Moho offsets beneath western Tibet", *Earth Planet. Sci. Lett*., 221, pp. 117–130, 2004.

Yılmaz Y., Morphotectonic Characteristics of Neotectonics in Anatolia and Its Surroundings *Active Global Seismology: Neotectonics and Earthquake Potential of the Eastern Mediterranean Region*. John Wiley & Sons, 2017, pp. 11-91, 2017.

Yoshizawa K. Yomogida K. Tsuboi S., "Resolving power of surface wave polarization for higher-order heterogeneities", *Geophys. J. Int*., 138, 205–220, 1999.

Zelt, C. A. and R. M. Ellis, "Practical and efficient ray tracing in twodimensional media for rapid travel-time and amplitude forward modeling", *Can. J. Explor. Geophys*., 24, pp. 16–31, 1988.

Zha, Y., S. C. Webb, and W. Menke, “Determining the orientations of ocean bottom seismometers using ambient noise correlation”, *Geophys.Res. Lett*., 40, no. 14, pp. 3585–3590, 2013.

Zhu, H. and Kanamori, H., “Moho depth variation in southern California from teleseismic receiver functions”, *J. Geophys.Res*., 105, 2969-2980, 2000.

APPENDIX A1: RECEIVER FUNCTIONS FOR KOERI NETWORK

ADVT Station Radial RFs

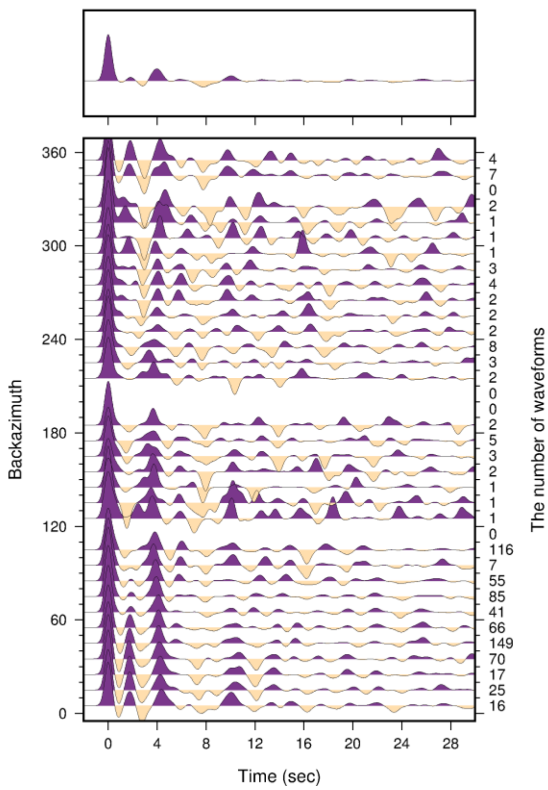

ADVT Station Transverse RFs

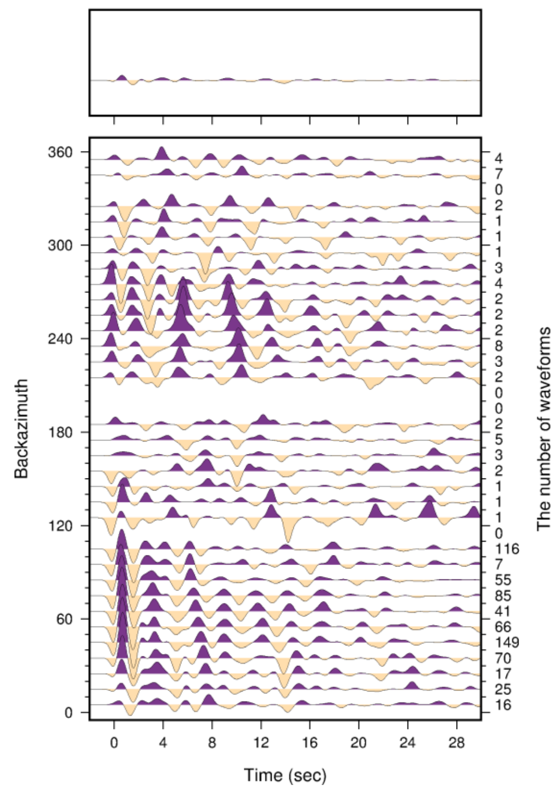

ARMT Station Radial RFs

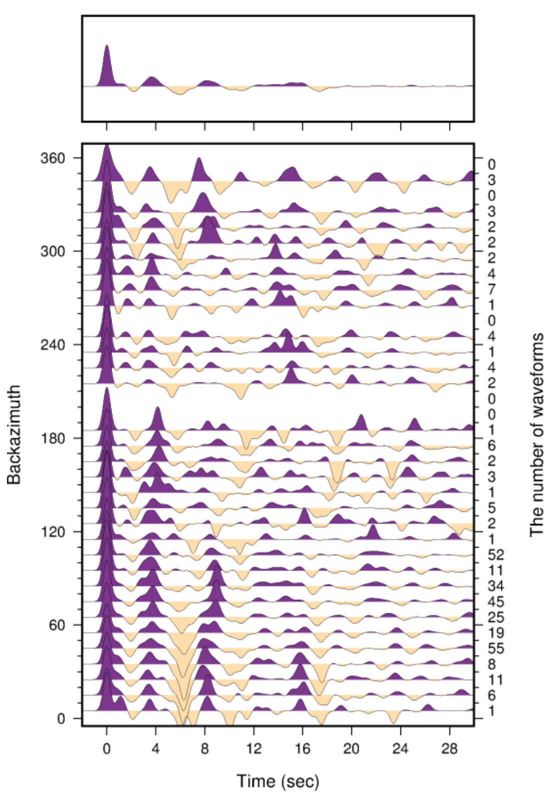

ARMT Station Transverse RFs

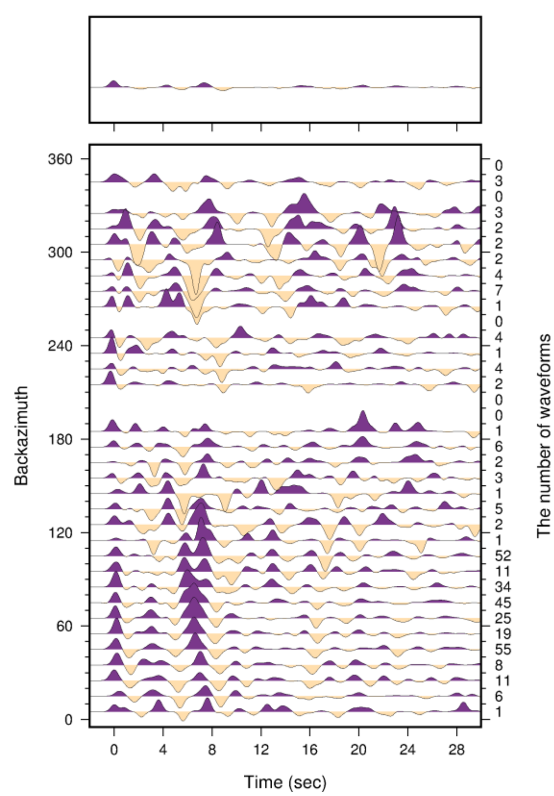

CTKS Station Radial RFs

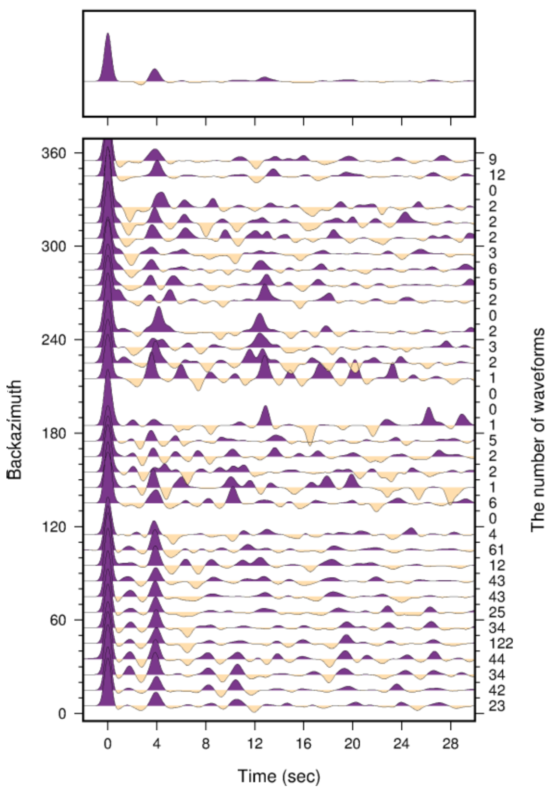

CTKS Station Transverse RFs

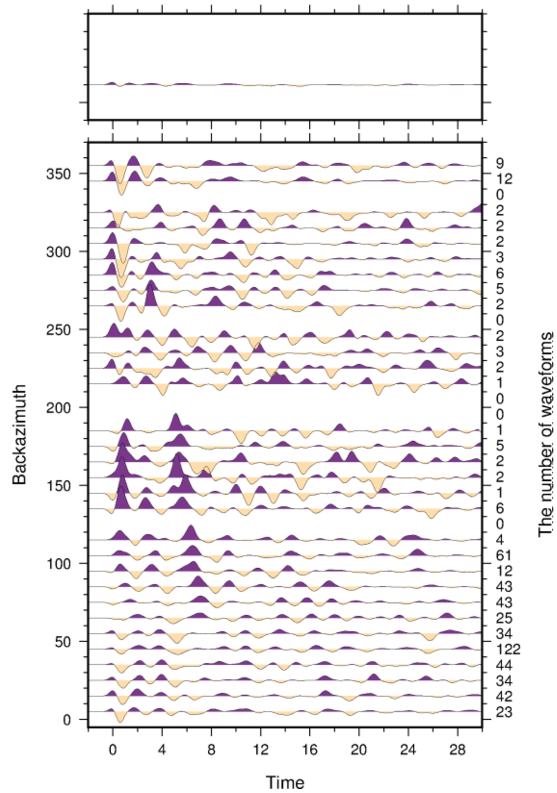

CTYL Station Radial RFs

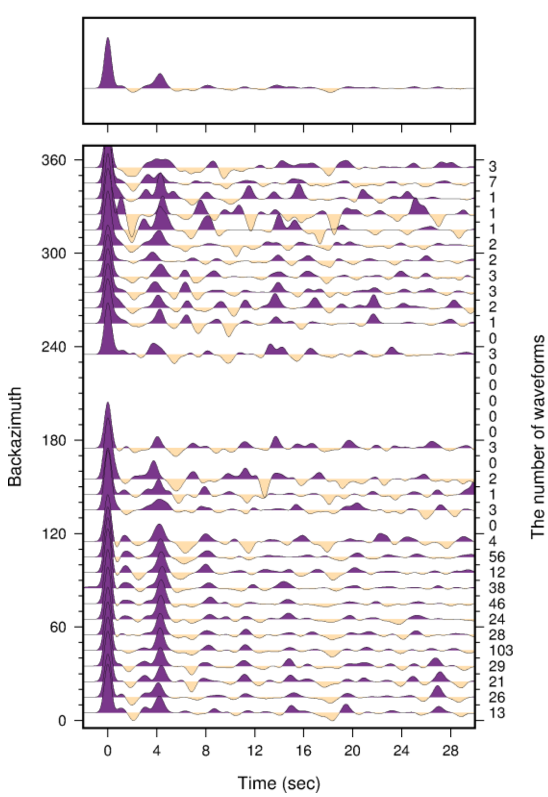

CTYL Station Transverse RFs

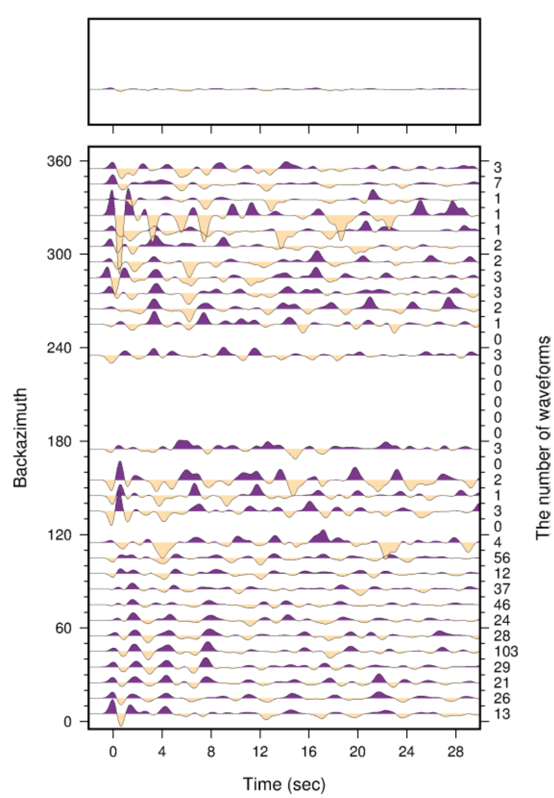

EDC Station Radial RFs

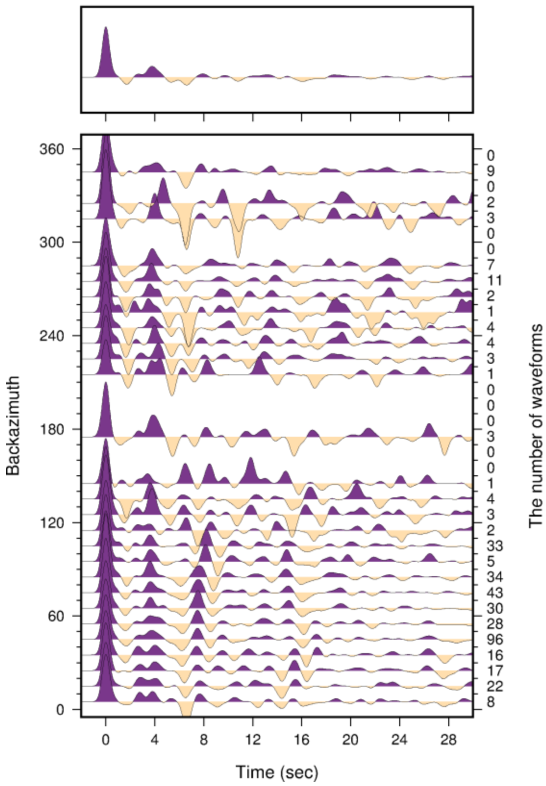

EDC Station Transverse RFs

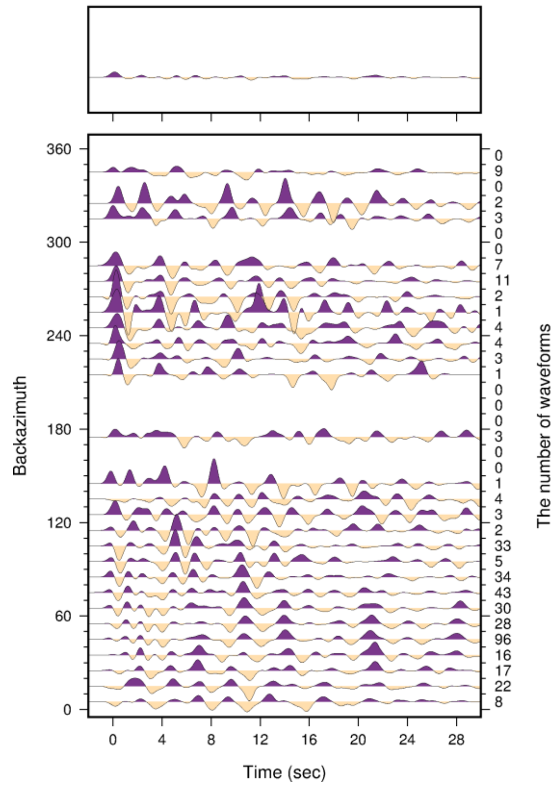

GEMT Station Radial RFs

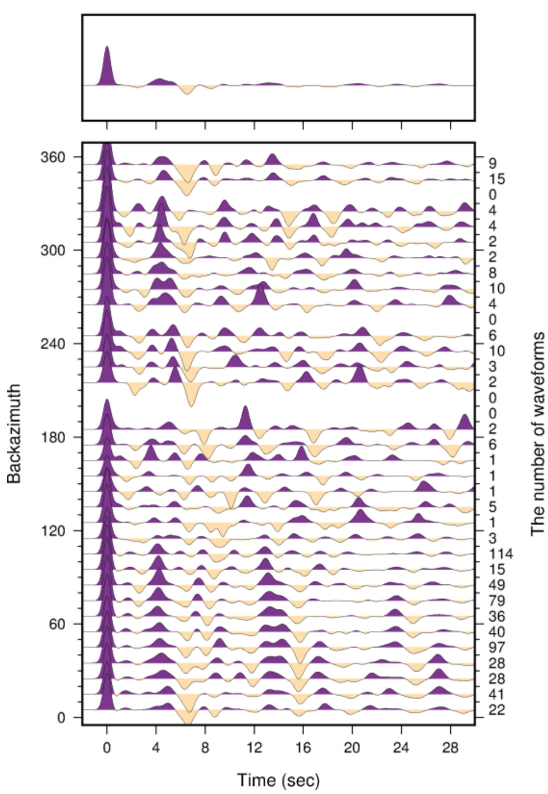

GEMT Station Transverse RFs

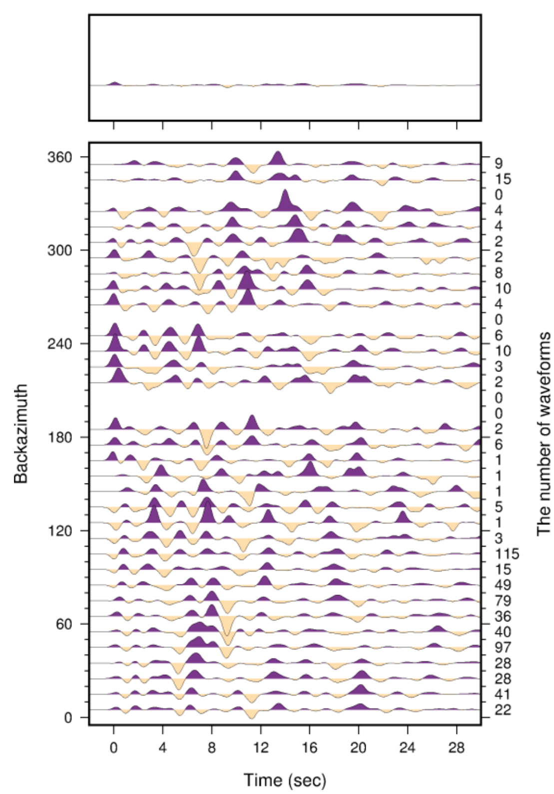

HRTX Station Radial RFs

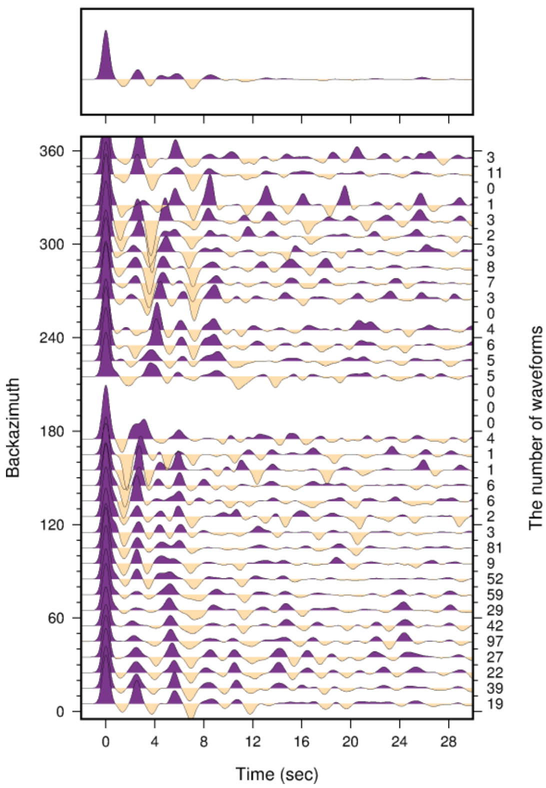

HRTX Station Transverse RFs

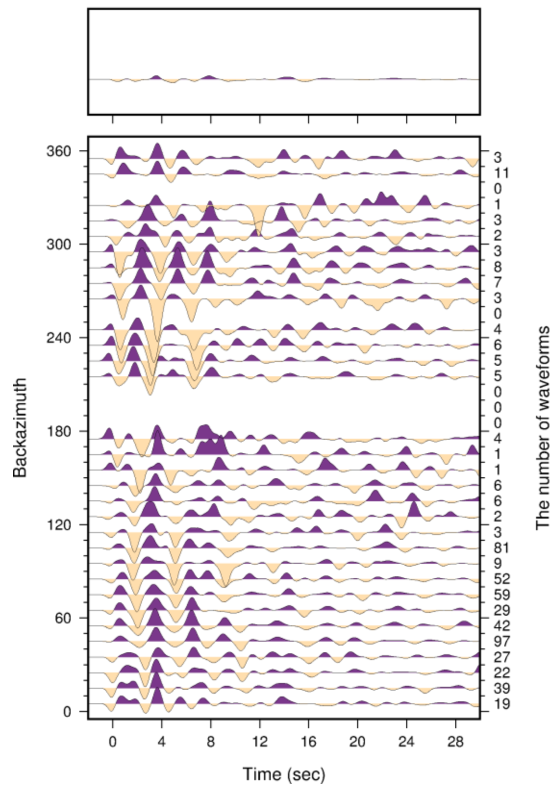

ISK Station Radial RFs

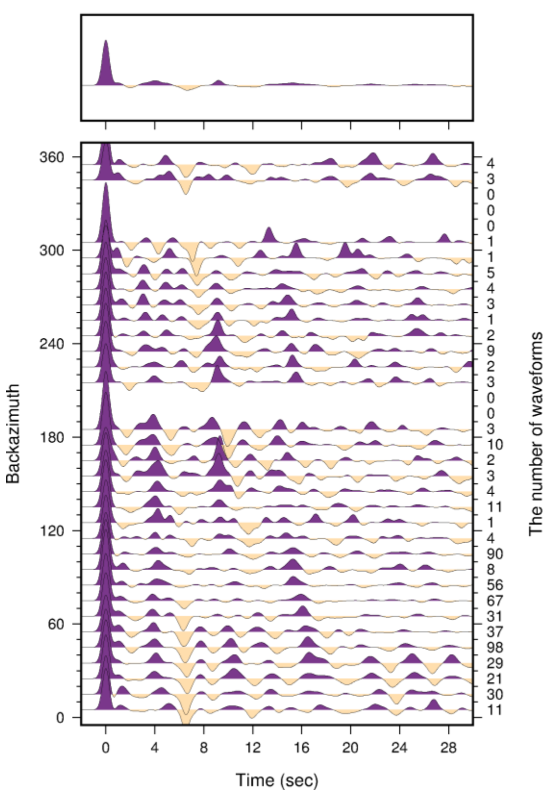

ISK Station Transverse RFs

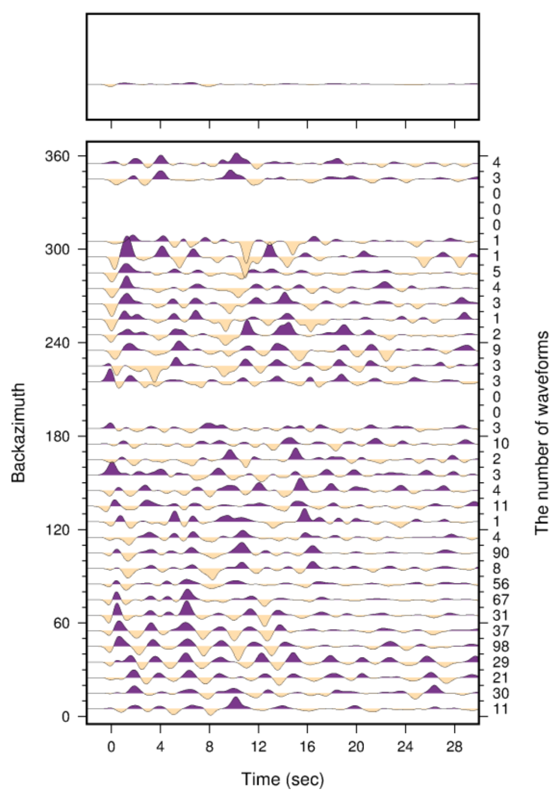

KCTX Station Radial RFs

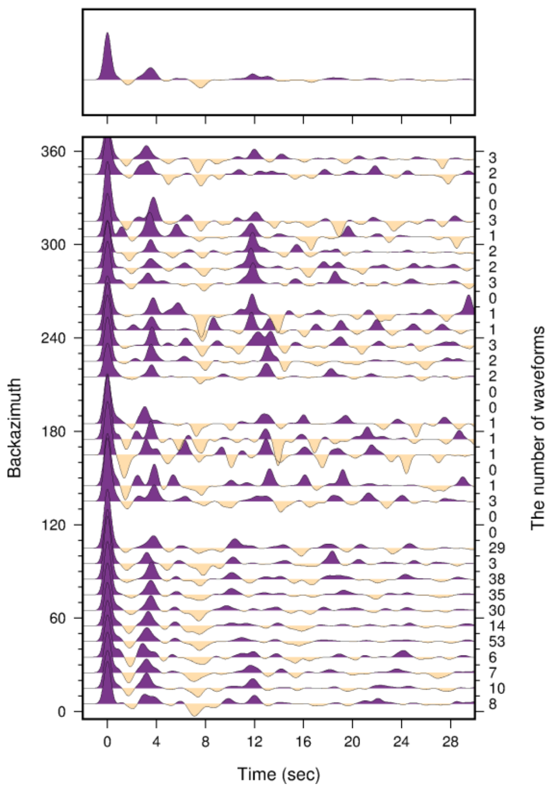

KCTX Station Transverse RFs

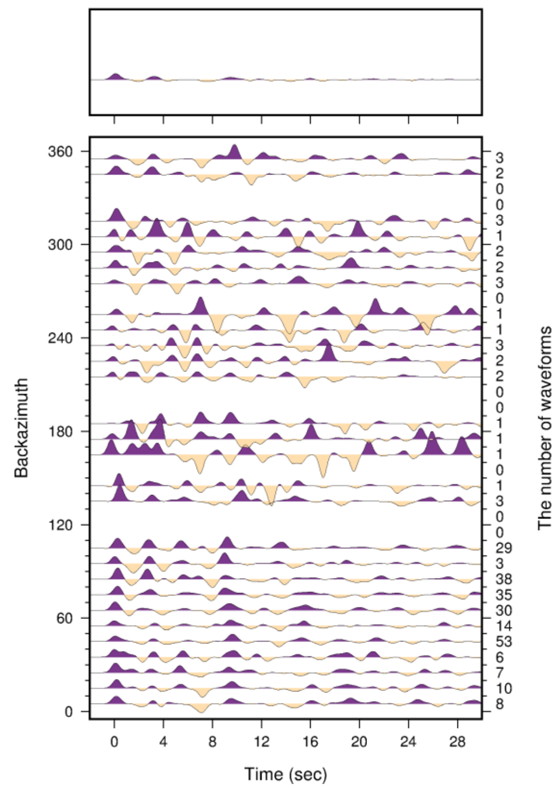

KLYT Station Radial RFs

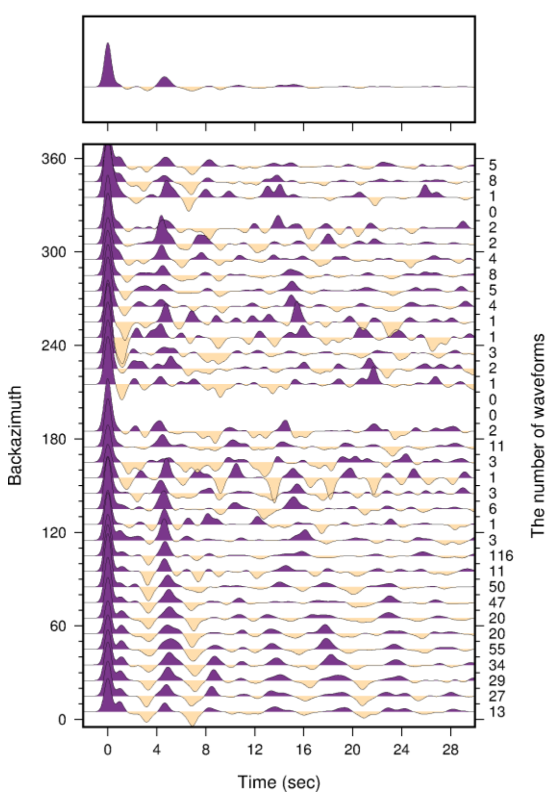

KLYT Station Transverse RFs

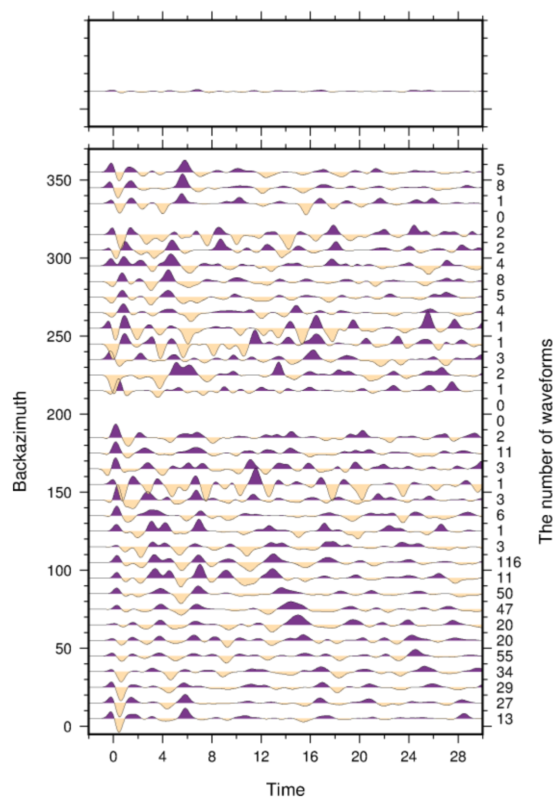

MDNY Station Radial RFs

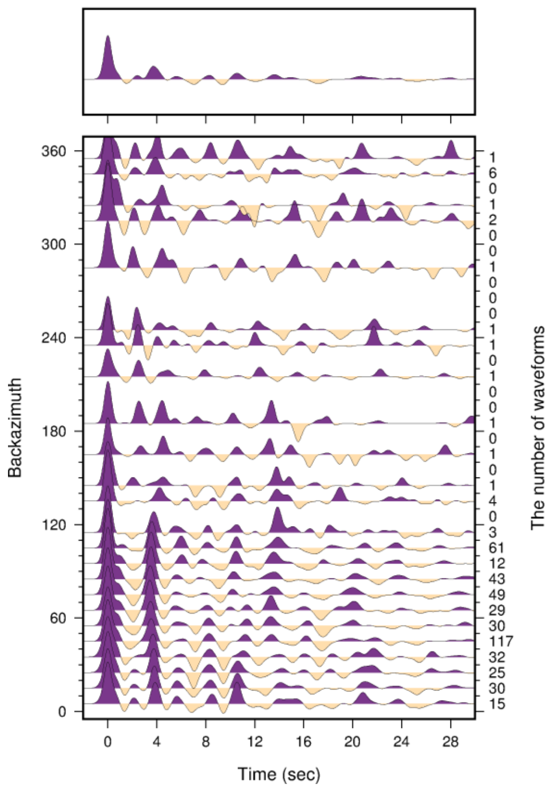

MDNY Station Transverse RFs

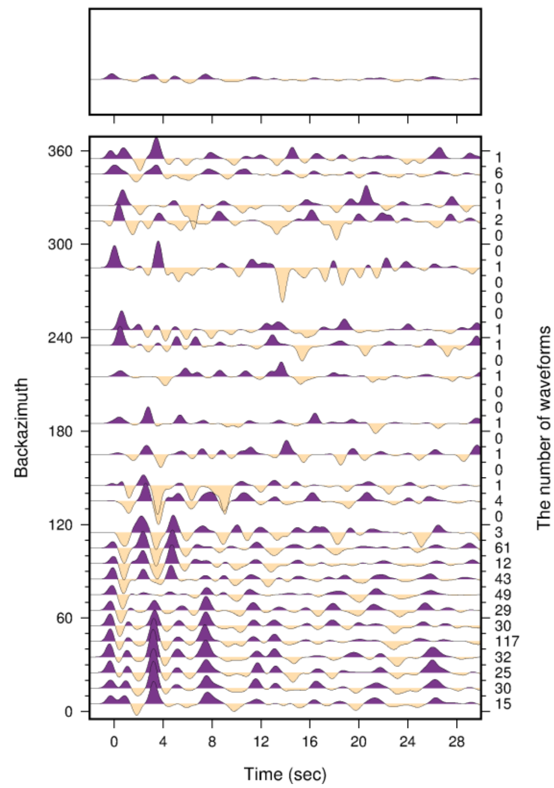

SILT Station Radial RFs

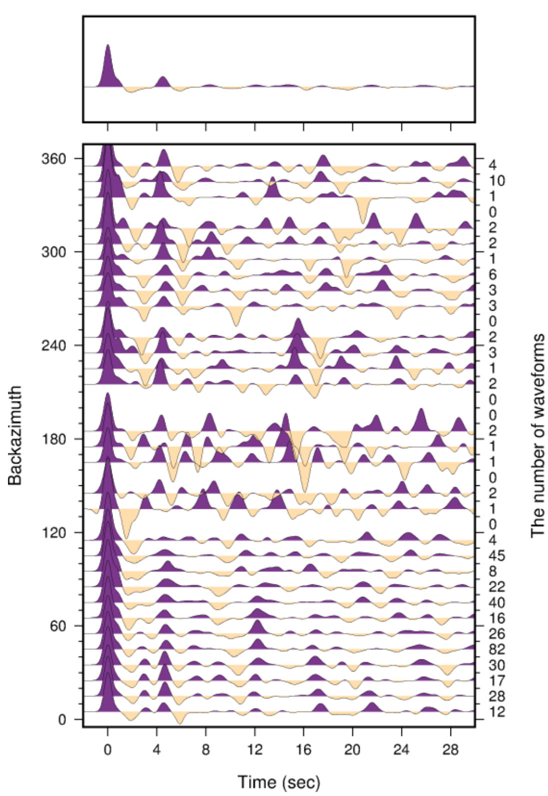

SILT Station Transverse RFs

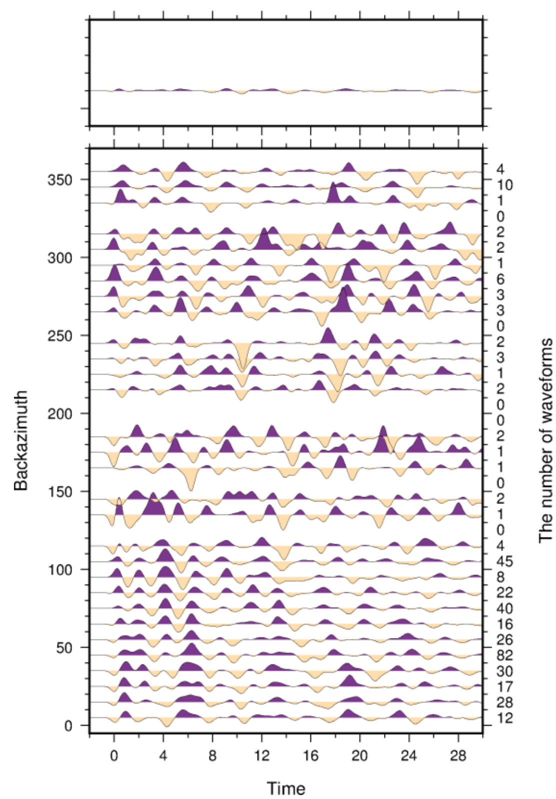

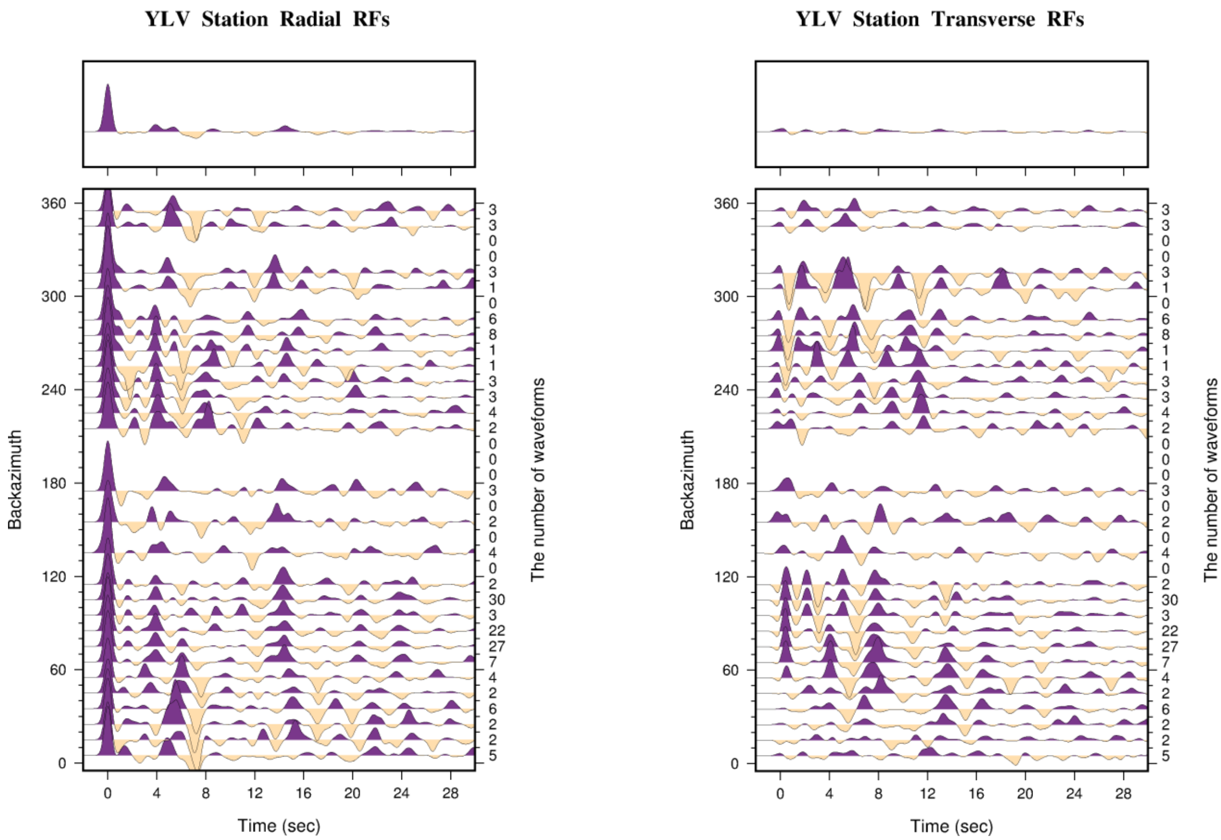
YLV Station Radial RFs
Backazimuth
0 60 120 180 240 300 360
Time (sec)
0 4 8 12 16 20 24 28
The number of waveforms
3 3 0 0 3 1 0 6 8 1 1 3 3 4 2 0 0 0 3 0 2 0 4 0 2 30 3 22 27 7 4 2 6 2 2 5
YLV Station Transverse RFs
Backazimuth
0 60 120 180 240 300 360
Time (sec)
0 4 8 12 16 20 24 28
The number of waveforms
3 3 0 0 3 1 0 6 8 1 1 3 3 4 2 0 0 0 3 0 2 0 4 0 2 30 3 22 27 7 4 2 6 2 2 5

APPENDIX A2: RECEIVER FUNCTIONS FOR PIRES NETWORK

BRGZ Station Radial RFs

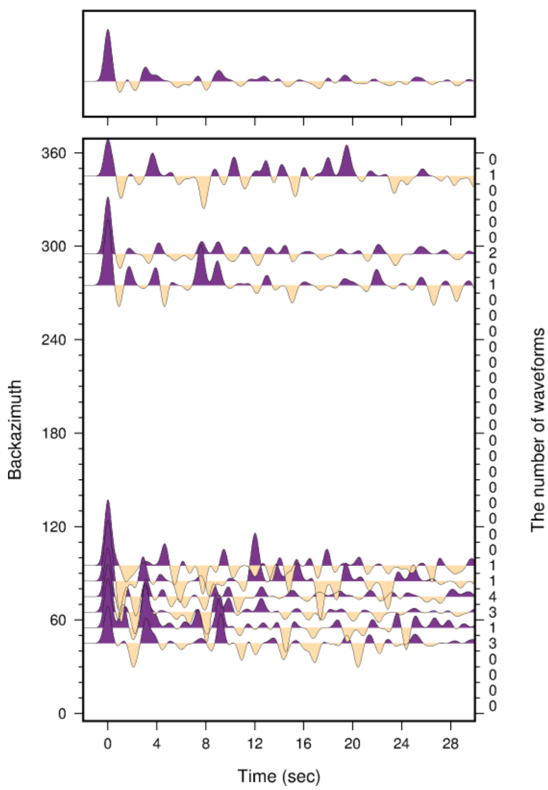

BRGZ Station Transverse RFs

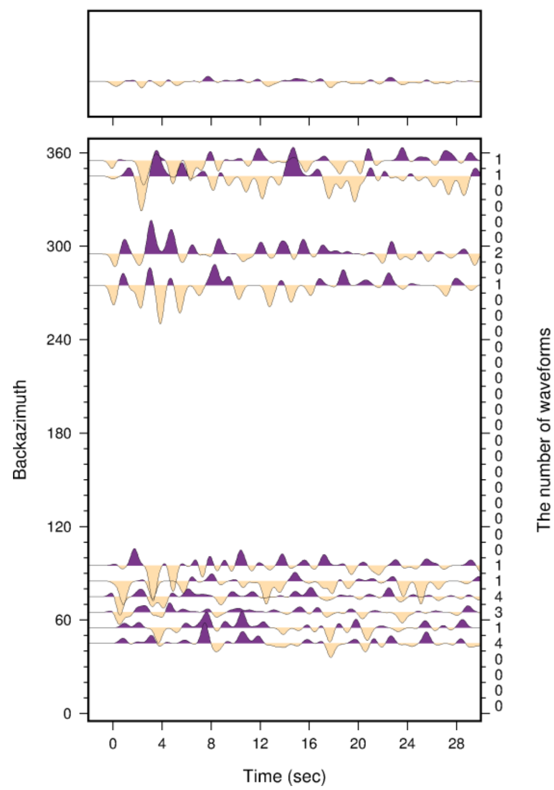

BUYA Station Radial RFs

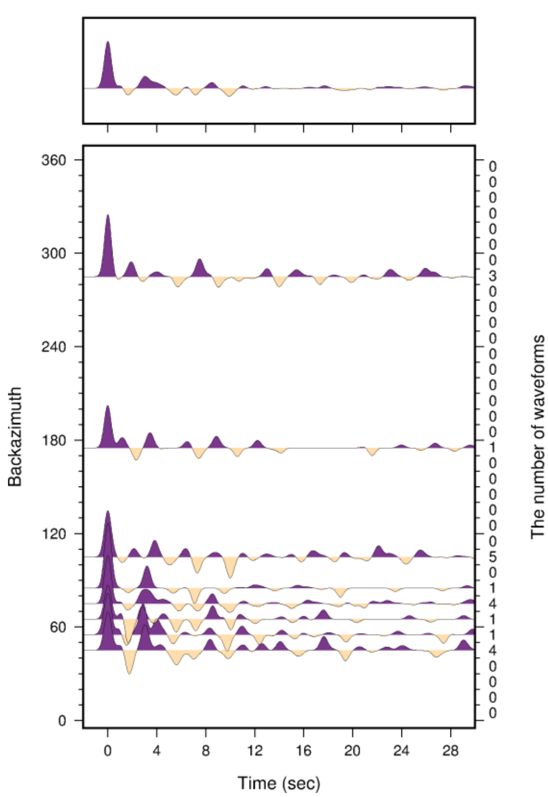

BUYA Station Transverse RFs

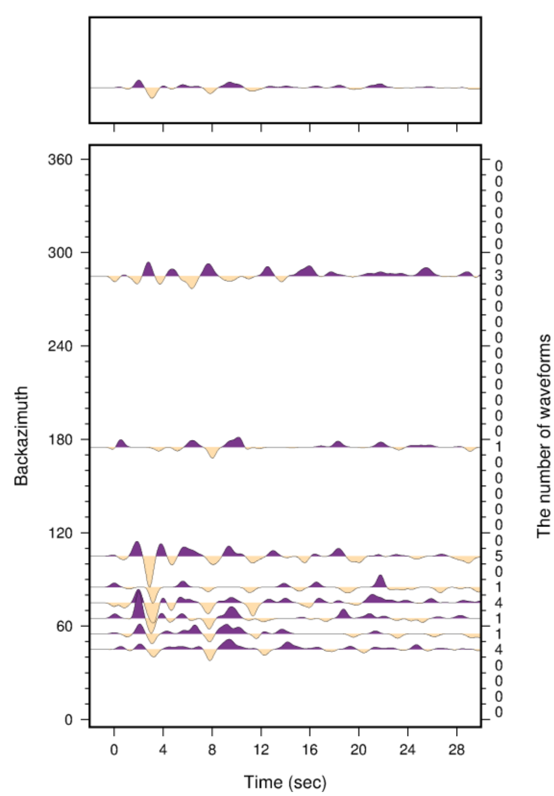

YASSI Station Radial RFs

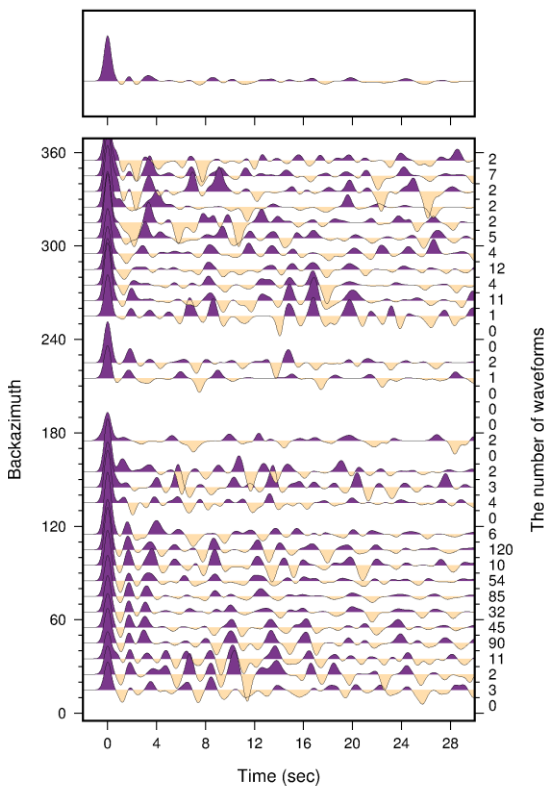

YASSI Station Transverse RFs

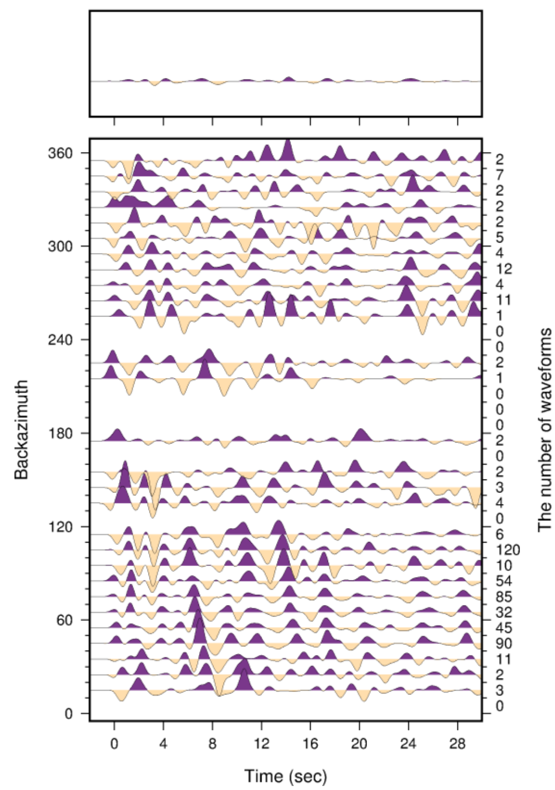

SIVRI Station Radial RFs

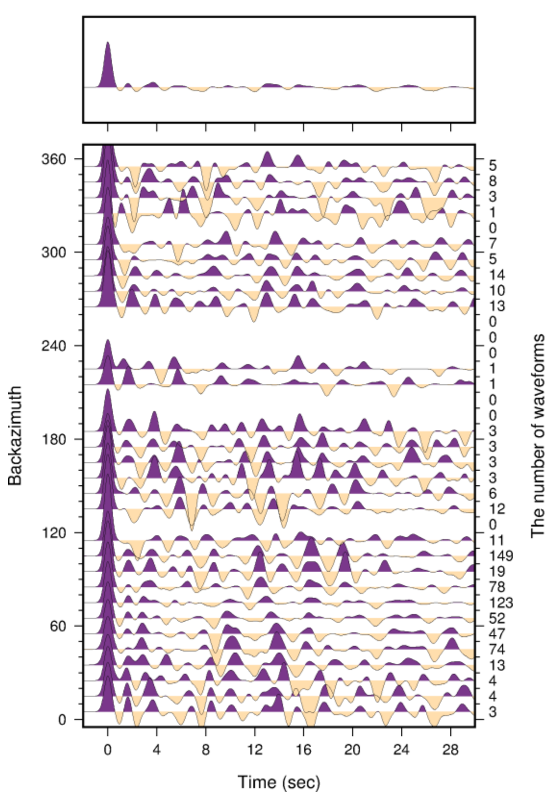

SIVRI Station Transverse RFs